ATOMIC AND ELECTRONIC STRUCTURE OF GRAIN BOUNDARIES IN GALLIUM ARSENIDE

Sujata Krishna
Wolfson College
Oxford

Trinity Term 1994
A thesis submitted for the degree of Doctor of Philosophy at the
Department of Materials,
University of Oxford.

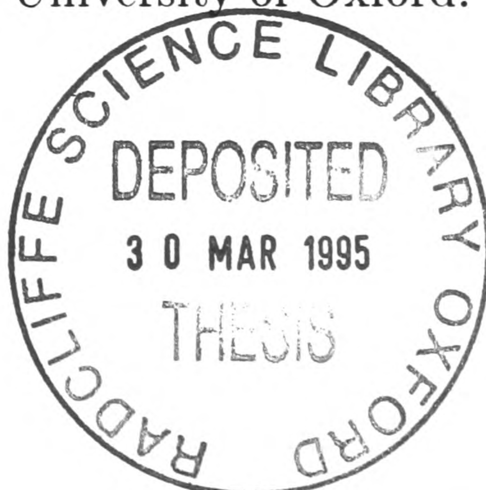

The Atomic and Electronic Structure of Grain Boundaries in Gallium Arsenide

Sujata Krishna
Wolfson College

A thesis submitted for the degree
of Doctor of Philosophy

Trinity Term, 1994

Abstract

HREM imaging was performed using the Jeol 4000ex microscope on specimens prepared from an as-grown ingot of semi-insulating Gallium Arsenide. Various low angle grain boundaries were imaged in the [110] orientation, misorientations varying between 4^0-13^0. Detailed study of a grain boundary of 11.5^0 misorientation about the [110] rotation axis has been carried out. Burgers vector analysis showed the presence of perfect 60^0 and [001] dislocations.

Modelling of the [001] dislocation has been carried out using the Tersoff potential, Bond Order Potential and a tight binding Hamiltonian for GaAs, using Chadi (1984) parameters. The dislocation core was associated with an 8-membered and two 5-membered rings. Assuming there is a minimum of wrong bonds, we predict that the core has two wrong bonds, one being Ga-Ga, and the other As-As, both in equivalent positions where the two 5-membered rings were appended to the 8-membered ring. The Ga-Ga bond is considerably shorter and hence stronger than the As-As bond. Band structure calculations performed using a Vogl (1983) sp^3s^* Hamiltonian revealed deep states in the gap, which are associated with atoms in the core only.

Using Stadelmann's (1987) EMS program, successful image matching of calculated images of the [001] dislocation has been achieved with the experimental image, using the atomic structure generated by tight binding relaxation. Ga and As being only two atomic numbers apart have similar scattering factors and cannot be easily distinguished in the experimental image. The equivalence of the position of the two wrong bonds greatly eases image matching as it is no longer necessary to know which is the Ga-Ga , and which is the As-As bond.

This is the first suggested model of the [001] dislocation in GaAs, to the best of my knowledge. It is found to be similar to the atomic structure of the 90^0 partial dislocation in silicon (Bigger *et al.*, 1992). No account of segregation of impurities to the grain boundary, or the [001] dislocation core is taken here, though it is very likely that an impurity atom would sit itself in this large space.

The relaxed atomic structure for the 60^0 dislocation showed a doubling of periodicity along the dislocation line, similar to that found in the 30^0 partial in Si. The core consists of a 7-membered and a 5-membered ring with a minimum of two wrong bonds.

In addition to this, quantitative comparisons of the [001] HREM image and simulated structures have been made and an iterative structure refinement carried out in order to achieve the best image matching. The resultant 'experimental-best-fit' structure was not found to be physically or chemically plausible.

Preface

This thesis is an account of the work undertaken by the author in the Department of Materials, Oxford University, between March 1990 and September 1994, under the supervision of Drs. A. P. Sutton and C. R. M. Grovenor. The work has been supported by a Radhakrishnan Scholarship awarded by the British Council.

This thesis has not been previously submitted for a degree at this or any other university. Part of the work contained in this thesis will be submitted for publication. The work of others has been freely drawn upon and is duly acknowledged in the text. A full list of references is compiled at the back of this thesis.

Declaration

The body of the text of this thesis contains fewer than 40,000 words.

Acknowledgements

It is a difficult task to adequately thank the many friends, colleagues and organizations for the role they individually played from the initiation of this work till its completion. At the outset I must state that if by some oversight I have forgotten to mention someone, it is not for lack of wanting.

Professor P.B. Hirsch FRS, Professor J.W. Christian FRS, Professor J. Brook OBE and Professor D.G. Pettifor I wish to thank not just for the provision of laboratory and computing facilities, but more so for creating an amiable and constructive environment in which students can learn and grow.

The Radhakrishnan Trust and Wolfson College I thank for financial support.

A great deal of thanks to the very happy group of Professor M. Rühle at MPI, Stuttgart, Germany. In particular to Günter Möbus, Gabi, Frank Earnst, Dirk Hoffmann and Mike Finnis. I wish to thank everyone of the group for making me so welcome.

It is hardest of all to thank my supervisors, Drs. A.P. Sutton and C.R.M. Grovenor for the many varied roles they have played. In particular for their support, crucial guidance and for always 'being there' when I needed them.

Special thanks are also due to Marta Ramos, Duncan McInnes and Jim Bigger for familiarising me with FORTRAN programming in the first years. For all subsequent last-minute help I relied a great deal on Chris Goringe and his ever-willing attitude. And to Tchavdar for inspiration!

On the HREM side, I learnt a great deal from Dr. J.L. Hutchison, Dr. Amanda Petford-Long and from Dr. Linda Romano. Thanks to Dr. Neil Long I have got all my large computer jobs done with ease.

The Materials Modelling Laboratory is to be thanked for the computing facilities it offered me. In particular, thanks to Dr. Tony Paxton for discussions and to Dr. Mike Fearn for helping me with BOP. Thank you to all at the OUCS advisory desk for the timely help.

Dr. Peter Wilshaw I thank for helpful discussions and for together setting up the chemical thinning unit.

Thanks are due to Mr. G. Dixon-Brown, Mr. R.C. Doole and Mr. P. Hambridge for the maintenance of the electron microscopes, Mr. J.M. Short for his kind help in the students' workshop and Mr A.H. McKnight and Mr. M. Taheri for their photographic work.

Special thanks to Professor and Mrs M.A.E. Dummett for the regular jokes and wonderful tea times, apart from their concern for my well being.

I wish to thank Appa, Amma, Anu, Anju and Mitu for giving me such a wonderful family.

And I wish to thank dear Giri for his love, understanding, and friendship.

Contents

1 A Review of Grain Boundaries in Semiconductors **1**

1.1 Introduction 1

1.2 Grain Boundary Geometry and Related Terminology 2

1.2.1 Boundary Energy and Misorientation 5

1.2.2 The Coincidence Site Lattice (CSL) 6

1.2.3 Bicrystallography 9

1.2.4 The Structural Unit Model 10

1.3 Experimentally Observed Grain Boundaries in Semiconductors 12

1.3.1 Low Angle Grain Boundaries 14

1.3.2 HREM of Grain Boundaries in Gallium Arsenide 15

1.4 Computer Modelling of Grain Boundary Structure 17

1.5 Objectives of this Thesis 18

2 Background to the Experimental Work **20**

2.1 Crystal Structure 20

2.2 Dislocations in Semiconductors 21

2.3 Dislocation Core Reconstruction 24

2.4 Deep Levels at Dislocation Cores 25

2.5 Experimental Techniques 26

3 Theoretical Background to the Study 29

3.1 Introduction 29

3.2 The Tersoff Potential 31

3.3 The Tight Binding Energy Minimisation 32

3.3.1 Scaling Laws 35

3.3.2 Molecular Dynamics (MD) 37

3.4 Bond Order Potentials (BOP) 38

3.5 Summary 39

4 Low Angle Grain Boundary 40

4.1 Introduction 40

4.2 The specimen 40

4.2.1 Orientation 40

4.2.2 Preparation 41

4.3 The imaging conditions 42

4.3.1 The Jeol 4000EX 42

4.3.2 Microscope Alignment 44

4.4 The Geometry of the Grain Boundary 49

4.5 Geometric Construction of the [001] Edge Dislocation 52

4.5.1 The 446 Atom Supercell 53

4.6 The 336 Atom Supercell 54

5 The [001] edge dislocation 58

5.1 Introduction 58

5.2 HREM Image Simulation 59

5.2.1 The EMS Program 61

5.2.2 Simulation of perfect crystal images 62

5.2.3 Simulation of [001] edge dislocation 67
5.3 Relaxation of the [001] dislocation 76
5.3.1 Relaxation using a classical potential 76
5.3.2 The Bond Order Potential (BOP) relaxation 79
5.3.3 The Tight-binding relaxation 80
5.4 Band structure and electronic states 83
5.5 Summary and Conclusion 88

6 The Undissociated 60^0 Dislocation **90**
6.1 Introduction to 60^0 Dislocations 90
6.1.1 Geometry of the supercell 93
6.1.2 The Atomic Relaxations 97
6.1.3 The Tight Binding Relaxation 98
6.2 Image simulation of the 60^0 Dislocation 98
6.3 Conclusion 102

7 Other Experimental Work and Suggestions for the Future **103**
7.1 Other Work 103
7.2 Suggestions for Further Work 108
7.3 Closing Remarks 109

A The Median Lattice **110**

B The Contrast Transfer Function **113**

C List of Input Parameters used in the Atomic Relaxations **117**
C.1 The Tersoff Potential 117
C.2 The Bond Order Potential 118

D The 336-atom Supercell 122

REFERENCES 131

List of Figures

1.1 Structure of a symmetric tilt boundary. An array of edge dislocations forms a boundary whose axis is perpendicular to the plane of the page. θ is the misorientation angle, D the distance between the two dislocation cores of the Burgers vector **b**. 4

1.2 Structure of a twist boundary made up of a cross-grid of screw dislocations. The plane of the figure is parallel to the plane of the boundary and the open and closed circles represent atoms of either grain. 4

2.1 A unit cell of GaAs showing the sphalerite structure comprising two f.c.c sublattices shifted by $(\frac{1}{4}, \frac{1}{4}, \frac{1}{4})$ with respect to each other. 21

2.2 A) A projection of the diamond cubic lattice along [110]. B) Formation of a shuffle dislocation by removing material contained in 1234. Note that the two extra half planes of atoms terminate between the widely spaced $\{111\}$ planes. C) Formation of a glide dislocation by removal of 1564. Note that the two extra half planes of atoms terminate between the narrowly spaced $\{111\}$ planes. 23

2.3 A) A projection of the reconstructed 90^0 partial in the $\{111\}$ plane in Si, obtained by atomic relaxations performed by Bigger *et al.* (1992). B) The $\{111\}$ projection of the reconstructed 30^0 partial in Si, obtained from atomic relaxations. Note the bond reconstruction along the dislocation line, leading to period doubling. The filled and empty circles represent atoms on either f.c.c. sublattice. 25

2.4 A dark field image of a low angle grain boundary showing the presence of dislocations. 28

3.1 A) s^2p^2 state of an isolated Si atom. B) The occupation of s and p orbitals by one and three electrons achieved by promoting one s electron to a p-state. 34

3.2 A) General form of the scaling law used in the tight binding scheme. Note the smooth termination to the scaling for the hopping integrals and the pair-potential within the tight binding scheme. Atoms can move in and out of r_t without introducing discontinuities in the force. B) Scaling law used for GaAs. 36

4.1 The contrast transfer function for the Jeol 4000EX at two different defocal values of a) -471 Å and b) -720 Å. Note the span of the plateau (i.e., region of same contrast) and the d-spacing of the GaAs planes shown at the base of both figures. 43

4.2 The [110] diffraction pattern for a diamond cubic structure with the indexing of some beams. Other spots can be indexed by symmetry. . . 45

4.3 A) The dark field image of a grain boundary in GaAs, showing the presence of dislocations. B) The corresponding bright field image of the same grain boundary. 47

4.4 A photograph of the image of a 11.5^0 grain boundary about [110], recorded at Scherzer defocus along the [110] orientation. The diffraction patterns from grain A and grain B are inserted, as is the selected area diffraction pattern at the boundary. 48

4.5 An enlargement of the boxed area in Figure 4.4. Some directions are marked on the grains. Some dislocations are marked out with arrows; others are left unmarked for clearer viewing. 50

4.6 A) An illustration of the desired supercell dimensions for modelling the [001] dislocation. Consider a lattice site, A, and travel along $[\bar{7},7,1]$ one period of the boundary to C. Now, in this distance the displacement in either grain would be $|\mathbf{b}|/2$, where **b** is the net Burgers vector per period of the boundary, which is shown by AB and AD. Then, since C lies on a lattice site we are certain that the periodicity of the boundary is satisfied so long as there are 2[001] dislocations in one $[\bar{7},7,1]$ period. B) A schematic diagram illustrating the required supercell height to match the grain boundary periodicity. (After Bigger, 1993). 55

4.7 A [110] projection of the 446-atom supercell containing two [001] dislocation dipoles per boundary period. The As atoms have been shown larger than Ga in order to distinguish the two. 56

5.1 Simulated images of the perfect GaAs lattice at varying thickness and defocus. These images were obtained by the EMS package (Stadelmann, 1987), using the parameters given in Table 5.1. A) A coarse thickness-defocus variation. Also shown is the projected potential inserted at the bottom left of the figure. Image 'l' was chosen for image matching. B) Small variations around the image at 13.6 nm thickness and Scherzer defocus. 64

5.2 The digitised image of the grain boundary. Boxes A, B and C are drawn in to facilitate superposition of simulated images contained in the envelope attached to the back cover of the thesis, on the perfect crystal region, the [001], and the 60^0 dislocations. 65

5.3 The difference image obtained from the comparison of the simulated image '1' and the perfect crystal region in one grain of Figure 4.5. . . . 66

5.4 The [110] projection of the 336-atom supercell containing a [001] dislocation dipole. This supercell has been relaxed using Chadi parameters for GaAs with a k-space tight binding code. The red spots mark the As atoms and the yellow the Ga. 68

5.5 A) The projected potential for the tight binding relaxed 336-atom supercell, under conditions given in Table 5.1. B) A thickness-defocal series of simulated images for the [001] dislocation, obtained from the tight binding relaxed 336-atom supercell. The defocus varies along a row from left to right in nm, and thickness increases along a column. 69

5.6 A quantitative comparison of A) The digitized experimental image and B) The simulated image cut to the correponding size. C) The difference image. D) The simulated image taking atoms to be in the 'experimental-best-fit' positions. E) The difference image between the digitized experimental image and the simulated image D. 71

5.7 A) A 54-atom block chosen around a [001] dislocation core for the iterative structure refinement procedure. B) A superposition of the 54-atom block on the digitized experimental image. Note the atom at the centre that is on a white region of the image and appears to require shifting. . 73

5.8 The net shift in the atomic positions of 10 pre-selected atoms from their initial structure to the 'experimental-best-fit' positions, indicated by arrows. 75

5.9 A [110] projection of the reconstructed [001] dislocation core. The bonds have been indexed to facilitate reference to them in the text and tables. 78

5.10 A comparative study of the relaxed cores obtained from the 336 atom supercell using a A) Tersoff scheme for Si and B) the tight binding **k**-space scheme for GaAs. 81

5.11 A comparative study of the relaxed cores obtained from the 446 atom supercell using A) Tersoff and B) BOP schemes for Si. 82

5.12 This figure illustrates the atoms associated with the states in the gap at the [001] dislocation core. Red circles are Ga and yellow correspond to As. See table 5.6 85

5.13 The projected band structure along the dislocation line for the 336-atom GaAs supercell relaxed by the **k**-space tight binding code and the Vogl sp^3s^* Hamiltonian. The dashed lines show the edges of the bulk valence and conduction bands. Note the presence of deep (0.72 and 0.99 eV) and shallow states in the gap. The deep states are associated with atoms at the core, as can be seen from Table 5.6 and these atoms are marked out in Figure 5.12. The shallow states have weight distributed over the core. 86

6.1 A [110] projection of the 672-atom supercell used in atomic relaxations. The supercell contains two 60^0 dislocation dipoles and its period is 2 [110]/2 along the line of projection. The As atoms are shown larger than Ga for clarity. 94

6.2 A) An illustration of the matching between the grain boundary periodicity and the supercell period along the boundary. B) Consider a grain boundary running along $[1\bar{1}0]$ as shown by line AC, generated by a set of **a**/2< 110 > dislocations. Per period, the boundaries in the supercell contain a net Burgers vector of **b**=**a**[001] and **b**=**a**$[00\bar{1}]$ respectively. The dislocations impart an equal and opposite displacement of **a**/2[001] in each boundary period to either grain, as shown at site C. From the triangle ABC or ADC, it is clear that a similar triangle of double the scale would have the vector B′C′ ending at another atom that is equivalent to the atom at site C. 96

6.3 An illustration of the 60^0 core obtained by atomic relaxation, with bond indexing. Above is a schematic diagram showing bond index 12, along the dislocation line. 99

6.4 A series of simulated images for the 672-atom supercell at varying thicknesses and defocii. The projected potential is shown at the top left. . . 101

7.1 A) An HREM image of a twin boundary in GaAs and B) the $[1\bar{1}0]$ projection of a twin boundary in an f.c.c. structure. Open circles represent atoms in the plane of the drawing and filled circles those in the layers immediately above or below. The reflection symmetry across the twin plane is suggested by the dashed lines connecting several pairs of atoms. 105

7.2 An HREM image of a 4^0 tilt boundary in GaAs about [110] with arrows marking some dislocation cores. 106

7.3 HREM imge of an 8^0 tilt boundary about [110] showing the presence of **a**/2 < 110 > dislocations. 107

A.1 a) The perfect median lattice in which a grain boundary is to be formed. b) Rotation of the surface normals about the rotation axis normal to the page. The normal to the mean boundary plane is **N**. 111

List of Tables

2.1 Dislocation types in the III-V semiconductors. 22

4.1 Box size effects on bond distortions in relaxed [001] dislocation cores in silicon. 57

5.1 Parameters used to simulate the perfect crystal images with the EMS package. 63

5.2 Shift in atomic positions resulting from iterative structure refinement. . 75

5.3 Variation in bond length with box size, potential and treatment. 79

5.4 Comparative percentage bond distortions in relaxed core structures of [001] dislocations, obtained for different potentials. * marks a Ga-Ga wrong bond, and # an As-As wrong bond. 83

5.5 Comparison of relaxed [001] dislocation core structures 84

5.6 Weighting and occurrence of localised states in the reconstructed [001] core obtained for tight binding relaxation. See Figure 5.12 for atom indexing, red spots indicate Ga atoms. 87

5.7 Charges on atoms in Tight Binding relaxation. The atoms are indexed as in Appendix D. 88

6.1 Current understanding of dislocations in Ge. 92

6.2 Current understanding of dislocations in Si. 92

6.3 Current understanding of dislocations in GaAs 92

6.4 Maximum and minimum distortions in the reconstructed perfect 60^0 dislocation core. 98

6.5 Comparative percentage bond distortions in relaxed core structures of perfect 60^0 dislocations obtained for different potentials. The two tight binding results are from the dislocation cores containing Ga-Ga and As-As wrong bonds respectively. * marks a Ga-Ga wrong bond and # an As-As wrong bond. Bond 12 is along the dislocation line. 100

C.1 Parameter set used for Tersoff (1988) potential for Si. 118

C.2 Parameters used for GaAs tight-binding. 121

Chapter 1

A Review of Grain Boundaries in Semiconductors

1.1 Introduction

The increasingly varied applications of semiconductors in the electronic industry give continued importance to the study of these materials and the defects that occur in them. Lattice defects are known to affect the mechanical and electrical properties of a material. Precise knowledge at a defect of the microscopic and macroscopic differences relative to the bulk make possible the controlled exploitation of these effects in device design. For example, molecular beam epitaxy (Esaki and Tsu, 1970) can be used to form artificial semiconductor multi-layers designed to have a desired band gap.

Applications of polycrystalline semiconductors and of compound semiconductors used as solar cell materials have been reviewed by many workers (Ghosh *et al.*, 1980; Fahrenbruch and Bube, 1983). A polycrystalline semiconductor thin film is easy to deposit and is found useful as an interconnecting material, but knowledge of the effect of the grain boundaries becomes essential. Much experimental work has been done to measure the macroscopic properties such as the I/V characteristics and recombination efficiency in the presence of a defect. Efforts to relate the macroscopic properties to microscopic structure were reviewed by Grovenor (1985). The effects are directly

attributable to the intrinsic structural disorder of the boundary and the possible modifications of the local chemistry or stoichiometry.

Research on grain boundary structure has largely been carried out for grain boundaries in metals (Sutton, 1984; Vitek, 1988), nevertheless, a few reviews of the research of grain boundaries in covalently bonded semiconductors do exist (Sutton, 1989; Werner and Strunk, 1991 and references therein).

1.2 Grain Boundary Geometry and Related Terminology

A polycrystalline material consists of an aggregate of misoriented single crystals, the interface between the two crystals being defined as a grain boundary. Typically a solid will contain many different grain boundaries, but it is possible to grow a bicrystal (Matare, 1960) containing a specific boundary and to study its electrical and geometric nature.

There are at most six macroscopic geometrical degrees of freedom associated with a grain boundary which define the orientation relationship between the two grains: two degrees in defining the rotation axis, one in defining the rotation angle and another two in specifying the normal to the boundary plane. The sixth degree of freedom is present in some bicrystals that have either crystal showing enantiomorphism. Here, inversion is the only way to transform one crystal to the other; rotation being unable to achieve it. In addition to these are the microscopic degrees of freedom which are related to the atomic structure at the interface; two degrees are associated with the relative translation of one grain with respect to the other parallel to the boundary and one degree is the grain boundary expansion normal to the boundary plane. For crystals other than those with a monatomic basis there is a further microscopic degree of freedom defining the position of the boundary plane in the crystal.

A common approach to studying and classifying boundaries is with respect to the structural and energy changes with misorientation, for example the systematic study of specific series of tilt boundaries in cubic metals (Sutton and Vitek, 1983).

The dislocation model of grain boundaries and its modifications are a widely used approach to characterise the boundary geometry using an array of dislocations (Frank, 1950; Bilby *et al.*, 1955), and to assess the boundary energy using the elastic theory of dislocations (Read and Shockley, 1950).

A boundary constructed geometrically by tilting two crystals about an axis which is parallel to the boundary plane is said to be a *tilt* boundary, while a boundary constructed by rotating one grain with respect to the other about an axis that is normal to the boundary plane forms a *twist* boundary. A pure tilt boundary may either be symmetric or asymmetric and its net dislocation content is purely edge in character. This is best understood in terms of the median lattice (see Appendix A). The mean boundary plane bisects the angle between the two boundary planes in the reference lattice. A *symmetric* boundary necessarily has a mirror plane of the perfect crystal as the mean boundary plane, and the form of the Miller indices of the boundary plane in either crystal is the same. It can be thought of as an array of edge dislocations of Burgers vector **b** as shown in Figure 1.1, and may also contain screw dislocations that cancel out to give no net screw component.

The grains on either side of the boundary are rotated by equal and opposite amounts about the Z-axis, the net misorientation being denoted by θ. If the spacing between the dislocations is D, then Equation (1.1) is the famous Frank's formula,

$$\mathbf{b}/2D = \sin(\theta/2). \tag{1.1}$$

When D is less than a few lattice spacings the individual identity of the dislocations is questionable and this corresponds to a *large angle* boundary. There is no sharp divide between large and low angle boundaries, but boundaries of misorientation greater

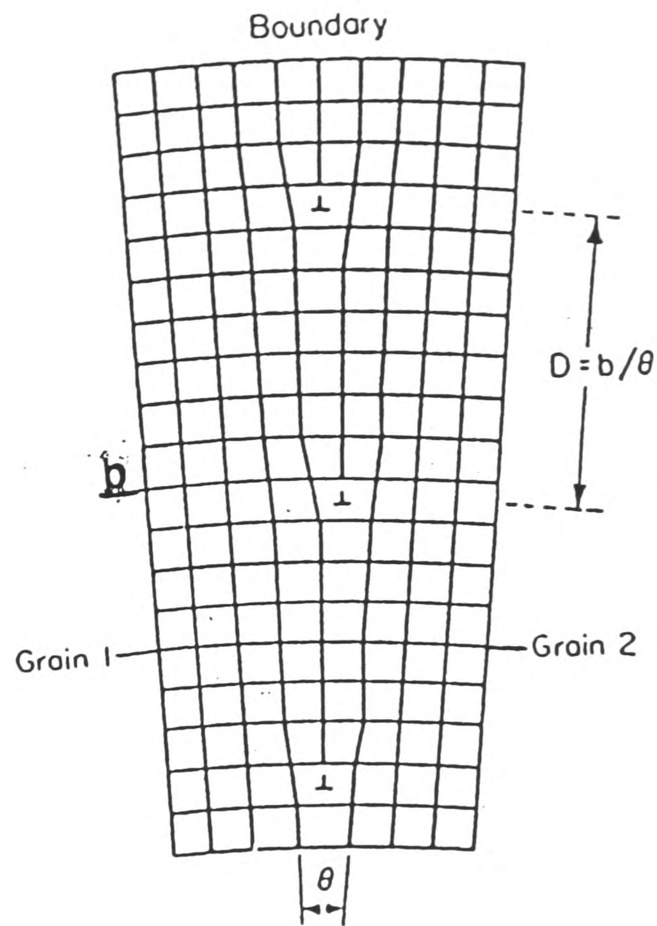

Figure 1.1: Structure of a symmetric tilt boundary. An array of edge dislocations forms a boundary whose axis is perpendicular to the plane of the page. θ is the misorientation angle, D the distance between the two dislocation cores of the Burgers vector **b**.

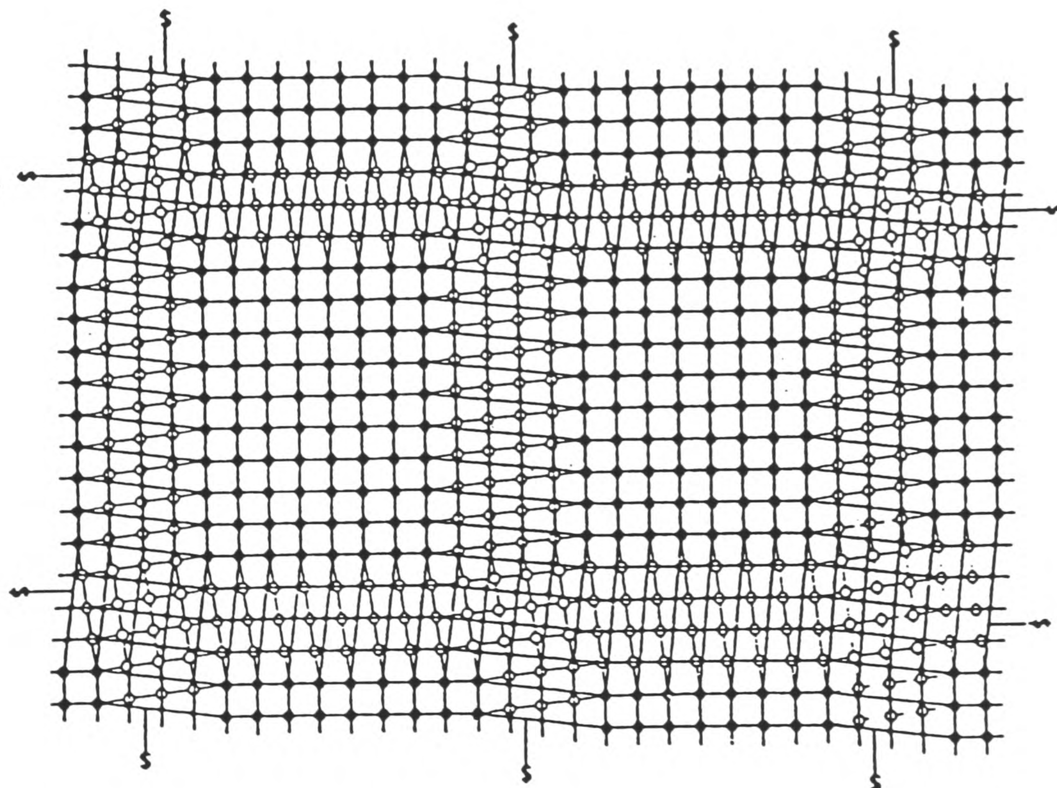

Figure 1.2: Structure of a twist boundary made up of a cross-grid of screw dislocations. The plane of the figure is parallel to the plane of the boundary and the open and closed circles represent atoms of either grain (after Read, 1953).

than $10 - 15^0$ have been referred to as large angle in the literature. *Asymmetric* tilt boundaries necessarily have a mean boundary plane that is not a mirror plane of the median lattice.

A boundary formed from a cross grid of pure screw dislocations is shown in Figure 1.2 and forms a pure twist boundary. It is not necessary for pure twist boundaries to be made up of pure screw dislocations; there is merely no net edge component. Boundaries in general exhibit a *mixed* tilt and twist character and have an array consisting of both edge and screw dislocations.

1.2.1 Boundary Energy and Misorientation

Read and Shockley (1950) modelled the energy of a low angle grain boundary suggesting that it was associated with both the strain field of the boundary (accommodated in a set of lattice dislocations) and the dislocation core energy. The elastic energy can be treated using a continuum theory of dislocations but evaluation of the dislocation core energy requires atomistic considerations. Frank (1950) modelled the geometry of the boundary and put forth his well-known formula, Equation (1.1), relating the misorientation angle to the separation between the dislocations associated with a symmetrical tilt boundary.

At high misorientation, according to the dislocation model, the energy is no longer given simply by the Read-Shockley formulation, though Frank's formula still holds. The problem arises due to the now relatively larger contribution of the dislocation cores to the grain boundary energy. Taking the energy difference as being due to the additional energy associated with any irregularity in the spacing of the primary dislocations, later developments of the Structural Unit Model enabled a Read-Shockley type estimation of boundary energy to be carried out for high as well as low angle boundaries (Vitek and Wang, 1985). They showed that both the position and the relative depth of the

cusps could be determined in the energy versus misorientation curve.

Frank (1950) and Bilby *et al.* (1955) developed the dislocation model to give the net Burgers vector density for a given misorientation and rotation axis that would be required to cancel out all long range stresses from either grain. Note that only the dislocation density, and not the individual dislocations, were characterized. The dislocation model of grain boundaries proved inadequate in providing an insight into the atomic structure of the boundary, as was shown by Christian and Crocker (1980), as a result of the non-uniqueness of the dislocation description for a given interface.

As of now, in the characterisation of a boundary, reference is made to parameters and concepts stemming from several different models. These models will be briefly outlined in the next section, with emphasis on the terminology that has outlived the models themselves.

1.2.2 The Coincidence Site Lattice (CSL)

A grain boundary can be considered to be composed of regions of fit and regions of misfit (Mott, 1948). In the dislocation model the misfit was taken up by dislocations in the boundary. The CSL concept considers the interpenetrating lattices of the two grains that form a bicrystal. If the two lattices have some lattice points in common, these are called 'coincidence lattice sites' (Pumphrey, 1976). A grain boundary may or may not give rise to coincidence lattice sites, depending on whether the orientation of the two grains is such as to relate them by a rational or irrational transformation matrix.

A boundary that has distinctive properties such as relatively low energy (as reviewed by Goodhew, 1980) was termed special. A boundary that was not special was termed random or general. Several geometric criteria associated with, and responsible for, the low boundary energy were put forth. Some of the factors were a low value of

Σ (Kronberg and Wilson, 1959) (Σ being the ratio of a unit cell volume of the CSL to the unit cell volume of the lattice of one grain), high coincidence site density in the boundary plane (Brandon *et al.*, 1964), and most significantly, large inter-planar spacings (Wolf, 1985) parallel to the boundary. Read and Shockley in their dislocation model had appreciated that a uniform spacing of lattice dislocations corresponded to a local minimum in energy, and these in the CSL model were known to be the coincidence site orientations. A special boundary was associated with periodicity and the presence of a coincidence site lattice. However, not one of these factors proved solely responsible for controlling the grain boundary energy when tested against experimental evidence. Sutton and Balluffi (1987) provide a good overview of the links made between boundary energy and geometry and they conclude that it is the atomic (not geometric) arrangement and bonding that are key factors in determining boundary energy.

If the orientation of the two grains at a boundary is such that they have vectors in common, then they may form a spatial lattice of the common sites called the coincidence site lattice, and hence also show periodicity. However, a slight rotation from this position is sufficient to destroy the coincidence. One of the main problems with the CSL representation lay in its discontinuity in, and susceptibility to, small changes in misorientation.

The specific parameter Σ (Grimmer *et al.*, 1974) and the grain boundary plane were used in the CSL model to characterise a boundary. In the CSL model no account is taken of the fact that in reality the atoms relax from the positions assigned in the geometrical construction of a boundary (defined by the CSL parameters of Σ and the boundary plane), hence destroying the coincidence sites. Rigid body translation parallel to the boundary plane (Smith *et al.*, 1977) is often found to occur during relaxation, and is not predicted by the CSL geometry. It leads to a different atomic structure and energy (Vitek, 1970; Bristowe and Crocker, 1975) for the same macroscopic boundary,

i.e., the same rotation axis, misorientation and boundary plane.

The limitation of the CSL representation to high coincidence, short period boundaries left a desire for a more complete structural representation of general boundaries. Although the parameter Σ is still used, the description of grain boundaries in terms of the CSL has been replaced by the more transparent Structural Unit Model (SUM).

Bollmann (1970) proposed the concept of the O-lattice which was similar to the CSL but a smooth function of misorientation angle, taking into account the coincidence of coordinates *within* a unit cell of one crystal and those of the other. This concept of the coincidence of empty space proved even less useful than the CSL, since the O-lattice assigned to a particular boundary depended on the choice of unit cells in both crystals and the transformation relating them.

Dislocations in a grain boundary were defined (Frank, 1950; Bilby *et al.*, 1955) with respect to a reference structure. For low angle boundaries it was the perfect lattice of the grains; the misorientation was incorporated by an array of lattice dislocations. For higher angle boundaries, it was easier to use a special boundary as the reference and describe the deviation from ideal coincidence in terms of dislocations in the CSL associated with it, called the Displacement Shift Complete (DSC) dislocations (Bollmann, 1970). DSC dislocations account for any irregular spacing of primary dislocations in a large angle boundary. Thus two types of dislocations were defined in high angle boundaries, namely primary or lattice dislocations and secondary or DSC dislocations. However, this DSC grain boundary description of a high angle boundary was thought to have little physical significance (Gleiter, 1977a,b), and corresponding transmission electron microscopy (TEM) observations to establish their existence (Pumphrey and Goodhew, 1979) are controversial (Vitek *et al.*, 1979). Owing to the choice of reference structure and to the various roles the dislocations were seen to play, several adjectives were used to describe them: intrinsic-extrinsic (Hirth and Balluffi, 1973), primary-

secondary (CSL concept), coherency-anticoherency (Olsen and Cohen, 1979), lattice, DSC and many more.

Bonnet (1985) developed a general description of the elastic field of an interface in terms of dislocations. The basic idea is to consider two types of dislocation arrays, one set that generates a long distance stress field and another that annihilates it. In the case where there are no long range stresses associated with the interface, in one period the two arrays must of course have equal and opposite net Burgers vectors, though the arrangement of the dislocations within the arrays may differ so as to obtain the lowest energy configuration. For an interface such as a grain boundary free of external constraints, there is no long range stress field and the Bonnet approach is seen as analogous to that of Read and Shockley by considering the rotation of the two grains as producing the long range stress field and the dislocations in the boundary plane as the annihilator array.

1.2.3 Bicrystallography

The symmetry shown by bicrystals was discussed by Pond and Vachlavas (1983) based on the theory developed by Shubnikov and Koptsik (1977). One advantage of this study was that an arbitrary reference structure was no longer required to describe the geometry of the interface. A new type of symmetry called 'colour symmetry' was defined for grain boundaries in which symmetry elements relate atoms of one crystal to the other. Using 'black' and 'white' to refer to lattice sites of one crystal and those of the other, ordinary symmetry elements relate black sites to black and white sites to white, while colour symmetry elements relate black sites to white. This system allows classification of bicrystals depending on the symmetry they show, analogous to the classification of a crystal based on the space group. For detailed geometrical analysis of a bicrystal based on bicrystallography see Pond and Vlachavas (1983).

1.2.4 The Structural Unit Model

This model was proposed by Bishop and Chalmers (1968) for metals. They suggested that the structure of grain boundaries in metals could be described equivalently by a two-dimensional array of coincidence atoms in the boundary plane (the CSL concept), a dense dislocation array (Frank, 1950) and by structural units. Three-dimensional arrangements of atom units form the core of a boundary, each unit corresponding to the core of a dislocation in the boundary. A structural unit is a group of atoms arranged in a characteristic configuration. For a given rotation axis, at particular angles the boundary is contiguously composed of units of one type only (Sutton and Vitek, 1983). Such a boundary therefore has a short period and is termed 'favoured'. Whereas boundaries had been classified as special (low energy) or general on the basis of energy considerations, they were later classified by Sutton and Vitek (1983) as favoured or non-favoured on the basis of structural considerations.

The basic idea was to consider large period boundaries as made up of distorted units of shorter period boundaries. The structural unit from a favoured boundary necessarily forms a fundamental structural element of nearby boundary structures. Boundaries that have a misorientation angle lying between those of two adjacent favoured boundaries of the same rotation axis are made up of linear combinations of the structural units constituting either. The sequence of units in a boundary is unique and is determined by the condition that minority units (defined below) are as widely spaced as possible.

Sutton (1981) and Sutton *et al.* (1981) applied this model to symmetric tilt boundaries in aluminium about $<110>$ lying in the range $\Sigma=11(113)$ 129.52^0 to $\Sigma=27(115)$ 148.41^0, and found that all the boundaries could be described by a linear combination of two structural units, say **A** and **B**. The delimiting boundaries were composed of only one type of undistorted structural unit each, either all **A** or all **B**, and were therefore

favoured boundaries. If the delimiting boundary was itself composed of a mixture of fundamental structural elements that were units of another boundary, it was called a 'multiple unit reference structure' (*m.u.r.s*) and was not a favoured boundary although it was a special boundary. In the range studied, it was found that the boundary structure changed gradually with misorientation, the number of times **A** units occurred in a period was a maximum for the misorientation closest to 129.52^0, and it gradually decreased to zero as 148.41^0 was approached, the **B** units increasing in number. The unit **A** thus changed from being a majority unit to a minority unit in boundaries in this misorientation range. Minority units may be considered as the cores of secondary grain boundary dislocations introduced to take up the deviation from the ideal coincidence of a delimiting boundary composed of majority units only. Further developments by Vitek *et al.* (1983) showed that multiplicity in grain boundary structure may exist with small differences in energy for the same macroscopic parameters. Since the energy difference is small, a boundary may contain regions of different structural modifications.

First applications of the SUM model to periodic tilt boundaries in Si were shown by Kohyama (1987). The structures were predicted at 0^0 K because vibrational energy was not taken into account. It was found that the SUM was best suited to predicting the structure and energy of pure tilt and pure twist boundaries about low-index rotation axes. For higher index rotation axes and mixed boundaries, it is less useful (Sutton, 1989) although it remains valid. Later Sutton and Balluffi (1990) studied grain boundaries of mixed nature and were further convinced of the need for a better model which has not yet been developed.

1.3 Experimentally Observed Grain Boundaries in Semiconductors

It has long been recognised that the understanding of interface properties strongly hinges on the availability of experimental information on the atomic scale at the interface. Atomistic simulations of planar defects have been carried out and tested against such experimental evidence. With modern HREM facilities it is now possible to obtain direct observation of many interfaces at the atomic scale. The procedures are discussed in Chapter 4; in this section a brief review of previous experimental work on semiconductor interfaces is given.

About two decades ago TEM was already in use for the study of interfaces in bicrystals. Young *et al.* (1973) used the orientation-sensitive Kikuchi patterns from each of the two crystals of Al-0.5 at.% Ag alloy to determine the misorientation axis and angle to an accuracy of $\pm 4^0$ and $\pm 0.1^0$ respectively. With the knowledge of the rotation matrix and the change in boundary images with tilting, the boundary normal was calculated. Prior to this method, this kind of analysis was done using the stereographic projection. These studies were restricted to characterising the macroscopic geometric parameters of a grain boundary.

If the orientation of the grain boundary is suitable, *lattice fringe imaging* can prove informative as fringes in both grains can be imaged simultaneously. This technique was used by Clarke (1978) to successfully image a grain boundary segment in a ZnO varistor ceramic. The boundary must be viewed edge-on and interference images contain features which can be considered as fringes at the positions of the lattice planes.

A 39^0 tilt boundary in Ge was directly imaged along [011] using HREM (Krivanek, 1978) and matched to a model consisting of a regular array of $\mathbf{a}/2[110]$ dislocations having no dangling bonds. The typical method at this time of comparing an experimental image with a model of the grain boundary was to compare a slightly blurred

picture of a ball-and-wire model with the image taken at the microscope. The earliest atomic level lattice plane imaging was possible in the [110] orientations of Si and Ge, where {111} lattice planes could be imaged in the bright field mode with nearly 3.1 Å resolution in a 100 kV type microscope (Bourret, 1982; Vaudin *et al.* 1983). Bacmann *et al.* (1985) studied the [001] Σ=5(1$\bar{3}$0) symmetric tilt boundary in Ge using the α fringe contrast analysis (Pond and Smith, 1976) combined with electron diffraction and proposed a boundary structure based on the structural unit model.

The most commonly seen large misorientation boundaries in polycrystalline semiconductor-grade Si are Σ=3(111), Σ=3(112), Σ=9(221), Σ=9(114) and Σ=27(552) about the $<110>$ rotation axis. They are all twin related and have boundary planes containing a high density of coincidence sites. The atomic structure of the Σ=3(111) coherent twin boundary (D'Anterroches and Bourret, 1984) has been determined by experimental and theoretical studies in Si and Ge. It consists of 6-membered rings in the $<110>$ projection and the atoms are not associated with any dangling bonds. The Σ=3(112) symmetric tilt boundary in Ge was observed by HREM techniques by Bourret and Bacmann (1985) and the atomic structure observed agreed very well with the theoretical model (Paxton and Sutton, 1989). The atomic structure of $\Sigma = 9(221)$ was imaged by Krivanek *et al.* (1977) and D'Anterroches and Bourret (1984). They found it to have the same qualitative structure predicted by Hornstra (1959) and the 5-membered and 7-membered rings expected from the structural unit model, but with some distortion in the rings which was attributed to oxygen contamination at the boundary. Cunningham and Ast (1981) imaged the dissociation of the Σ=27(552) into boundary segments of the $\Sigma = 9(221)$ and $\Sigma = 3(111)$, which presumably leads to a reduction in energy. They suggested that atomic faceting is favoured if the facets are on high density planes of the coincidence site lattice.

Sutton (1991) gives a list of large angle grain boundaries in Si and Ge observed

before July 1990. Most of these are symmetrical tilt boundaries. Here he also compares the HREM experimental observations (Putaux and Thibault-Desseaux, 1990) with theoretical predictions based on the Structural Unit Model. It was found that the structure of the $<110>$ (995) and $<110>$ (332) symmetric tilt boundaries observed by HREM had structures in agreement with the model at 1220^0 K, but at 1470^0 K the $<110>$ (332) symmetric boundary had a third structural unit not belonging to either of the two delimiting boundaries, and was therefore not in agreement with the SUM. This new unit was also found in the HREM image of $<110>$ (443) symmetric tilt boundary and can be found in a high energy configuration of the (111) twin.

Kim *et al.* (1992) carried out HREM and high spatial resolution AEM to analyze the structure and chemistry of $\Sigma = 13(510)[001]$ pure tilt boundary in a CZ silicon bicrystal. The atomic model of the grain boundary core structure has been described as a mixture of dislocations and the corresponding characteristic structural units. The Burgers vector of the primary dislocations of the boundary was $\mathbf{b}=\mathbf{a}[100]$.

Paidar (1992) made a geometrical study of asymmetrical $<110>$ and $<100>$ tilt grain boundaries in f.c.c. and b.c.c. crystal lattices. He found three types of boundaries: 1) the short period ones to which the structural unit model is applicable, 2) the exceptional asymmetrical boundaries that have large periodicity but cannot be decomposed into structural units from smaller period boundaries, and 3) the asymmetrical tilt boundaries that show no periodicity. Further theoretical and experimental work on asymmetric boundaries needs to be done.

1.3.1 Low Angle Grain Boundaries

The first low angle boundary in semiconductors to be imaged was in Ge (Vogel *et al.*, 1953) and it showed an array of dislocations, agreeing with Frank's model. Although the dislocation model for low angle boundaries was widely accepted, the Burgers' vec-

tors of the dislocations, their stability or dissociation in the boundary, and the stability of the boundary plane itself, were uncertain.

HREM was used to image [011] pure tilt boundaries with misorientations under 5^0 in Czochralski grown Ge bicrystals (Bourret and Desseaux, 1979), and the misfit dislocations were analyzed. The dislocations found were mainly undissociated edge dislocations with $\mathbf{b}=\mathbf{a}/2[0\bar{1}1]$, 60^0 $\mathbf{b}=\mathbf{a}/2<101>$ dislocations dissociated into 30^0 and 90^0 partials, $\mathbf{b}=\mathbf{a}/2<211>$ dissociated dislocations and a group of Frank partials with $\mathbf{b}=\mathbf{a}/3<111>$. The detailed core structures of these dislocations could not be ascertained at the resolution available at the time.

Carter (1981) observed many low angle tilt and twist grain boundaries in Si and Ge and analyzed the arrays of discrete dislocation cores. Carter *et al.* (1981) report that in tilt boundaries the Burgers' vectors found were: $a/2<112>$ and $\mathbf{a}<001>$. However, no attempt was made to interpret the $\mathbf{a}<001>$ image to reveal the atomic structure of the dislocation core.

1.3.2 HREM of Grain Boundaries in Gallium Arsenide

In compound semiconductors it is possible to have more than one type of boundary depending on the stoichiometry at the boundary plane. For example, an anti-phase boundary (APB) in GaAs can have all Ga-Ga or all As-As wrong bonds, or have an equal or unequal number of Ga-Ga and As-As bonds (Holt, 1969).

The $\mathbf{a}/2<110>$ dislocations in elemental semiconductors can be of two types, *glide* and *shuffle* dislocations. These are shown in Figures 2.2 A, B and C, and are distinguished by whether the dislocation lies in the narrowly spaced (111) planes or the widely spaced (111) planes of a diamond structure. The number of different dislocation types in III-V semiconductors is doubled compared to elemental semiconductors as the extra half plane can now end on a group III or group V element. The As dislocations

in the glide set and Ga dislocations in the shuffle set are called α dislocations, while the As dislocations in the shuffle set and Ga dislocations in the glide set are called β dislocations.

The *rigid body translation* across a Ga-Ga (111) APB facet has been determined by McKernan *et al.* (1991) using several 2-beam images, and is found to be normal to the boundary plane. The displacement was **R**=(0.0098±0.002) nm, in agreement with predictions based on a hard sphere model.

Carter *et al.* (1985) used HREM to image the $< 110 > \Sigma = 3(111)$ twin and [001] $\Sigma 5$ tilt boundaries in GaAs epilayers on {110} and {001} Ge bicrystal substrates, grown in a low-pressure organometallic vapour-phase epitaxy system. They found the $\Sigma 5$ boundary plane to facet onto {130} and {120} planes. The simulated structures of first order twins were determined by DeCooman *et al.* (1985) in agreement with experimental images. However, they made no statement regarding the distinction between the Ga and the As atoms. Liliental-Weber and Parechanian-Allen (1986) used convergent beam electron diffraction successfully to determine the crystal polarity in (011) GaAs samples, using the difference in the (200) and $(\bar{2}00)$ diffraction spots. Cho *et al.* (1987) then analyzed a $5^0 < 110 >$ tilt boundary using the convergent beam technique to show that all the edge dislocations had β type **a**/2[110] Burgers vectors.

$< 110 >$ tilt boundaries with misorientation less than 2^0 in Bridgman GaAs were investigated (Krakow and Smith, 1987) for their dislocation content. They found **b**=**a**[001] and dissociated dislocations with the net **b**=**a**/2[101] and **b**= **a**/2$[0\bar{1}1]$. They merely reported these findings and did not analyze them for the dislocation core structures.

While Burgers vector analysis and the periodicity of grain boundaries can be obtained directly from HREM images, the core structures at the boundary and dislocations cannot be ascertained without simulations. The main difficulty in looking at

grain boundaries in compound semiconductors as opposed to those in Si or Ge lay in the inability to grow the desired interfaces. The technique of hot pressing two single crystals together failed as GaAs dissociates incongruently at temperatures above 500^0C. One is therefore restricted to imaging naturally occurring grain boundaries in melt-grown GaAs, making a systematic study more difficult. Hence the theoretical predictions (Holt, 1964) of the structure of these boundaries preceded their experimental observation.

1.4 Computer Modelling of Grain Boundary Structure

The earliest calculations of the atomic structure at a grain boundary were carried out for metals, as a spherically symmetric bonding was easier to model than the directional bonding for covalent, four fold coordinated, semiconductors. For these cases, ball and stick models were built to study the possible core structures of dislocations in the diamond lattice with the desire to minimise the number of dangling bonds, bond bending, and bond length distortions (Hornstra, 1958). Hornstra (1959) later proposed structures of the $[1\bar{1}0]$ tilt grain boundaries in a diamond lattice of any misorientation, by using an array of dislocations and allowing the atoms to relax from their ideal coincidence positions. The structure of the Σ=3(111) twin was correctly predicted, and boundaries with high misorientations were shown to have smaller spacings between the dislocations. These early predictions were based on geometry rather than atomistic energy minimisations and are commendable for the qualitative insight they provided.

The early use of semi-continuum models (Frenkel and Kontorova, 1938; Peierls, 1940; Nabarro, 1947; van de Merwe, 1950) for the study of core structure of grain boundary dislocations was shown by Vitek *et al.* (1979) to be inappropriate. Nothing short of atomistic computer simulations was sufficient to predict the grain boundary

structure. Forms of inter-atomic forces were needed to incorporate relaxation of the atoms in any direction before an equilibrium structure could be computed.

Most of the models used in computational work for metals involved a central force pair potential or an N-body potential to correlate the energy of a system with the atomic coordinates. This energy is then minimised with respect to all the coordinates to obtain the equilibrium configuration at 0^0 K. Temperature dependence of the structure was later introduced by Sutton (1989); it is incorporated in molecular dynamic methods which include kinetic energy explicitly in the simulation, or Monte Carlo techniques where new configurations are accepted or rejected on the basis of a Boltzmann factor criterion.

The potentials used fall into three categories. The *ab initio* method (Car and Parrinello, 1985) involves first principle calculations of electronic structures to determine the atomic structure and total energy. This is the most accurate (though computationally demanding) method, treating fewer atoms than less accurate methods. *Empirical* methods such as the Stillinger and Weber (1985) and Tersoff (1986) for inter-atomic potentials should be used to provide qualitative results only. Here calculation of atomic forces and total energies is relatively simple and a large number of atoms can be dealt with. The *semi-empirical* tight binding methods such as that by Chadi (1978), the tight-binding bond model (Sutton *et al.*, 1988) and the self-consistent tight binding method (Majewski and Vogl, 1987) fall into the third category and have been successfully applied to semiconductors. The empirical and semi-empirical models used in this work are discussed in greater detail in Chapter 3.

1.5 Objectives of this Thesis

An approach combining theoretical and experimental atomistic investigations is certainly the most promising in studying interfaces. A theoretical prediction of electronic

states associated with a grain boundary and measurement of the electrical properties associated with these states would complete the picture. In this work I have imaged the [001]**a** and perfect 60^0 dislocation cores found in a low angle tilt boundary in GaAs, and analyzed their atomic and electronic structures. The simulated images of HREM observations of the expected structure were then compared with real images taken at the microscope and a good match was obtained. Electronic states associated with the defects are predicted by computer modelling but not experimentally measured.

In short, the thesis aims to use the latest tools available to take highly resolved images of grain boundaries in GaAs, and to analyze completely the images obtained to yield as much information as possible on structural and electronic properties. This is the first time that such a combined experimental and theoretical study of the atomic structure and electronic properties of the same grain boundary has been carried out.

Chapter 2

Background to the Experimental Work

2.1 Crystal Structure

The elemental semiconductors Si and Ge occur in the diamond cubic structure exhibiting the space group symmetry Fd3m. The III-V compound semiconductors such as GaAs and InP show the closely related sphalerite structure and $F\bar{4}3m$ space group symmetry.

The sphalerite structure consists of two interpenetrating f.c.c. sub-lattices, one sub-lattice displaced by (**a**/4,**a**/4,**a**/4) with respect to the other. In GaAs one of the sub-lattices is occupied by Ga atoms and the other by As atoms as can be seen from Figure 2.1 which shows a unit cell. Hence there are 8 atoms in a unit cell, 4 of each kind.

The loss of the centre of symmetry, found in the diamond cubic structure at a point lying half-way along a bond e.g. at (1/8,1/8,1/8), leads to significant differences in the properties of GaAs and Si. For example, the (111) plane with Ga atoms at the surface is distinct from the (111) plane with As atoms at the surface, one being known as the gallium face and the other the arsenic face, and the two are experimentally distinguishable by chemical techniques (Kyser and Millea, 1964). Similarly the [110]

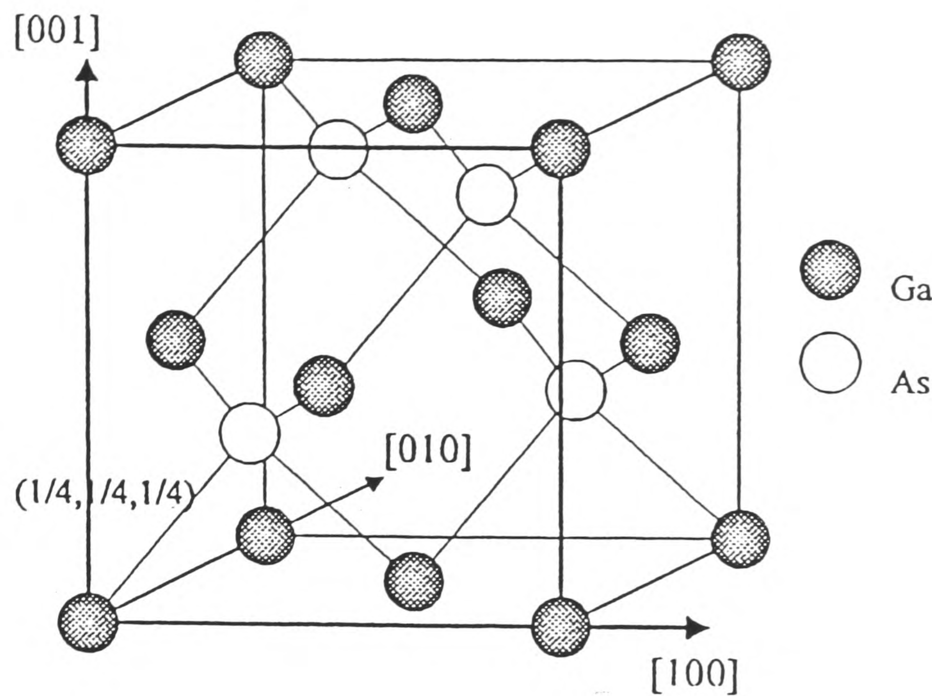

Figure 2.1: A unit cell of GaAs showing the sphalerite structure comprising two f.c.c sublattices shifted by $(\frac{1}{4}, \frac{1}{4}, \frac{1}{4})$ with respect to each other.

and $[1\bar{1}0]$ directions in the (001) plane have been distinguished by etching (Tarui, Komiya and Harada, 1971).

2.2 Dislocations in Semiconductors

As in the f.c.c. structures, the glide dislocations lie in $\{111\}$ glide planes, with perfect dislocations of Burgers vector $a/2<110>$, and the dislocation line usually along $<110>$. Characterising such dislocations by the angle between the dislocation line and the Burgers vector, dislocations are either screw type (0^0) or 60^0 dislocations. Use of weak beam microscopy showed that it was favourable for deformation induced perfect dislocations to dissociate into partial dislocations (Gai and Howie, 1974) in III-V semiconductors. The screw dislocation dissociates into two 30^0 partials separated by a stacking fault, and the 60^0 dislocation into 30^0 and 90^0 partials separated by the

Atom at end of extra half plane	Glide	Shuffle
Group III	Beta	Alpha
Group V	Alpha	Beta

Table 2.1: Dislocation types in the III-V semiconductors.

associated stacking fault. But, undissociated 60^0 dislocations in Si (Hutchison *et al.*, 1983) and GaAs (Tanaka and Jouffrey, 1984) have also been observed and reported.

Due to the diamond cubic stacking of {111} planes two kinds of dislocations are known to occur in silicon: the glide and shuffle dislocations (Hirth and Lothe, 1982). Depending upon whether the dislocation lies between the widely spaced or narrowly spaced planes it is termed a shuffle or glide dislocation respectively. Figures 2.2 A, B and C illustrate the distinction between the two types of dislocations. Experimentally it is far from trivial to distinguish between the two. When viewing the partial or perfect dislocation along its line direction, the difference between the shuffle and glide core types is given by one single atomic column in the glide case versus a dumb-bell of atoms in the shuffle case. Several attempts at determining whether a core is glide or shuffle have been made using high resolution electron microscopy, image processing and image simulation (Geipel, 1993) but no widely accepted technique of known accuracy has been established yet. Support for the occurrence of glide dislocations comes from the observation of glide of dislocations in the dissociated state (Gomez and Hirsch, 1977; Cockayne *et al.*, 1980; Feuillet, 1983).

In compound semiconductors there is yet another distinctive property of a dislocation. This comes from the fact that the extra half plane of a 60^0 dislocation may end on a group III or group V atom. Table 2.1 gives the nomenclature that was suggested by Alexander *et al.* (1979), and is still used.

Alternatively, Ga(s)/As(g) and Ga(g)/As(s) have been used to refer to the α and β

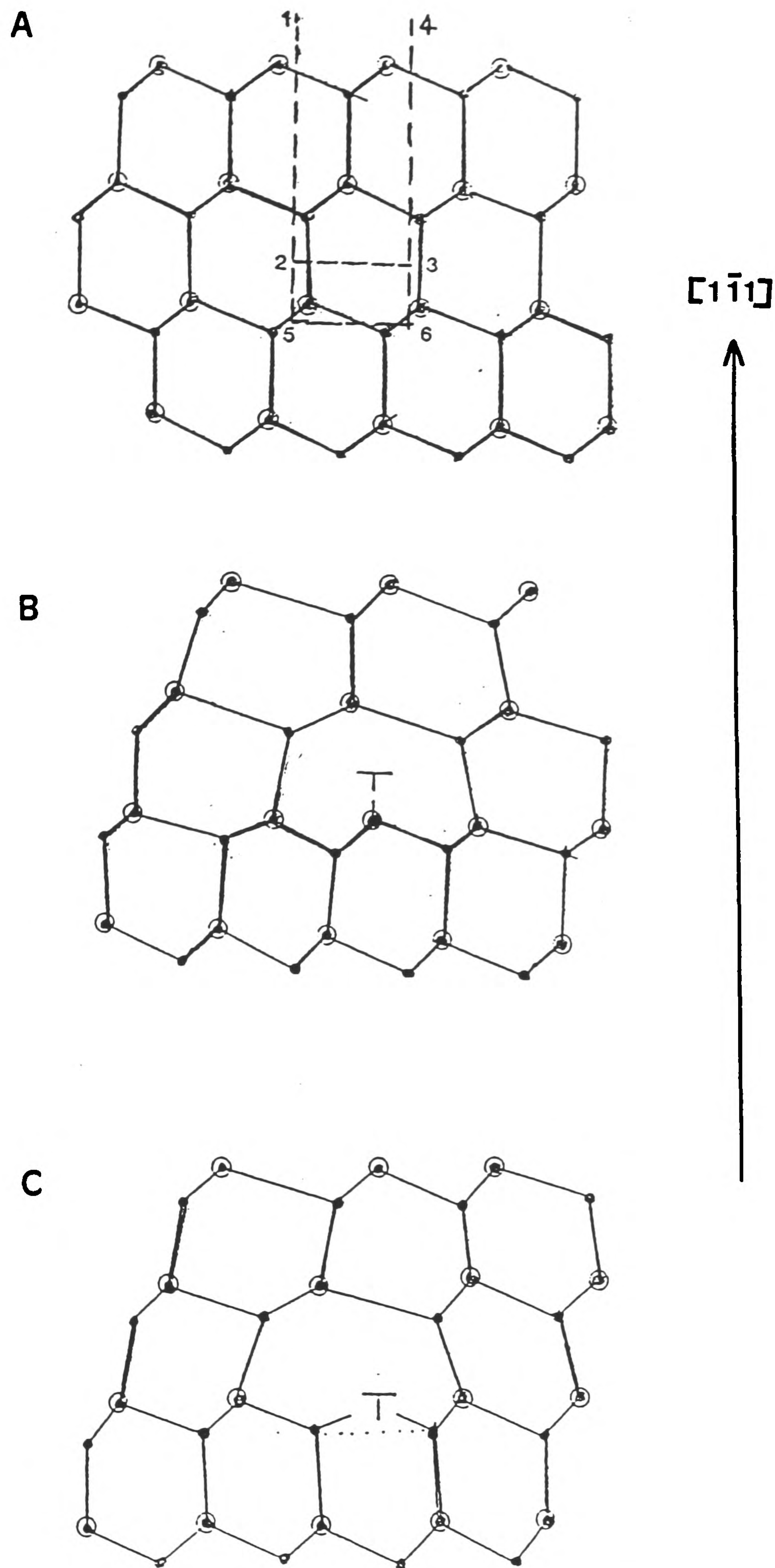

Figure 2.2: A) A projection of the diamond cubic lattice along [110]. B) Formation of a shuffle dislocation by removing material contained in 1234. Note that the two extra half planes of atoms terminate between the widely spaced {111} planes. C) Formation of a glide dislocation by removal of 1564. Note that the two extra half planes of atoms terminate between the narrowly spaced {111} planes.

dislocations, where s and g stand for shuffle and glide respectively. 30^0 partials in GaAs were found to be of the glide type by HREM techniques by Gerthsen *et al.* (1989).

In order to understand the differences in the α and β dislocations their dissociation widths and stacking fault energies were of prime interest to the microscopists. However, no differences in the dissociation widths were found for the 60^0 dislocation in GaAs (Gomez and Hirsch, 1978) nor in II-VI compounds (Lu and Cockayne, 1986). Studies in Si showed that the experimentally observed dissociation width was much larger than expected for Si quenched from high temperature. It was concluded that the 30^0 and 90^0 partials had different mobilities and their mobility also depended upon whether they were moving toward or away from the stacking fault. Whether partial mobilities in GaAs differ in a similar manner is not yet known.

2.3 Dislocation Core Reconstruction

Geometrically, addition or removal of a half plane of atoms gives rise to an unreconstructed core containing broken bonds. In reconstruction the atoms at the dislocation core relax into a structure that is more energetically favourable, where the bond bending and bond distortion is low. There is a trade-off in energy between the lowering in energy due to bond formation (as opposed to a dangling bond) and the increase due to strain. Calculations by various groups (Jones, 1979; Marklund, 1979) have independently shown that reconstruction is favoured in Si.

In the 30^0 partial in Si bond reconstruction occurs along the dislocation line, so doubling the periodicity along the dislocation line. In the 90^0 partial in Si, Bigger *et al.* (1992) showed that an asymmetric reconstruction of the core, as was originally proposed by Hirsch (1979) and Jones (1979), is likely to be found. Figures 2.3A-B show projections of the reconstructed 30^0 and 90^0 cores in Si. Reconstruction of partials in III-V compounds is necessarily different as it would involve like atoms bonding along

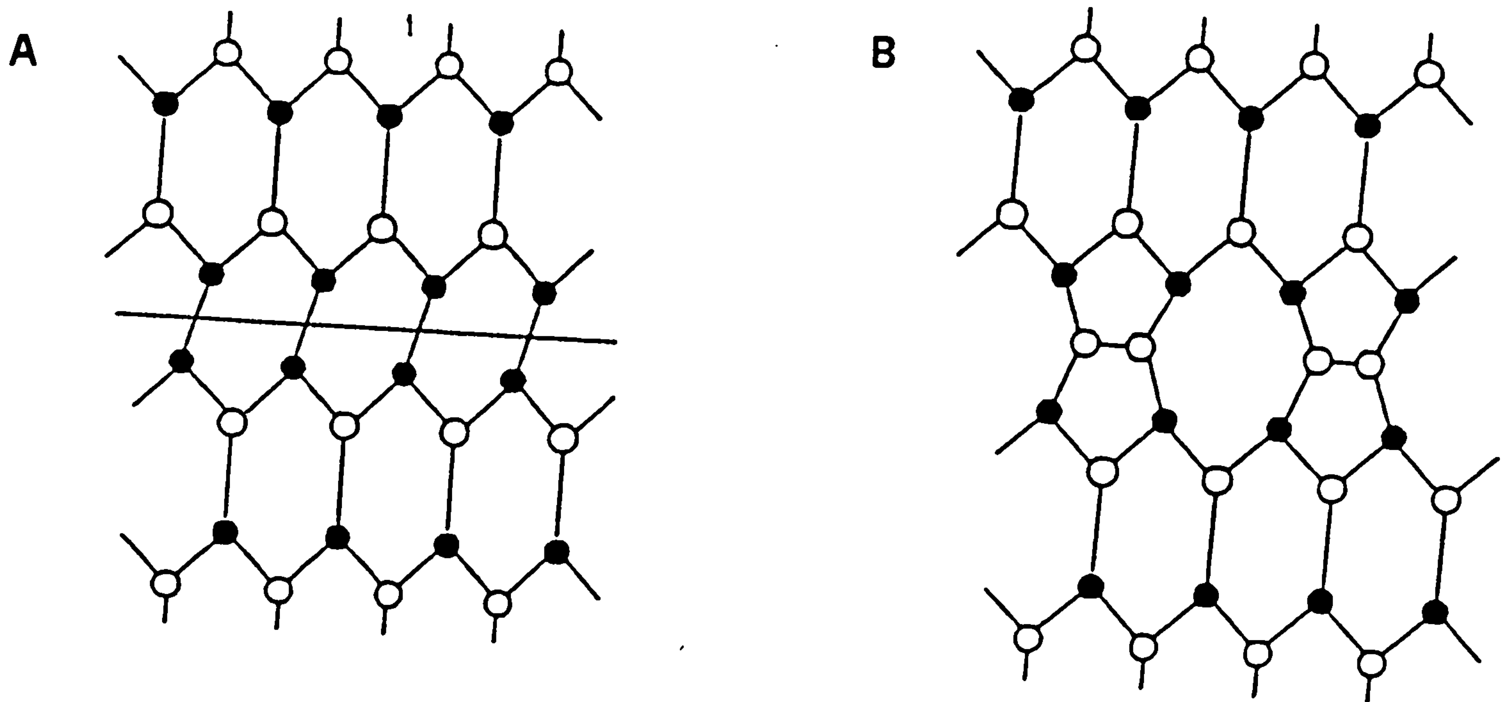

Figure 2.3: A) A projection of the reconstructed 90^0 partial in the {111} plane in Si, obtained by atomic relaxations performed by Bigger *et al.* (1992). B) The {111} projection of the reconstructed 30^0 partial in Si, obtained from atomic relaxations. Note the bond reconstruction along the dislocation line, leading to period doubling. The filled and empty circles represent atoms on either f.c.c. sublattice.

the dislocation line. Some attempts have been made by Jones (1981) and Jones *et al.* (1981) to find out how reconstruction occurs in 30^0 α and β partials and also for the 90^0 α and β partials.

2.4 Deep Levels at Dislocation Cores

Shockley (1953) suggested that a line of broken bonds at a dislocation core constituted a one-dimensional half-filled band located somewhere in the band gap. If the bond is reconstructed then the 1-D band splits into a full donor band and an empty acceptor band separated by a dislocation band gap. If the distortion at the core is small the donor band will lie close to the valence band of the perfect crystal structure and the

acceptor band close to the conduction band. The occupation of the states introduced by the dislocation is determined by the Fermi level relative to the dislocation band level. States below it are occupied and those above it empty.

Many experimental techniques have been used to study the electrical properties of dislocations, but there are difficulties in studying isolated dislocations. The electron paramagnetic resonance technique can allow the number of unpaired electrons in different states to be calculated, but the energy level of the partially occupied state is not determined. Alexander *et al.* (1983) used this method for Si deformed at 420^{0}C to find that less than 0.2% of the dislocation associated states were occupied. Deep level transient spectroscopy (DLTS), Hall effect and photoconductivity measurements are other means used to investigate the deep levels. Wilshaw (1984) and Wilshaw and Booker (1986) reported states at or deeper than E_c-0.5 eV in screw and 60^0 dislocations in Si.

In compound semiconductors the studies are not in agreement with each other and little can be said conclusively yet. In a study on highly deformed GaAs, Wosinski (1989) detected a dislocation state in the upper region of the band gap (ED1= E_c-0.68 eV) for specimens deformed at 400^{0}C to a strain greater than 3%.

2.5 Experimental Techniques

Transmission electron microscopy (TEM) concerns the formation of an image by high energy electrons that have been transmitted through a thin solid. In crystalline materials the interaction between the electrons and the crystal scatters electrons in the form of one or more diffracted beams. One or more of these beams is then used for image formation. Strain contrast in the image arises from local variations in the scattering from the lattice planes and Z-contrast arises from a difference in scattering from atoms of different atomic numbers. Two methods, diffraction contrast or phase contrast can

be used to produce contrast in a TEM image. In diffraction contrast an aperture in the back focal plane of the objective lens is used to select one electron beam which is used to form the image. The beam can either be the transmitted beam that forms a bright field image or a diffracted beam that gives rise to a dark field image (for example, Figure 2.4 showing the presence of dislocations at a boundary, also showing thickness fringes in the grain in which diffraction conditions are set up). The intensities in the image are then proportional to the square of the amplitude of the single beam that passes through the aperture. In the two beam dark field diffraction condition the sample is tilted so that only one diffracted beam is strongly excited.

In phase contrast microscopy (HREM) the sample is tilted so that the electron beam is aligned along a major crystallographic direction (a pole) in the crystal. The image is formed by several diffracted beams recombined with the transmitted beam in order that phase differences in the waves at the exit surface of the sample are converted into intensity differences in the image. The intensities in the image are therefore a combination of phase changes (interference effects) and amplitude changes.

The theory of electron microscopy and associated imaging has been comprehensively described in several excellent books (e.g. Hirsch *et al.*, 1977). The standard two beam diffraction contrast dark-field/bright-field techniques were used to take the micrographs shown in Chapter 4. HREM was employed to investigate atomic structure at defect sites. For details of HREM techniques the reader is referred to Chapter 4, and for a more detailed description to Appendix B and the book by Spence (1988).

Figure 2.4: A dark field image of a low angle grain boundary showing the presence of dislocations.

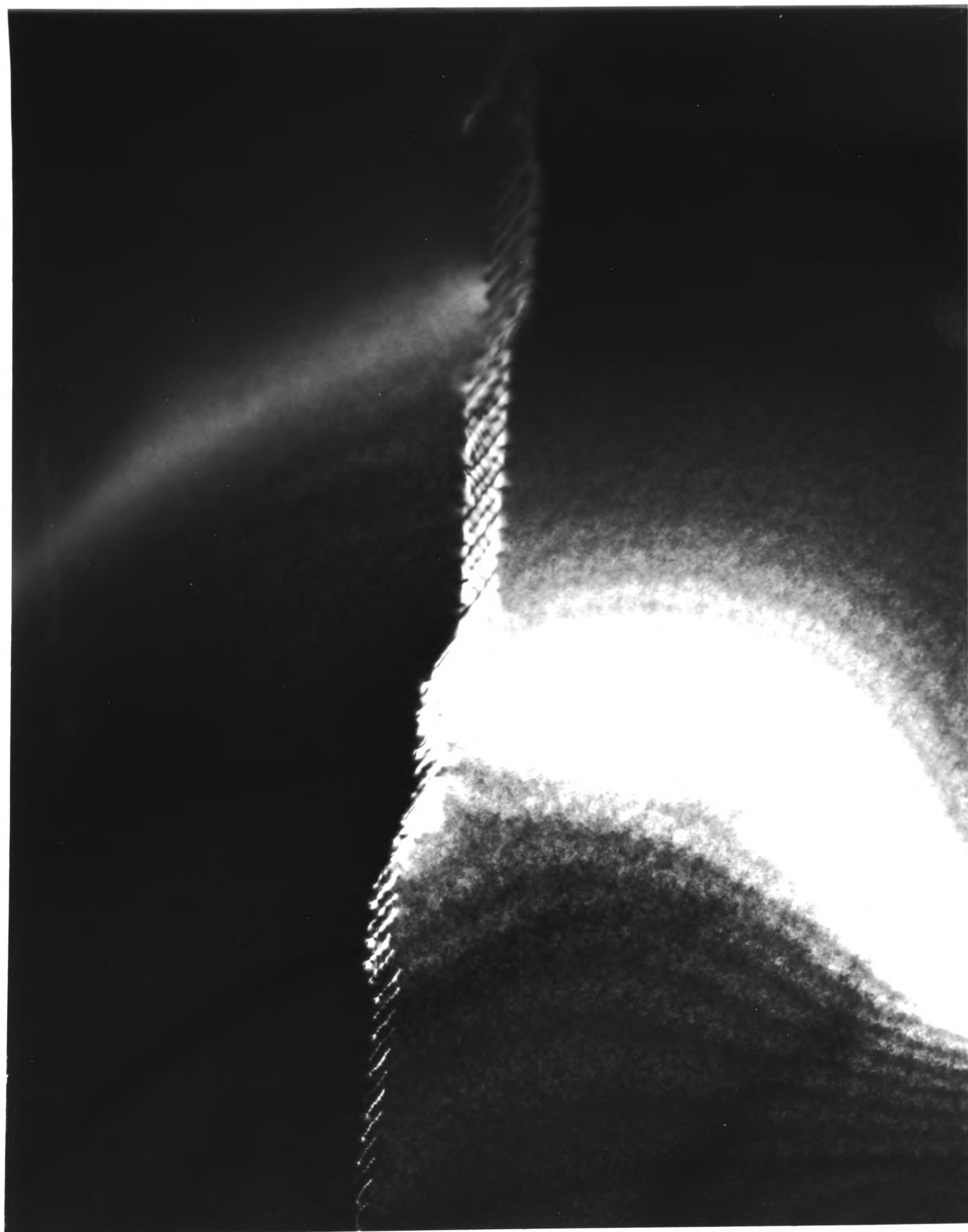

Chapter 3

Theoretical Background to the Study

3.1 Introduction

There is a growing link between those who are condensed matter electron theorists and those who manufacture useful materials such as semiconductor multilayers, as a result of the effective use of electron theory in predicting the properties of such materials, and in providing the conceptual basis for modelling the properties. This chapter aims at providing a general background to the theoretical approach used in the thesis, with an emphasis on why particular potentials have been used and what their limitations are. Anything short of solving the many body Schrödinger equation:

$$H\Psi = E\Psi \tag{3.1}$$

for the atoms that lie in the defect core is an approximation to reality and no matter how valid an approximation, it is vital to understand not only the degree to which it affects the result but also the properties it is most likely to bias. In the light of this it is understandable that when empirical or semi-empirical methods are used it is advisable to employ two or three different schemes and to seek agreement between their final results as I have done by using the Tersoff, Tight-Binding and Bond Order potentials. Basing a structure on a particular potential can easily lead to erroneous interpretation

of the results.

A standard method of obtaining the lowest energy configuration for a given block of atoms is to express the total energy (E) as a function of the atomic coordinates ($\mathbf{r}$) and to then minimise E with respect to $\mathbf{r}$. For example, consider a block of n atoms that interact with one another. One way to express the total energy is as a Taylor expansion about the minimum energy (Keating, 1966), but this approximation is valid only so long as the displacements of atoms from their equilibrium positions is small. Alternatively, the total energy can be expressed as:

$$E = \sum_{i} V_1(\mathbf{r}_i) + \sum_{i,j} V_2(\mathbf{r}_i, \mathbf{r}_j) + \sum_{i,j,k} V_3(\mathbf{r}_i, \mathbf{r}_j, \mathbf{r}_k) + \cdots \tag{3.2}$$

where $\mathbf{r}_i$ is the coordinate of atom i. Although such an expansion is not rigorously justified it has been used, for example in valence force fields. The first term to the right gives the effect of an external potential on all the atoms, the second term is a pair potential incorporating the two-body interaction, the third term corresponds to a three-body interaction, and so on till the n-body interaction is included. In the absence of an external field acting on the system the first term reduces to zero.

Either the exact mathematical form of the interaction must be considered and the Schrödinger equation solved (ab initio methods), or less accurate semi-empirical or fully empirical methods used to obtain the preferred states of the system. Empirical methods involve expressing the interaction as a function of a few chosen parameters. The parameters are fitted to experimentally measured quantities such as the cohesive energy, elastic constants, stacking fault energy etc. which are bulk properties. The potential however, is used at strained sites such as defects and the applicability of the potential away from equilibrium must be questioned. In many cases only the two-body interaction is taken and this is called the pair potential approximation. Such a potential favours a close packed structure and is good for purely ionic crystals and rare gases.

Semiconductors, on the other hand, have a more open structure and show a large measure of covalent bonding. Covalent bonding is strongly directional and this is not taken into consideration in a spherically symmetric pair-potential which is merely a function of the distance between two atoms. Hence the pair potentials developed as early as 1925 (e.g. Lennard-Jones potential; for a detailed description of this see Seitz, 1940) for metals could not be extended to covalently bonded systems.

Stillinger and Weber (1985) included a three-body 'bond bending' term in the hope of describing covalent bonding. While their empirical model can describe some of the properties of Si, it fails to describe the non-tetrahedral polytypes of Si. It is a popular potential in Si modelling but its failures have been pointed out by Wilson *et al.* (1990) and Bigger *et al.* (1992) among others. The properties that an empirical potential can correctly predict are largely those which are directly related to the properties considered while fitting the parameters. Thus the validity of an empirical potential is known only through extensive usage.

3.2 The Tersoff Potential

Tersoff (1986) developed a new empirical interatomic potential for Si by considering in real space how the bond order is affected by the local environment, in an intuitive way. He fitted the parameters to highly accurate calculations obtained from Local Density Functional theory for the energies of the different polytypes of Si. The Tersoff potential is based on the concept of competing parameters: the bond order, bond angle and the coordination number. The bond order is proportional to the energy of a bond, the bond angle factor incorporates bond bending forces, and the coordination number is the number of neighbours to which an atom bonds. Generally, the larger the coordination number the weaker each bond is. Hence, there is a trade-off between having a few strong bonds, and having a larger number of weaker bonds. The bonding

that leads to the greatest reduction in energy is expected.

The potential first proposed by Tersoff (1986) was modified by him (Tersoff, 1988); it is the modified potential that has been widely used to give good qualitative results for the core structure of defects in Si such as the 90^0 partial in Si (Bigger *et al.*, 1992), 30^0 partial, undissociated 60^0 partial in GaAs (this work), and the [001] dislocation in GaAs (this work) and to predict the ground state properties in silicon at defect sites. The main drawback of the potential is that while it describes the formation of σ-bonds reasonably well it cannot describe the π-bonding, which can be important at defect sites in Si (e.g. at surfaces).

3.3 The Tight Binding Energy Minimisation

The tight binding approximation is useful in describing the valence d-band of transition metals and sp valent bands found in semiconductors such as Si or GaAs. The basic idea is to express the wavefunction as a linear combination of atomic like orbitals (LCAO).

In the tight binding scheme the total energy of a system of atoms may be expressed as follows:

$$E = E_{bs} + U_{rep} \tag{3.3}$$

where E_{bs} is the band structure energy given by the sum of the energies of occupied eigenstates of the system:

$$E_{bs} = \sum_{n \ occupied} E_n(\mathbf{k}) \tag{3.4}$$

where $E_n(\mathbf{k})$ is the eigenvalue associated with one electron state $|n\mathbf{k}>$, with wave vector $\mathbf{k}$ and band index n. The summation is carried out by sampling the Brillouin zone with a mesh in $\mathbf{k}$-space. When there is sufficient symmetry in the system a special $\mathbf{k}$-point technique (Chadi and Martin, 1976) can be used for the summation. The second term in Equation (3.3) is a sum of repulsive pair potentials (Goodwin *et al.*, 1989).

After expressing the energy of the system as in Equation (3.3) we wish obtain the forces as derivatives of the energy with respect to displacement of the atoms. The derivative of the pair potential is straight forward, and there are several techniques to obtain the derivative of the band energy. In all the work here the Hellmann-Feynman theorem (for details see Sutton *et al.*, 1988) has been used to obtain the forces.

In the tight binding approximation an overlap of the free atom orbitals (s,p,d,f) gives rise to valence and conduction band states in the solid. Since the atomic orbitals are related to the free atom size and electronegativity, and they have an angular dependence (except for the s orbital which is spherically symmetric), atomic properties are incorporated in bonding between atoms in the solid, and the atomic interactions are angularly dependent.

The one electron wavefunction is expanded as a linear combination of atomic orbitals (LCAO) in a basis set limited to including only those atomic states that have energies comparable with the valence band energy of the solid, as:

$$\Psi^{(n)}(\mathbf{k}) = \sum_{i\alpha} c_{i\alpha}^{(n)}(\mathbf{k})\Phi_{i\alpha} \tag{3.5}$$

where i gives the atomic site of the orbital and α its angular momentum character (s, p, d etc.) and n refers to the band index. In this thesis the basis used was a minimal sp^3 basis (Chadi, 1984) consisting of the one 3s and three 3p atomic states, unless otherwise stated. In an isolated Si atom the valence electrons are in the s^2p^2 state shown in Figure 3.1A. In order that all four electrons participate in bonding one of the s electrons is promoted to a p state as shown in Figure 3.1B. The four atomic orbitals mix so as to form four equivalent sp^3 orbitals and this is known as hybridisation. The sp^3 hybridisation leads to tetrahedral bonding being favoured. The degree of hybridisation depends on the offset of the gain in bond energy versus the promotional energy required. This limitation to the basis set translates into an incorrect prediction of excited states that lie in the conduction band. These are often of importance in

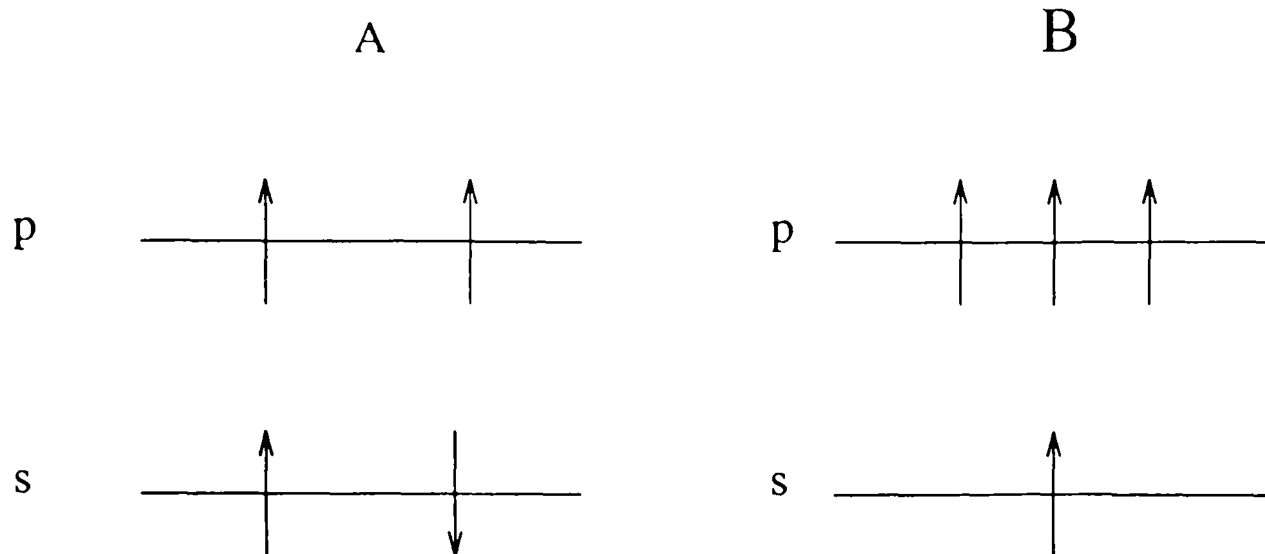

Figure 3.1: A) s^2p^2 state of an isolated Si atom. B) The occupation of s and p orbitals by one and three electrons achieved by promoting one s electron to a p-state.

seeing how the defect core may be associated with electronic states that lie in the gap. Vogl *et al.* (1983) showed that including an excited s state, s^*, does lead to corrected states near the lower end of the conduction band. This has been used in this thesis for calculating electronic energy bands in Chapter 5.

With this basis set the Schrödinger equation can be simplified into the matrix form:

$$\sum_{i\beta}(H_{i\alpha j\beta} - \epsilon^{(n)} S_{i\alpha j\beta}) c_{j\beta}^{(n)} = 0 \tag{3.6}$$

where $H_{i\alpha j\beta}$ and $S_{i\alpha j\beta}$ stand for the integrals $< \Phi_{i\alpha}|H|\Phi_{j\beta} >$ and $< \Phi_{i\alpha}|\Phi_{j\beta} >$ respectively. $S_{i\alpha j\beta}$ is the overlap matrix which can be made into an identity matrix by assuming the atomic basis set is orthnormal. This is a simplification justified by chemical pseudopotential theory (Heine and Hafner, 1980).

The other integral involves the Hamiltonian and it consists of several types of interactions:

- The interaction between orbitals on the same atom due to the crystal field potential. The crystal field potential is the average potential due to the rest of the atoms in the solid, which is seen by the atom under consideration. There are two kinds of matrix elements here $< \Phi_{i\alpha}|H|\Phi_{i\alpha} >$ and $< \Phi_{i\alpha}|H|\Phi_{i\beta} >$, of which the latter is assumed to be zero.

- The hopping integral which gives the interaction between two orbitals on different atoms via the potential field of one of the atoms.

- The interaction between two orbitals on different atoms via the potential field of a third atom. Pettifor (1977) showed that this term is second order in the energy, and it has usually been ignored (Slater and Koster, 1954).

In the tight binding scheme used, none of the integrals were evaluated. They were treated as parameters to be fitted to the band structure obtained experimentally and also to accurate local density functional calculations at high symmetry points in the Brillouin zone. As with other empirical schemes discussed it shares the problem of transferring these integrals, parameterised for the perfect crystal, to a defect environment where the crystal potential will clearly be altered.

3.3.1 Scaling Laws

Since the integrals are treated as fitted parameters, it is necessary not only to define their values, but also how the interaction scales with distance. These are known as scaling laws and are of vital importance in determining the final relaxed structure (Paxton and Sutton, 1989). The scaling for the tight binding scheme used in this work is shown in Figures 3.2A-B. In the vicinity of the nearest neighbour separations the repulsive pair potential has a radial dependence of the form r^{-4} and the hopping integrals the r^{-2} form. The smooth scaling was developed by McInnes (1992) by attaching a fifth order polynomial at a nodal distance r_n to ensure a gradual fall to zero potential at a termination radius r_t. A cutoff radius, r_c, lying between the first and second nearest neighbours has been used in the hopping integral such that only the nearest neighbour interaction is taken into account. So an atom may move out of or into the interaction range of another atom, merely by crossing r_c, without introducing an abrupt discontinuity in the forces.

A

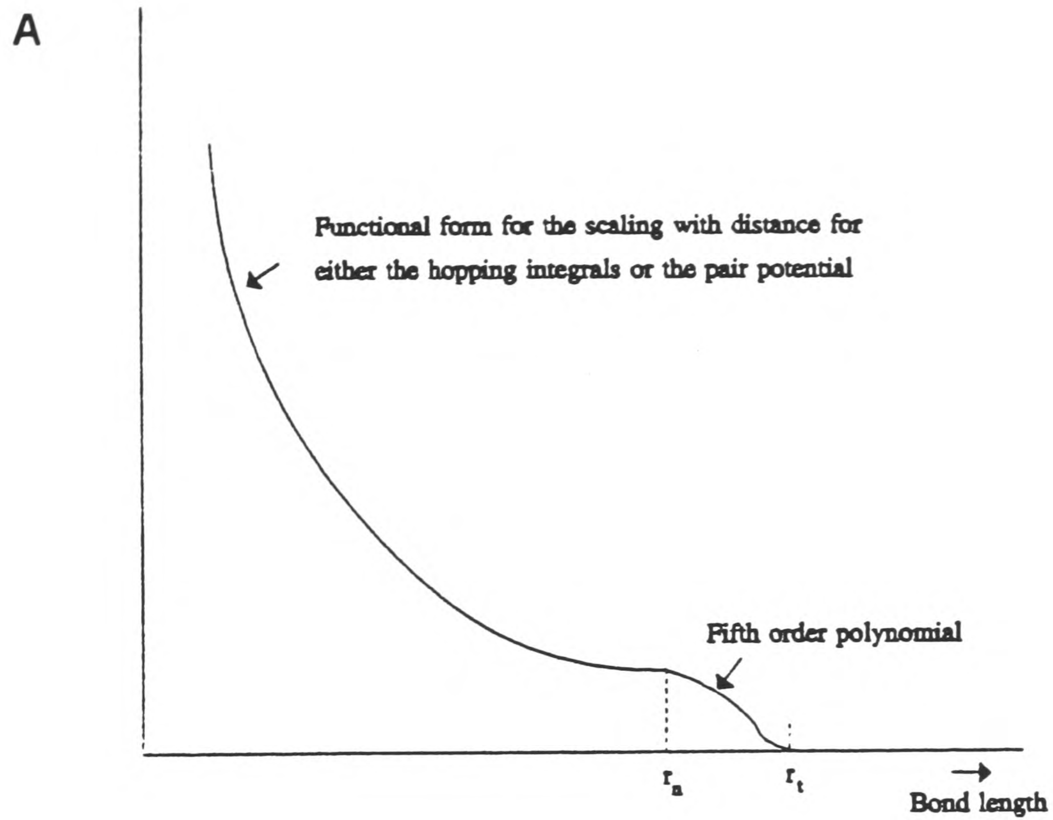

B

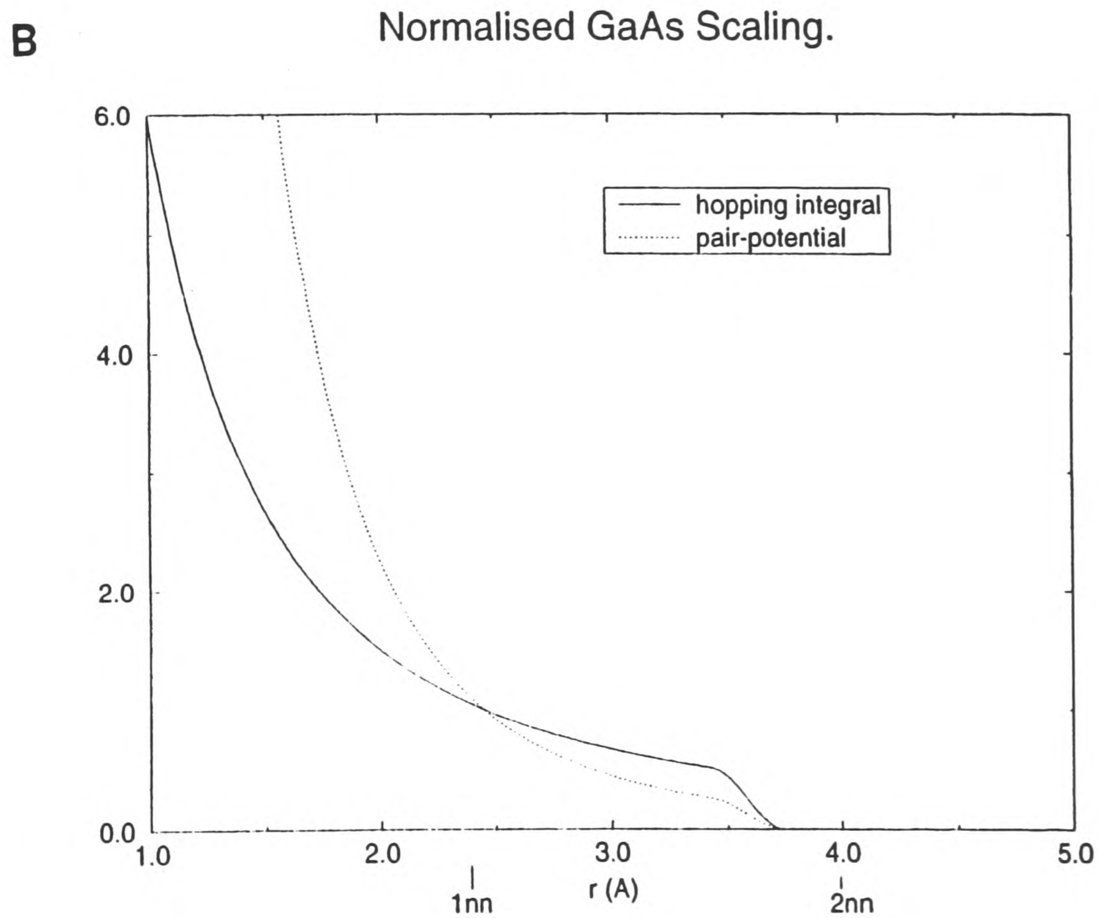

Figure 3.2: A) General form of the scaling law used in the tight binding scheme. Note the smooth termination to the scaling for the hopping integrals and the pair-potential within the tight binding scheme. Atoms can move in and out of r_t without introducing discontinuities in the force. B) Scaling law used for GaAs.

The **k**-space tight binding code used, based on Chadi's work (1979a, 1979b), was developed by McInnes (1992) and modified by Goringe (1994) to include the asymmetry in the sp interaction between Ga(s)-As(p) and Ga(p)-As(s). It is based on a periodically repeated supercell (periodic boundary conditions) for which the eigenvalues of the Hamiltonian are obtained in reciprocal space by matrix diagonalisation. Although the force (obtained as the derivative of the energy with respect to distance) and energy obtained are based on a finite basis, they are consistent with each other. The relaxation is carried out using molecular dynamics described briefly in the next section.

Sutton *et al.* (1988) broke down the total cohesive energy of a system into its physically transparent components in the tight binding bond model as follows:

$$E_{coh} = E_{cov} + E_{pro} + \Delta E_{es} + \Delta E_{xc} \tag{3.7}$$

where E_{cov} is just the sum of the covalent bond energies; E_{pro} is the energy of promoting an electron in a low lying atomic state into a higher atomic state to enable it to participate in bond formation; ΔE_{es} is the difference in the electrostatic and ΔE_{xc} in the exchange correlation energy between the solid and the isolated atoms. They also showed that the last two terms could be approximated to a sum of pair potentials.

3.3.2 Molecular Dynamics (MD)

A tight binding molecular dynamics scheme bridges the gap between first-principles and classical potential simulations. The main idea behind using MD is to obtain the global minimum energy configuration as opposed to a static local minimum obtained when MD is not used. In the static case, the energy and forces are calculated at 0^0 K for each iteration and the atoms are moved according to the forces acting on them. This process continues until either the forces become smaller than some value such as 0.01 eV/Å or the change in total energy between one iteration and the next is smaller than 0.0001 eV. The dependence on the initial configuration here is large, as the system has no energy

to jump out of a potential well, even if only a shallow well, and the existence of many shallow wells may be expected at defect sites. Starting a MD simulation involves setting a temperature and the corresponding energy is distributed in the system by giving each atom a random velocity from a Maxwell-Boltzmann distribution. In molecular dynamics the forces are calculated the same way, but atoms are now allowed to have kinetic energy as well. If the temperature is high enough the potential barriers can be jumped out of, and it is much more likely that one obtains the global minimum. However, there is no guarantee of that. The system evolves under Newtonian laws of motion as it is first annealed for about 10,000 time steps and then quenched (Finnis, 1990) to extract the lowest energy configuration. This is known as simulated annealing and quenching.

3.4 Bond Order Potentials (BOP)

Pettifor (1989, 1990) introduced the idea of a bond order potential which is a potential whose functional form is derived from the tight binding bond (TBB) model (Sutton *et al.*, 1988). It has the significant advantage over a **k**-space semi-empirical tight binding relaxation, in which the time taken is of the order N^3, in that the time involved here is proportional to N, where N is the number of orbitals in the supercell.

We have made use of the BOP for Si and GaAs in this thesis, but it has largely been used as a 'black box'. The code was written by Horsfield (1995). The bond order potential is based on the embedding of a bond in its environment, rather than an atom, and it can be expressed as an exact many atom expansion (Aoki and Pettifor, 1993). A study of its applicability to s and sp valent systems was carried out by Alinaghian *et al.* (1993) and it was shown that the model made good predictions, in particular the competition between graphite, diamond and simple cubic lattices is modelled well.

3.5 Summary

The most accurate method to study a system of atoms is to use density functional theory which is a fully quantum mechanical approach necessitating the evaluation of complicated integrals and hence limited to massively parallel computers for 1000 atoms. The semi-empirical tight binding method parameterises the complicated integrals and fits them to experimentally measured band structures. It can deal with many more atoms on conventional workstations. The bond order potential involves a slightly different view of the atomic system; the effect of the environment on a bond is studied as opposed to on an atom. This allows directional bonding to be described even at the lowest level of approximation, whereas no directional bonding is described by the simplest approximations to the local densities of states on atoms, such as in the Finnis-Sinclair (1984) potential. Tersoff's potential is also based on the idea of bond order although it is an empirical scheme not derived from quantum mechanics. It is remarkable that the Tersoff potential has the same type of functional form that the Bond Order Potential has in its simplest approximation. The results obtained from use of these theories are in Chapters 5 and 6 and the functional form as welll as the values for the parameters used in Tersoff, BOP and tight binding GaAs are tabulated in Appendix C.

Chapter 4

Low Angle Grain Boundary

4.1 Introduction

In Chapter 3 the theoretical approach and the computer programs used to analyze the images obtained were described. In this chapter the methodology of obtaining a correctly oriented grain boundary in a specimen with other essential features for good HREM imaging is set out and the result of one such successful imaging is shown. The conditions under which the image was obtained are given. A preliminary analysis of the low angle grain boundary is given, which leads to the ability to establish the atomic and electronic states associated with the boundary core. This detailed analysis is dealt with in the next chapter.

4.2 The specimen

4.2.1 Orientation

Dislocation lines and grain boundaries are often found to be parallel to $< 110 >$ in crystals with the diamond cubic structure, making the $<110>$ foil normal orientation the preferred orientation for high resolution imaging. In this orientation the core of the dislocation is parallel to the electron beam and a projected view of the core can be obtained edge on. Using the Back Reflection Laue technique (Laue, 1949) to determine

the orientation of the grains, a diamond saw was used to cut the GaAs ingot in the (110) plane. A plan-view TEM specimen was prepared with the foil normal close to the [110] ensuring that the lattice spacings of the planes to be imaged were greater than the resolution of the Jeol 4000EX microscope used at 400 kV for imaging. The [110] or $[\overline{1}\overline{1}0]$ direction was normal to one grain and the other grain was off by 0.7 degrees. This enabled the imaging to be done in both grains with sufficient clarity to allow quantitative analysis.

4.2.2 Preparation

High resolution electron microscopy requires the use of thin specimens because with a thick specimen resolution is degraded by effects of multiple elastic and inelastic scattering. From a GaAs ingot a plan-view specimen was prepared as follows. A 3 mm disc of $350\mu m$ thickness was cut ultrasonically, making sure that the grain boundary ran more or less along its diameter. The disc was then mechanically ground using first 600 grade and then 1200 grade SiC paper, to a thickness of $100\mu m$, followed by polishing using a diamond compound grit of $5\mu m$ and $1\mu m$ in turn. The specimen was then examined under an optical microscope to ensure that no scratches were visible on its surface after polishing. Using a Gatan Dimpler and diamond compound paste a dimple was made in the centre of the specimen till only $35\mu m$ remained as the thickness at the centre of the disc, the sides still being $100\mu m$ thick. The final stage in the thinning of the specimen was Ar-ion milling which was carried out for several hours at an angle of 15^0 at 4 kV and 0.5 mA gun current from each gun. Thinning was carried out from both sides and the specimen was rotated during thinning. In the last 2 hours the angle was reduced to 13 degrees so as to form a wedge shaped specimen with gradual increase in thickness, till a small hole at the centre of the specimen became visible. It is critical to stop the milling before the hole grows too large or the thin area of the

grain boundary may be lost entirely.

4.3 The imaging conditions

Unless otherwise stated, for all HREM imaging the Jeol 4000EX microscope was used at 400 kV. In order to determine the optimum conditions under which imaging of a suitable specimen is to be carried out it is important to know the aberration parameters of the microscope in use.

4.3.1 The Jeol 4000EX

At 400 kV the electron beam wavelength is 0.0164 Å. Due to the presence of chromatic aberration this value varies because of a small fluctuation in the high tension supply, and because the electron source size is finite. The chromatic half-width for the Jeol 4000EX is 80 Å for the single crystal LaB_6 source having an energy spread of 1-2 eV typically. The effect of chromatic aberration is worsened by thick specimens that have strong inelastic scattering. It is therefore important to make thin specimens and to take images from the thinnest regions by ensuring that the grain boundary of interest lies in this part of the specimen.

The spherical aberration present corresponds to a C_s value of 0.9 mm which is fixed by the lens design and it limits resolution. There is a side-entry goniometer that allows for a 20^0 tilt of the specimen. The zone axis at which the image is desired must therefore lie within this angular range of the specimen normal. To get the optimum image, passband imaging must be done (see Appendix B). Figures 4.1A-B show the contrast transfer function of the objective lens at two different defocal values. In Figure 4.1A, at an underfocus of -47.1 nm there is a well defined extended area of 'same contrast' and the contrast in the passband is high and positive, suggesting that atoms will be imaged white. However, the contrast in the experimental image also depends on the

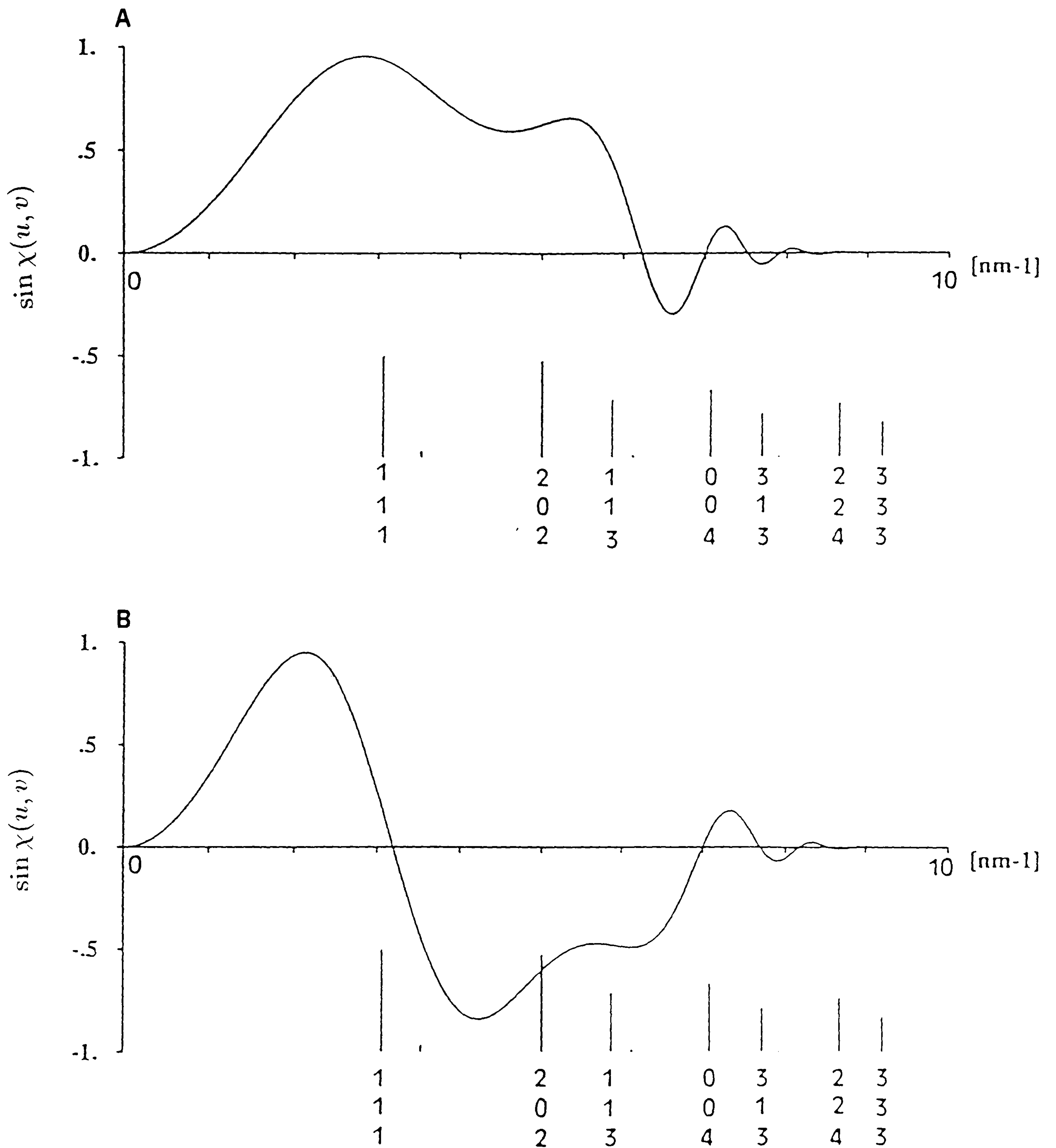

Figure 4.1: The contrast transfer function for the Jeol 4000EX at two different defocal values of a) -471 Å and b) -720 Å. Note the span of the plateau (i.e., region of same contrast) and the d-spacing of the GaAs planes shown at the base of both figures.

thickness of the specimen. The passband extends to 6.129 nm^{-1} which corresponds to a resolution of 0.163 nm. The lattice planes in GaAs that can be resolved are inserted at the bottom of the figure. This suggests that an objective aperture should be used to include the {111}, {002}, {202} and {113} diffracted beams only as they all have the same kind of contrast. The aperture diameters available are 26 nm^{-1}, 20 nm^{-1}, 12 nm^{-1} and 6 nm^{-1}. In Figure 4.1B the passband has shifted to larger values along the reciprocal spacing but the total extent of the passband is smaller. The defocus corresponding to the largest passband is the Scherzer defocus and the Scherzer resolution is given by the end point of the passband. They can be calculated using the following equations:

$$\text{Scherzer defocus} = 1.2[C_s\lambda]^{1/2}, \quad (4.1)$$

$$\text{Scherzer resolution} = 0.65 C_s^{1/4}\lambda^{3/4} \quad (4.2)$$

Using this we get the Scherzer defocus as an underfocus of 471 Å and a Scherzer resolution of 1.7 Å.

In the [110] zone diffraction pattern for the diamond cubic structure the indexed diffraction spots are given in Figure 4.2. The 12 nm^{-1} aperture was found suitable for imaging and it included 13 beams from a perfect area of one crystal. From a region containing a defect many more beams will be found in the same aperture.

4.3.2 Microscope Alignment

At 400 kV the filament was turned up to register a beam current of about 120±12% μA. With deflector condensers on, the beam was repeatedly centred and converged using the knobs beam *shift* and *brightness* till the smallest beam was obtained which converged concentrically when *brightness* was turned. A condenser aperture was inserted to obtain a nearly parallel and coherent beam. This procedure ensured that the electrons passed through the centre of the condenser aperture. Condenser lens

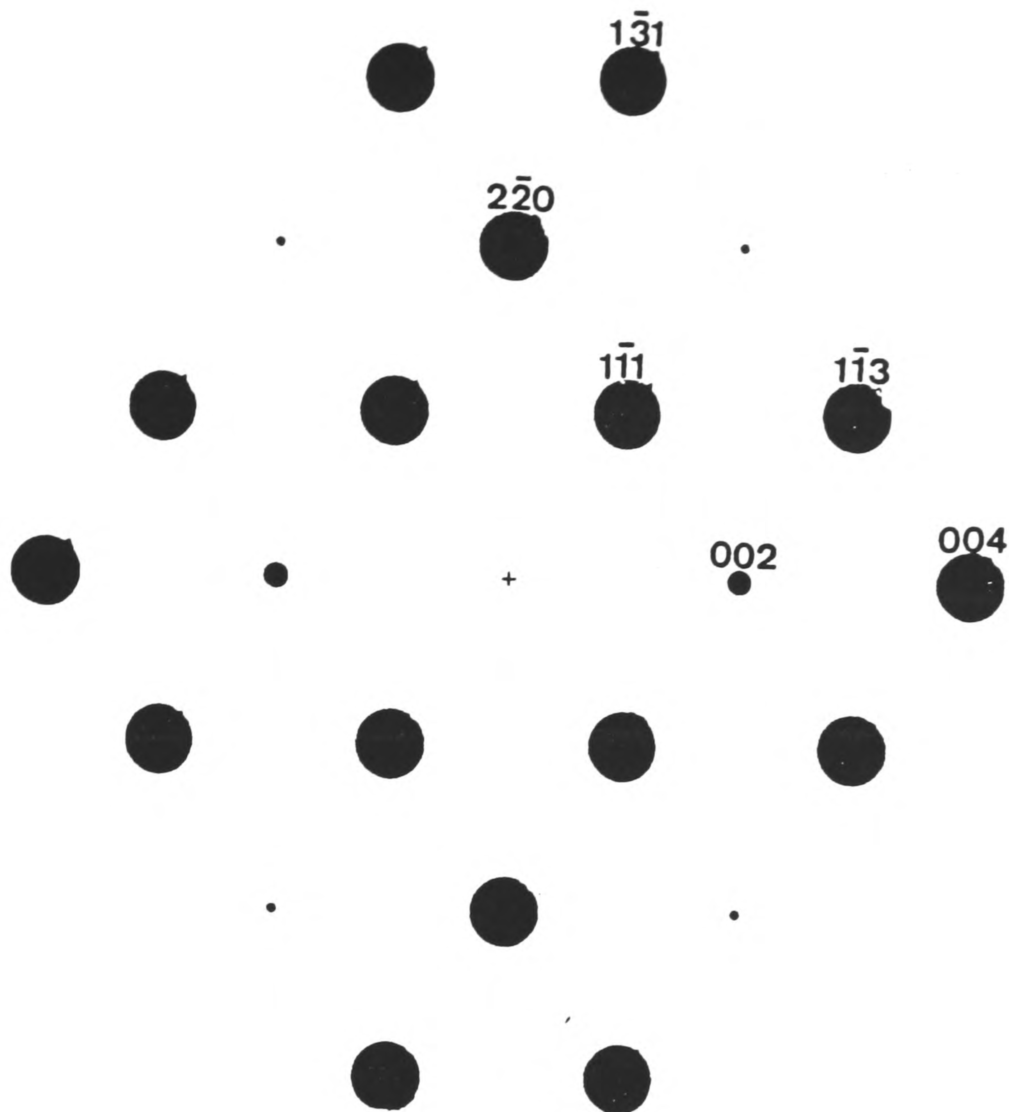

Figure 4.2: The [110] diffraction pattern for a diamond cubic structure with the indexing of some beams. Other spots can be indexed by symmetry.

astigmatism can lead to uneven irradiation on the specimen surface and insufficient brightness. This was corrected by use of condenser stigmators. Condenser alignment and beam shift adjustments were then carried out to minimise the amount of beam shift when the beam spot size is changed or when the beam is tilted. Care was also taken to ensure that the beam does not tilt when it is shifted. It is essential that the voltage centre is aligned, for if not, at high magnifications, images will be indistinct in a particular direction. A camera length of 2.0 m was chosen and the image shift with change in camera length minimised.

After having aligned the column it is now set for imaging the specimen. Searching out a grain boundary in the electron transparent area of the specimen requires careful inspection when the two grains differ in orientation by a few degrees only. This is because the change in the diffraction pattern across the boundary may go unnoticed by the eye. Resorting to a two-beam Bright Field or Dark Field condition helps find

the cracks and grain boundaries which can then be distinguished by going back to the diffraction mode. Figures 4.3A and 4.3B show a grain boundary in dark and bright field taken considerably off the [1,1,0] zone axis, when it was first found. The dislocations in the boundary plane are clearly visible in both these pictures. Also visible are the thickness fringes running parallel to the edge of the specimen formed due to the wedge shape of the specimen.

To image the boundary the specimen was tilted with the aid of Kikuchi lines visible in diffraction patterns from thicker regions of the specimen till the zone of the diffraction pattern was exactly [110] in one grain, the other being slightly off and the electron beam running along the optic axis of the column. The diffraction patterns are inserted in Figures 4.4. The selected area diffraction pattern from the grain boundary is also shown in Figure 4.4. A centred objective aperture was introduced so as to cut out the unwanted scattered beams to maximise the ease of interpretation, yet provide sufficient resolution. Interference between waves within the aperture gives rise to phase contrast, the phases being controlled by accurate focusing. Contrast in the image of a weak phase object is dependent on the objective aperture limitation, the spherical aberration of the objective lens and the defocus.

The magnification was increased to 800,000 times and an area near the grain boundary was carefully focused on while viewing through a pair of binoculars. Zero focus is approximately where the contrast in the amorphous region is a minimum. Astigmatism was removed by going through focus several times and checking for a non-directional change in contrast. If it is not removed the focal length changes with beam direction. When the best condition had been obtained the specimen shift was used to move on to the grain boundary region and a series of pictures was taken using Kodak SO163 film over a range of defocal values. The picture at Scherzer defocus has optimum contrast and resolution and is shown in Figure 4.4. It is discussed in the next section.

Figure 4.3: A) The dark field image of a grain boundary in GaAs, showing the presence of dislocations. B) The corresponding bright field image of the same grain boundary.

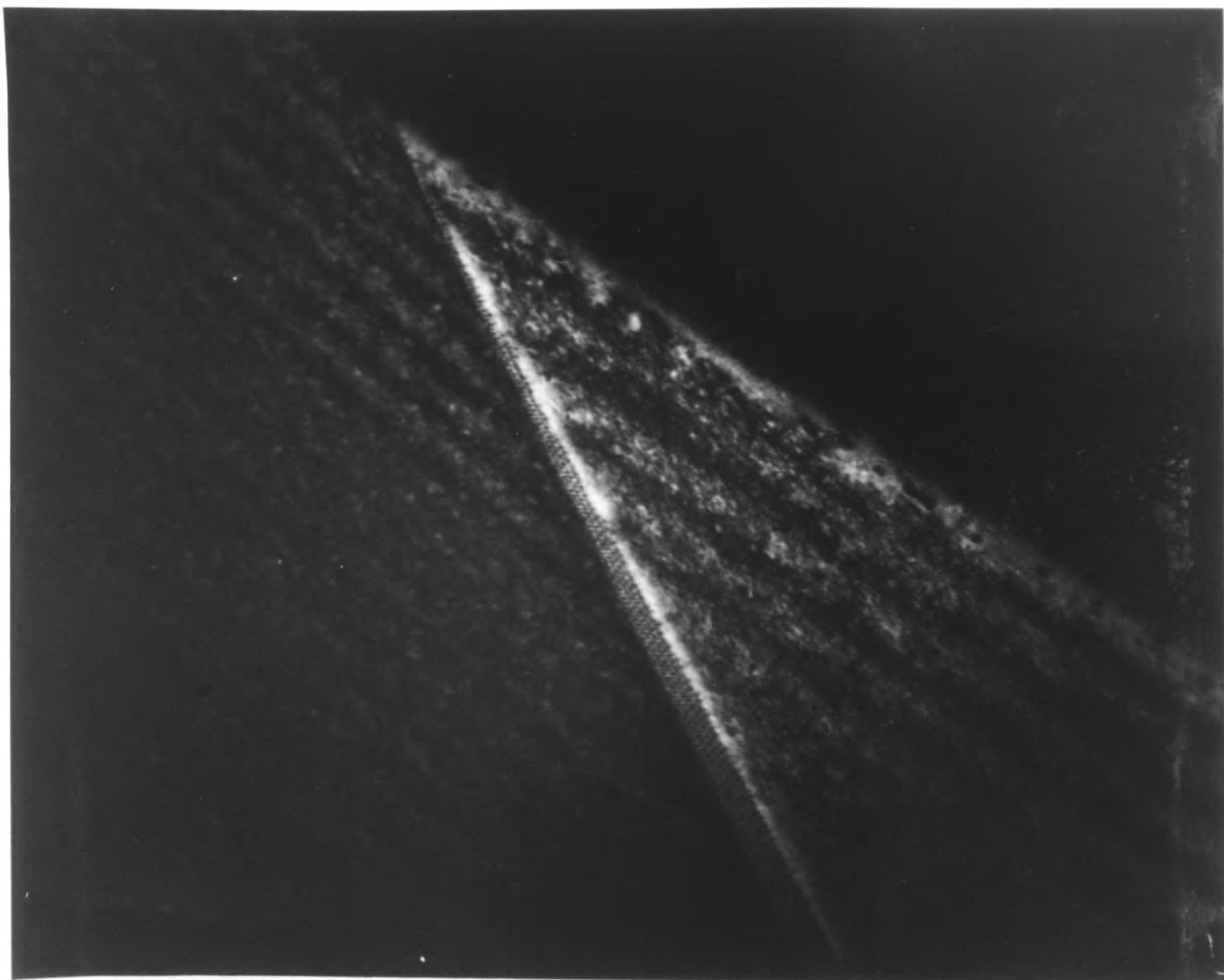
A

B

Figure 4.4: A photograph of the image of a 11.5^0 grain boundary about [110], recorded at Scherzer defocus along the [110] orientation. The diffraction patterns from grain A and grain B are inserted, as is the selected area diffraction pattern at the boundary.

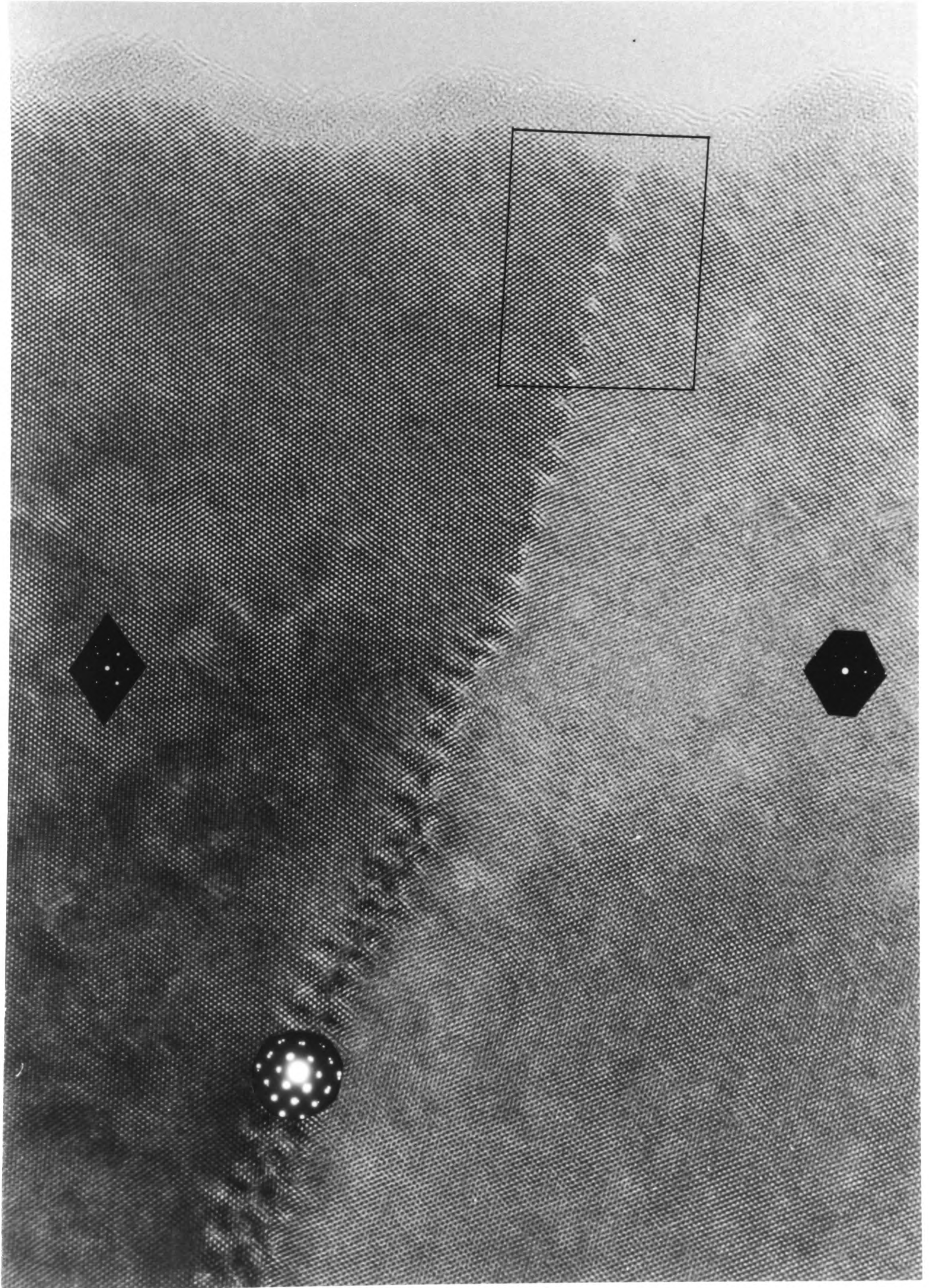

The setting up of ideal conditions at the microscope was not carried out at the region of interest as the contamination due to the beam during this time may be considerable and the specimen may buckle with beam heating. If beam damage does occur the ideal way to regain some good region is to Ar-ion mill the specimen at a low angle for a few seconds. While recording, the image specimen drift was checked for by ensuring the image of the hole was not blurred in any direction. Drift can arise from the improper securing of the specimen. All vibration in the vicinity of the microscope was minimised. With good alignment illumination was sufficient for the exposure time to be less than 2 seconds.

4.4 The Geometry of the Grain Boundary

Figure 4.4 shows the entire area of the grain boundary that was imaged. It is a picture taken at Scherzer defocus and it shows the boundary aligned as nearly edge-on as possible. A few interesting features may be noted in this image. Indications that the imaging conditions were correctly set up are found in the image of the amorphous edge at the hole. Its granularity reveals how well astigmatism has been minimised. Astigmatism is caused by the asymmetric magnetic field of the objective lens and a set of four crossed cylindrical lenses are present in the Jeol 4000EX with which to compensate the asymmetry of the field. As the thickness of the specimen increases the boundary looks less clear because the boundary plane is no longer edge on. The ideal conditions for imaging change with thickness. It is therefore clear that any analysis of the boundary should be carried out in the region of the image near the hole, the hole being identified by the amorphous edge imaged. The area in Figure 4.4 enclosed in a box has been enlarged for this purpose and is shown in Figure 4.5 with the hole towards the top of the page. On Figure 4.5 are marked some important directions in both grains taking the [1,1,0] direction of both grains to be common and along the

Figure 4.5: An enlargement of the boxed area in Figure 4.4. Some directions are marked on the grains. Some dislocations are marked out with arrows; others are left unmarked for clearer viewing.

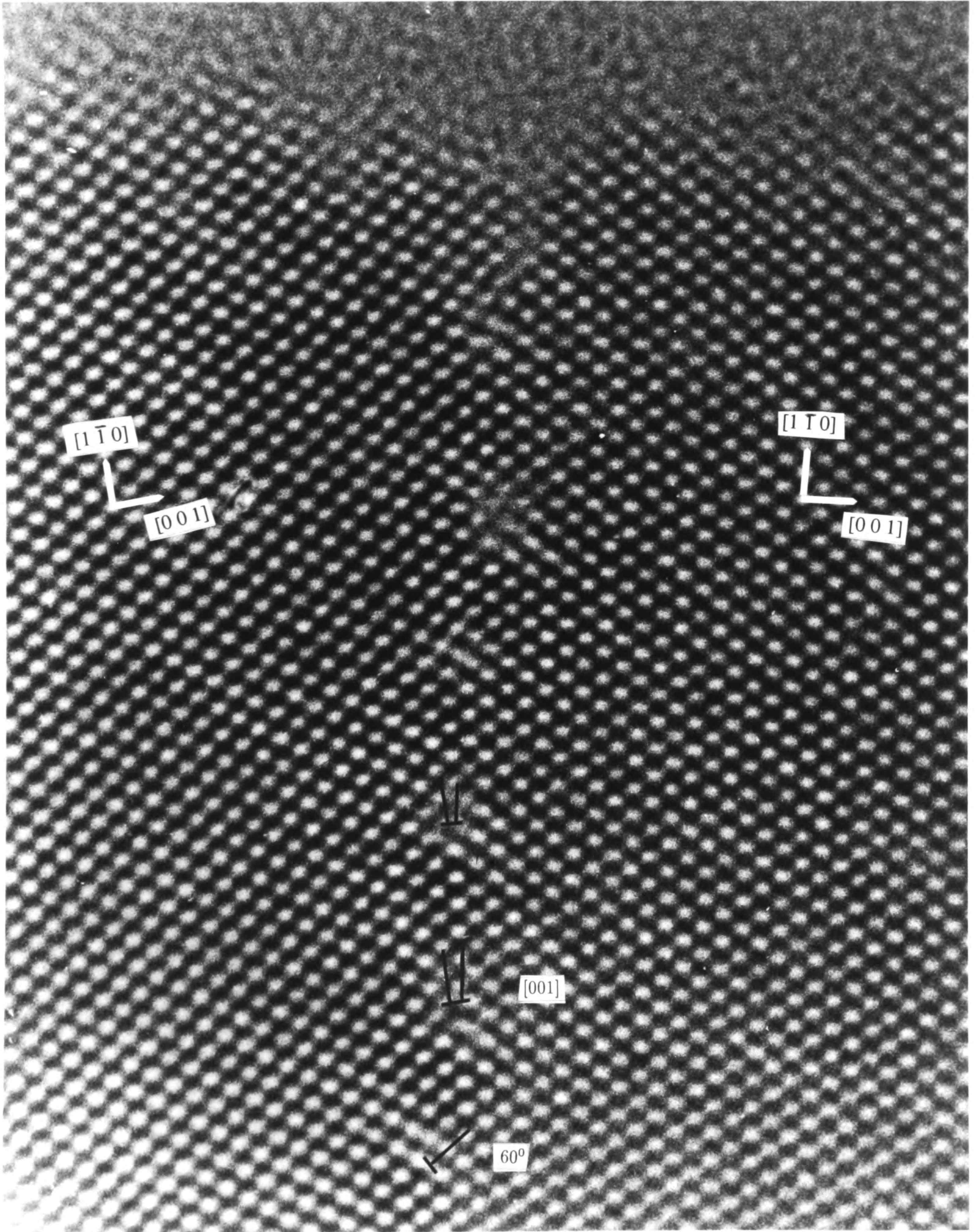

[1 $\bar{1}$ 0]
[0 0 1]
[1 $\bar{1}$ 0]
[0 0 1]
[001]
60°

upward drawn normal to the plane of the figure. It is clear from extending the [0,0,1] directions of both grains till they intersect that the misorientation angle of the grain boundary is 11.5^0, in agreement with that measured from the diffraction patterns, and that the $[0,0,1]$ direction in one grain is nearly perpendicular to the boundary itself. The misorientation is characterised by the axis being [1,1,0] and angle 11.5^0; and is closest to a $\Sigma 99$ Coincidence Site Lattice used in understanding the geometries of grain boundaries earlier.

In order to deal simultaneously with vectors in two grains it is convenient to define the coordinate system to be that of the median lattice (see Appendix A). The grain boundary is obtained by rotating by equal and opposite amounts about the rotation axis the boundary plane normals of the two grains by half the boundary angle. In this case this means a rotation by 5.75^0 about the common rotation axis, i.e. [1,1,0]. If the boundary were symmetric the boundary plane normals would be $[1,\bar{1},14]$ and $[\bar{1},1,14]$, each perpendicular to the rotation axis and making an angle of 11.54^0 between them. The mean boundary plane would be (001) which is a mirror plane as expected in a symmetric boundary. In fact, the boundary is not quite parallel to this symmetric inclination, being closer to (001) on one side.

Figure 4.5 focuses on how the incoherence at the boundary is taken up by dislocations. The dislocation cores are sufficiently far apart to be considered distinct. Using the RH/FS convention Burgers' circuits in the perfect lattice surrounding each core reveal essentially two types of Burgers' vectors, namely $\mathbf{a}[0,0,1]$ and $\mathbf{a}/4[1,\bar{1},2]$. At first these may seem unlikely, $\mathbf{a}$[0,0,1] being associated with too large an energy (energy is proportional to $|\mathbf{b}|^2$) to be found commonly, and $\mathbf{a}/6 <1,1,2>$ being the more expected Burgers vector in zincblende structure rather than $\mathbf{a}/4 <1,1,2>$. In Chapter 5 the $\mathbf{a}[0,0,1]$ dislocation is dealt with in depth.

The $\mathbf{a}/4[1,\bar{1},2]$ dislocation may be understood by considering the presence of a

$\mathbf{a}/4[1,1,0]$ screw component in addition to it to give a resultant $\mathbf{a}/2[101]$ Burgers vector. The $\mathbf{a}/4[1,1,0]$ component cannot be imaged in the orientation of the specimen used in this experiment. $\mathbf{a}/2[101]$ is a lattice translation vector for the diamond cubic structure, and a dislocation of this Burgers vector is perfect and hence expected to occur. The dislocation may be thought of as :

$$\mathbf{b} = \mathbf{a}/4[1,\bar{1},2] + \mathbf{a}/4[1,1,0] = \mathbf{a}/2[101] \tag{4.3}$$

or,

$$\mathbf{b} = \mathbf{a}/4[\bar{1},1,2] + \mathbf{a}/4[\bar{1},\bar{1},0] = \mathbf{a}/2[\bar{1},0,1] \tag{4.4}$$

4.5 Geometric Construction of the [001] Edge Dislocation

The atomic structure to be fed into the simulation program was generated geometrically and then relaxed using classical and semi-empirical potentials. The relaxation will be dealt with in the next chapter. In this section we deal with the geometric aspects of the construction of the supercell. Great care must be taken in constructing the supercell and the construction is not trivial.

Two supercells are constructed, both containing dislocation dipoles of Burgers vector [001], one with 446 atoms and another with 336 atoms. The smaller supercell is an approximation to the larger and the justification for the approximation is that after relaxation, the dislocation core structure is very nearly the same in both. The need for a smaller supercell arises from the memory size required by the relaxation programs that are semi-empirical.

Programs developed by Bigger (1992) were used for constructing the geometry, namely **GEN3D** and **AESOL**.

4.5.1 The 446 Atom Supercell

GEN3D was used to construct a 3 dimensional perfect crystal slab in a diamond cubic lattice. The axes of the slab are chosen to be along $[1,\bar{1},14]$, $[\bar{7},7,1]$ and $[1,1,0]$ in keeping with the discussion in Section 4.4. We now wish to introduce two grain boundaries of 11.5^0 about [110] in this slab. In order to preserve translational symmetry on the introduction of a defect, and so the applicability of Bloch's theorem, a supercell as suggested by Marklund (1978) was developed. Although the periodic repetition of cells in all directions was used to eliminate the surface effects it leads to problems of its own. It is not always easy to establish perfect matching at the supercell edges and several ways round the problem have been tried (Marklund, 1979, 1983; Wang and Teichler, 1989, Bigger *et al.*, 1993). In this slab two equal and opposite [001] dislocations were then introduced using **AESOL** in such a fashion as to construct two equivalent [001] cores. This program uses anisotropic elasticity to introduce the displacement field of periodic arrays of dislocations. In the computational cell there is one dislocation dipole. Since periodic boundary conditions are applied to the computational cell in the relaxation program, periodic arrays of dislocations are generated by the boundary conditions on the computational cell. It is therefore essential to introduce the elastic displacement field of these periodic arrays of dislocations, and this is done in **AESOL**. The periodic arrays of dislocations generate tilt grain boundaries of alternating sign. The separation between the dislocations in a tilt boundary is determined by the supercell height, which was adjusted to correspond to the misorientation angle of 11.5^0 found in the experimental image.

Bigger (1992) showed the importance of the supercell height (in this case along $[\bar{7},7,1]$) being commensurate with the periodicity of the grain boundary generated in order to avoid a horizontal shear strain at the edges of the supercell. It is appropriate at this point to check whether the supercell used here is commensurate with the

boundaries generated.

Figure 4.6A shows a [110] projection of a perfect diamond cubic lattice in which we imagine a grain boundary along AC. Consider a lattice site, A, and travel along $[\overline{7},7,1]$ one period of the boundary to C. Now, in this distance the displacement in either grain would be $|\mathbf{b}|/2$, where $\mathbf{b}$ is the net Burgers vector per period of the boundary, which is shown by AB and AD. Then, since C lies on a lattice site we are certain that the periodicity of the boundary is satisfied so long as there are 2[001] dislocations in one $[\overline{7},7,1]$ period. Also, refering to Figure 4.6B and using Frank's formula:

$$\mathbf{b} = 2d \sin \theta/2 \tag{4.5}$$

and using $\theta = 11.5^0$ and $d = [\overline{7},7,1]$, or 9.949**a**, we get $\mathbf{b} = 2[001]$. This means that the smallest supercell must contain a total of four [001] dislocations, as can be seen in Figure 4.7 which shows the 446-atom supercell.

4.6 The 336 Atom Supercell

GEN3D was used to generate a 3 dimensional periodic orthogonal slab of 336 atoms in a diamond cubic lattice, the slab having its axes along the $[001], [1\overline{1}0]$ and $[110]$ directions respectively. Again, **AESOL** was used, but to introduce only a single dislocation dipole of [001]**a** as can be seen in Figure 5.4. This means we now have a boundary of misorientation 5.79^0 about the [110] rotation axis. Also, there is a shear strain at the block edges due to the mismatch in the boundary period and the supercell height. There is a danger in relaxation using periodic boundary conditions that errors in matching atoms at the boundary might be absorbed into the relaxed structure. The strain is small enough to leave the core structure similar to that obtained for the 446 atom block as can be seen from the comparison made in Table 4.1 of the bond distortions in both the cores obtained from relaxations with the Tersoff potential. The dangling bonds at the geometric dislocation core were seen to reconstruct

Figure 4.6: A) An illustration of the desired supercell dimensions for modelling the [001] dislocation. Consider a lattice site, A, and travel along $[\overline{7},7,1]$ one period of the boundary to C. Now, in this distance the displacement in either grain would be $|\mathbf{b}|/2$, where **b** is the net Burgers vector per period of the boundary, which is shown by AB and AD. Then, since C lies on a lattice site we are certain that the periodicity of the boundary is satisfied so long as there are 2[001] dislocations in one $[\overline{7},7,1]$ period. B) A schematic diagram illustrating the required supercell height to match the grain boundary periodicity. (After Bigger, 1993).

A

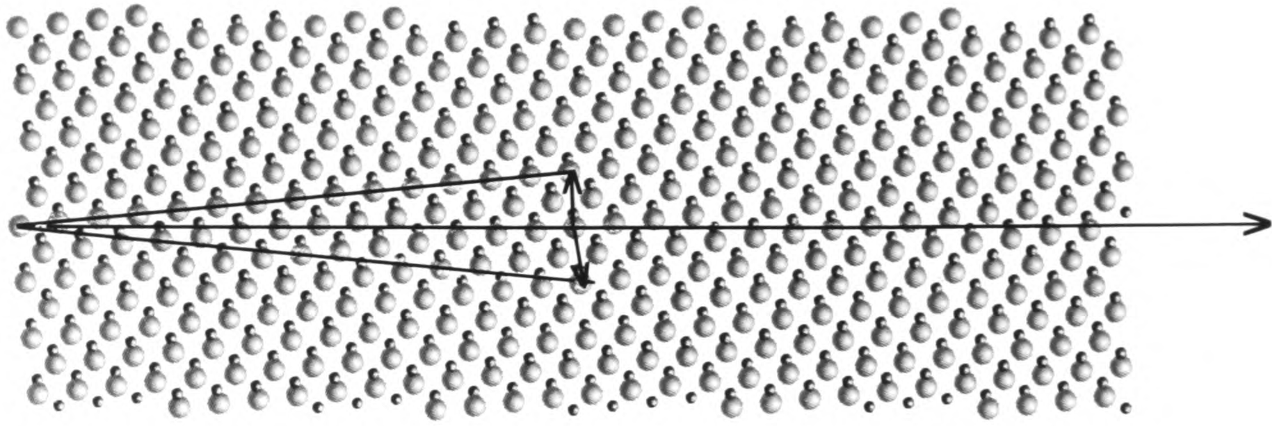

B

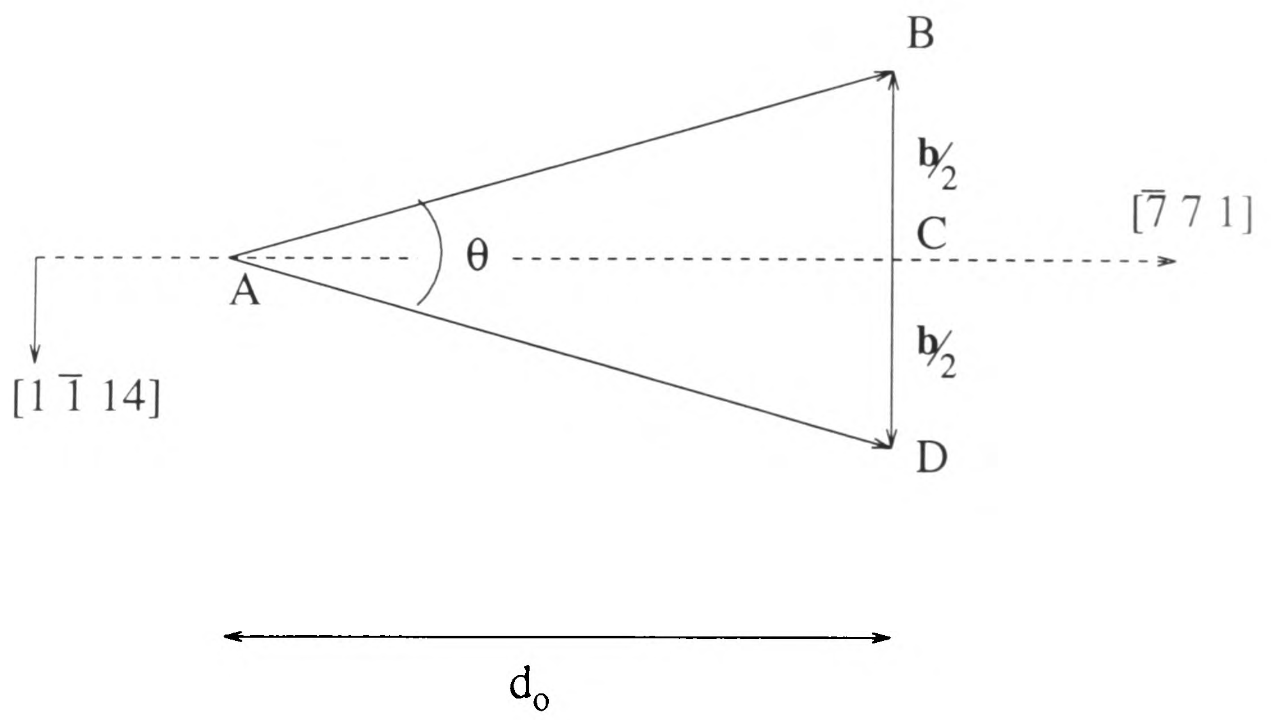

Figure 4.7: A [110] projection of the 446-atom supercell containing two [001] dislocation dipoles per boundary period. The As atoms have been shown larger than Ga in order to distinguish the two.

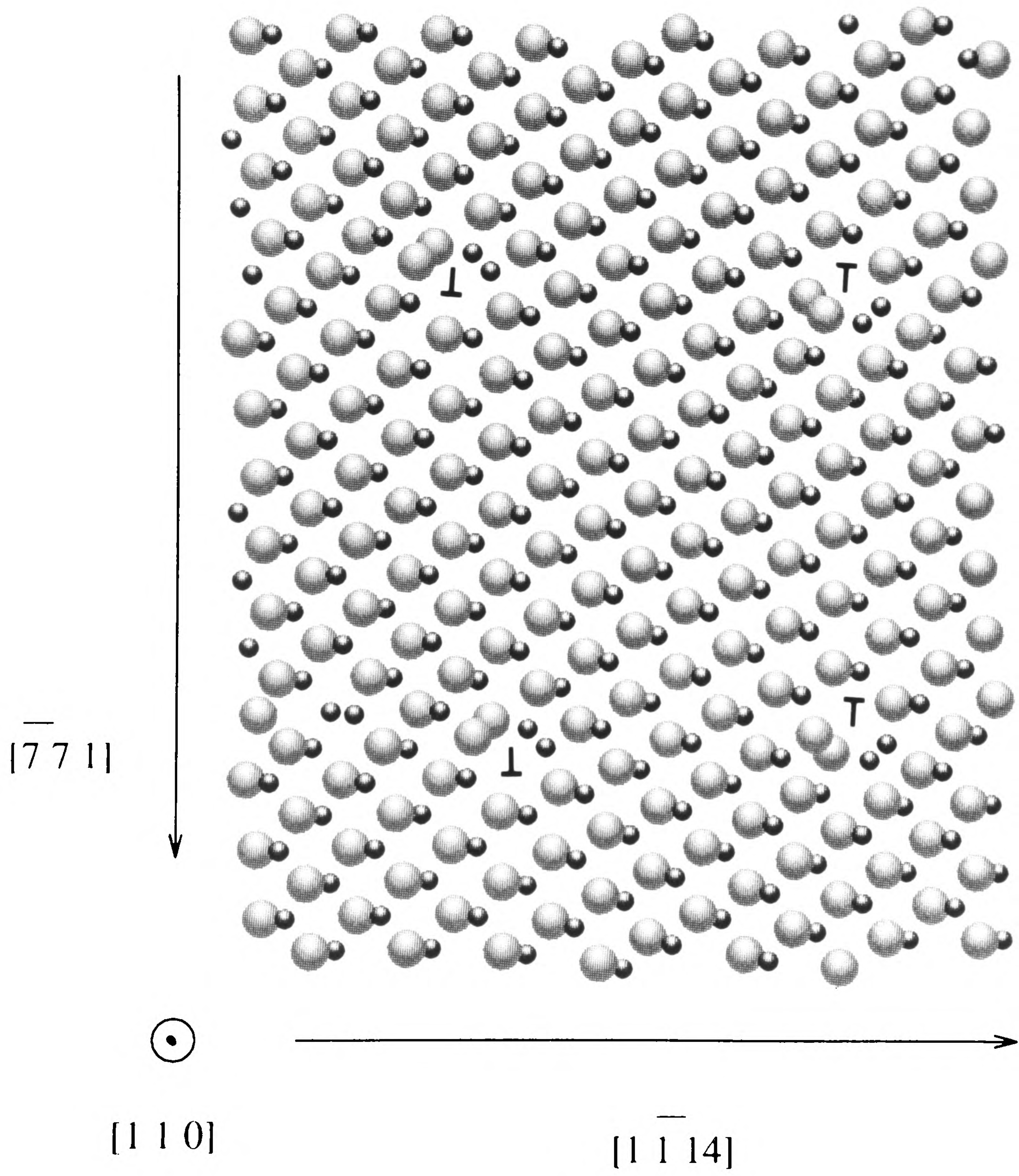

[$\bar{7}$ 7 1]
[1 1 0]
[1 $\bar{1}$ 14]

Bond Index	446 Block	336 Block	Difference
1	2.405	2.394	0.01 %
2	2.238	2.188	0.05 %
3	2.389	2.362	0.03 %
4	2.682	2.736	0.05 %
5	2.498	2.471	0.02 %
6	2.427	2.422	0.01 %
7	2.422	2.595	0.07 %
8	2.373	2.362	0.01 %
9	2.754	2.838	0.08 %
10	2.318	2.286	0.03 %
11	2.322	2.280	0.04 %
12	2.358	2.286	0.07 %
13	2.384	2.481	0.09 %
14	2.290	2.220	0.07 %
15	2.300	2.305	0.01 %
16	2.505	2.541	0.04 %

Table 4.1: Box size effects on bond distortions in relaxed [001] dislocation cores in silicon.

into tetrahedral coordination upon relaxation. Both classical and tight-binding relaxations revealed that such a reconstruction of the bonds along the dislocation line was favoured. In the case of the 90^0 partial in Si it has been shown (Bigger, 1992) that the reconstruction of dangling bonds in the core gives rise to an asymmetric structure with all atoms tetracoordinated and is preferred to a symmetric core with quasi-five-fold reconstruction.

Chapter 5

The [001] edge dislocation

5.1 Introduction

This chapter deals with the interpretation of the image of the [001] edge dislocation shown in the previous chapter and the calculation of the electronic structure associated with it. This dislocation has been seen earlier by Krakow and Smith (1987) but to the best of my knowledge the dislocation core structure has never been analyzed before. This is therefore the first atomic and electronic structure to be proposed for the [001] edge dislocation in GaAs. It is found here to closely resemble the 90^0 partial in Si and the two are compared.

In order to interpret the experimental image in terms of a well defined atomic structure it is essential to simulate the image using assumed structural models and to compare the simulations with the image taken on the high resolution electron microscope. Only when the two are considered to be in good agreement is the atomic structure of the defect fully determined, and an electronic structure calculation can then be performed. In this chapter, therefore, first the simulation is carried out to determine a reasonable atomic structure of the [001] dislocation, which is then compared quantitatively with the experimental image, and then the information about any localised electronic states associated with it is extracted.

5.2 HREM Image Simulation

The interpretation of an image, i.e., the determination of the atomic positions, involves a process of trial and error. An atomic model of the defect is introduced in a computer, then the wave-function resulting from the interaction between the incident electrons and the crystal containing the defect is calculated. The effect of aberrations on the phase and amplitude of the waves is considered and the final intensity distribution calculated. The computed image is then compared to the micrograph recorded under the same imaging conditions.

There are several image simulation packages available for the use of image matching. The aim of such a package is to calculate images for different specimens as they should be observed in the HREM under specific imaging conditions and known microscope parameters. Use was made of the EMS package developed by Stadelmann (Stadelmann, 1987) for all simulation work and it was run on the Oxford University VAX and in the Materials Modelling Laboratory (MML). An innovative procedure of automatic refinement by off-line digital image processing developed at the Max Planck Institüt für Metallforschung, Stuttgart, Germany was used, during a three month visit there, to try to refine the atomic structure. This procedure is based on quantitative comparisons between experimental and simulated HRTEM images.

The structure refinement procedure, including image simulations, was programmed to run automatically on a computer (DEC Station 5000) in Stuttgart.

In order to determine the structure underlying a HRTEM image an assumption of uniqueness has to be made. This implies that two identical images can originate only from two identical structures, and that the images of two similar structures become increasingly different with increasing differences between the structures.

The procedure of structure determination based on these assumptions is divided into the following steps:

- Digitisation and processing of experimental negatives.

  A first step to making quantitative comparisons between the two images was to digitize the experimental image. This was done in Stuttgart using a diode-array camera (EIKONIX) with a dynamic range of 2. The signal of the densitometer is proportional to the translucence of the negative. The random noise in the image can be reduced by filtering at this stage, but for our image the noise was minimal.

- Possessing a starting structural model.

  This was obtained from the atomic relaxations carried out in Section 5.3. The supercell was used for generating simulated structures using EMS as described in the next section. The simulated image was then cut so as to contain only one dislocation core and the area of interest surrounding it.

- Quantitative definition of image discrepancy.

  In order to obtain the best fit to the experimental image, certain pre-selected atoms are allowed to shift so that better image matching occurs. This leads to a structure that may be considered the 'experimental-best-fit' structure as opposed to the relaxed structure obtained by energy minimisation based on some description of atomic interactions. It is necessary to define the discrepancy of the two images - the simulated and the experimental. There are several suggestions for calculating this, such as the R-factor (Smith and Eyring, 1982), the cross-correlation function (Frank, 1980) or a scalar product (Ourmazd, 1989).

- Iterative structure refinement.

  The process of image simulation, quantitative image comparison, and the modification to the structure is iterated in order to optimise the match between the image simulation and the experimental image. The refinement stops when the

discrepancy between the two images converges to a minimum, and the atomic displacement between the two iterations becomes less than 0.03 Å.

5.2.1 The EMS Program

Either the program can be used to generate a perfect crystal structure of specified symmetry or a supercell containing the defect of interest must be input into the program. The basic image forming mechanism in an electron microscope is a two stage process: an electron wavefunction resulting from a dynamical scattering process is formed at the exit surface of the specimen and is then modified by the objective lens contrast transfer function. The final intensity distribution on the film is a convolution of these two processes.

The EMS package offers a variety of programs which are referred to by three characters printed in bold throughout this text. The program takes into account the specimen thickness and orientation, the spherical aberration, defocus, objective aperture, beam divergence and energy spread of the incident beam. In addition to these the crystal structure needs to be fed into the program. This is simple when a perfect crystal is being considered but in the case of defects the structure must be guessed beforehand. How to guess a structure is discussed in Section 5.3, but for the present the atomic structure of the defect is assumed to be known. In these calculations no account of absorption was taken for a specimen thickness less than 200 Å. Neglecting absorption within such a thickness has been the norm for most of the simulations of GaAs reported in literature. The main reason for neglecting the absorption lies in the difficulty faced in trying to estimate it.

The interaction of the electrons with the supercell is strong and requires a dynamical approach. This can be calculated in two ways. One way is to solve the Schrodinger equation using a superposition of plane waves (Howie and Whelan, 1961). Another

method is an optical description of the propagation of electrons through a crystal cut into infinitesimally thin slices, called the multi-slice approach (Cowley, 1975).

EMS is a software package for electron diffraction analysis and HREM image simulation based on the Fast-Fourier-Transform multi-slice approach for perfect crystal structures and on the Bloch wave formalism for defect structures. The specimen is cut into thin slices in which the phase grating approximation is valid. The phase grating approximation is to consider only low angle diffraction and assume a slow variation of the potential along the propagation direction of the electrons. The **pg2** or **sc3** operation can be used to generate a phase grating and Fresnel propagator functions which are used by the multi-slice iterations. The projected potential can also be obtained by this operation. The **ms1** is a multi-slice iteration operation that works by Fast Fourier Transform to create the wavefunctions at the exit surface, which are then used to calculate the HREM images by allowing them to interfere. The amplitude and phases of selected diffracted beams as a function of specimen thickness can also be obtained at this stage. The operation **im1** was used to form the image based on what Stadelmann refers to as the 'non-linear' formation theory which, for example, allows interference between {111} and {113} reflections as opposed to 'linear' images which allow each reflection to interfere with the (000) beam alone. Due to this, greater complexity and realism in the 'non-linear' images is expected. The terms 'linear' and 'non-linear' used here are not to be confused with those used to describe mathematical equations.

5.2.2 Simulation of perfect crystal images

Multi-slice calculations in the [110] direction sampled with a 128 $\times$ 128 mesh were performed for the non-centrosymmetric unit cell shown in Figure 2.1 over a range of crystal thickness 0-200 Å. The images obtained at different defoci and different thicknesses are given in Figure 5.1 (A & B), and the projected potential is inserted into the bottom

Zone axis	[110]
Specimen structure	GaAs
Lattice Parameter	5.649 Å
Accelerating Voltage	400 kV
Objective Aperture Diameter	12 nm^{-1}
C_s	0.9 mm
Spread of Focus	8.0 nm
Beam Divergence	0.5 mradians
Absorption	nil
Defocus	varied between 0 and -480 Å
Scherzer Defocus	-471 Å
Specimen thickness	varied between 0 and 200 Å
Image dimensions	512 × 512

Table 5.1: Parameters used to simulate the perfect crystal images with the EMS package.

left of the image 5.1A. Table 5.1 gives the values of the remaining parameters specific to the imaging conditions used. Although the objective aperture includes 13 beams the dumb-bell shape expected for atomic pairs just being resolved is missing from the experimental image. This may be due to the axial electron beam not being completely coherent. From Figure 5.1A it is clear that the images are periodic with thickness and with defocus. For example, in the lowest row shown the contrast reverses from **c** to **d**, showing periodicity with defocus. Careful matching with the perfect crystal region imaged is obtained by trial and error. Figure 5.2 is the digitized experimental image on which three boxes A, B and C have been drawn to mark out regions used to qualitatively compare with appropriate simulated images. A superposition of the box in Transparency A (contained in the envelope attached to the back cover of the thesis) on Box A in Figure 5.2 gives a qualitative idea of matching the simulation to the digitised image. Figure 5.3 shows the difference between the two images by the pattern given by the simulation being subtracted from the experimental image. This box corresponds to 136 Å thickness and -480 Å defocus and the atomic columns are imaged black while

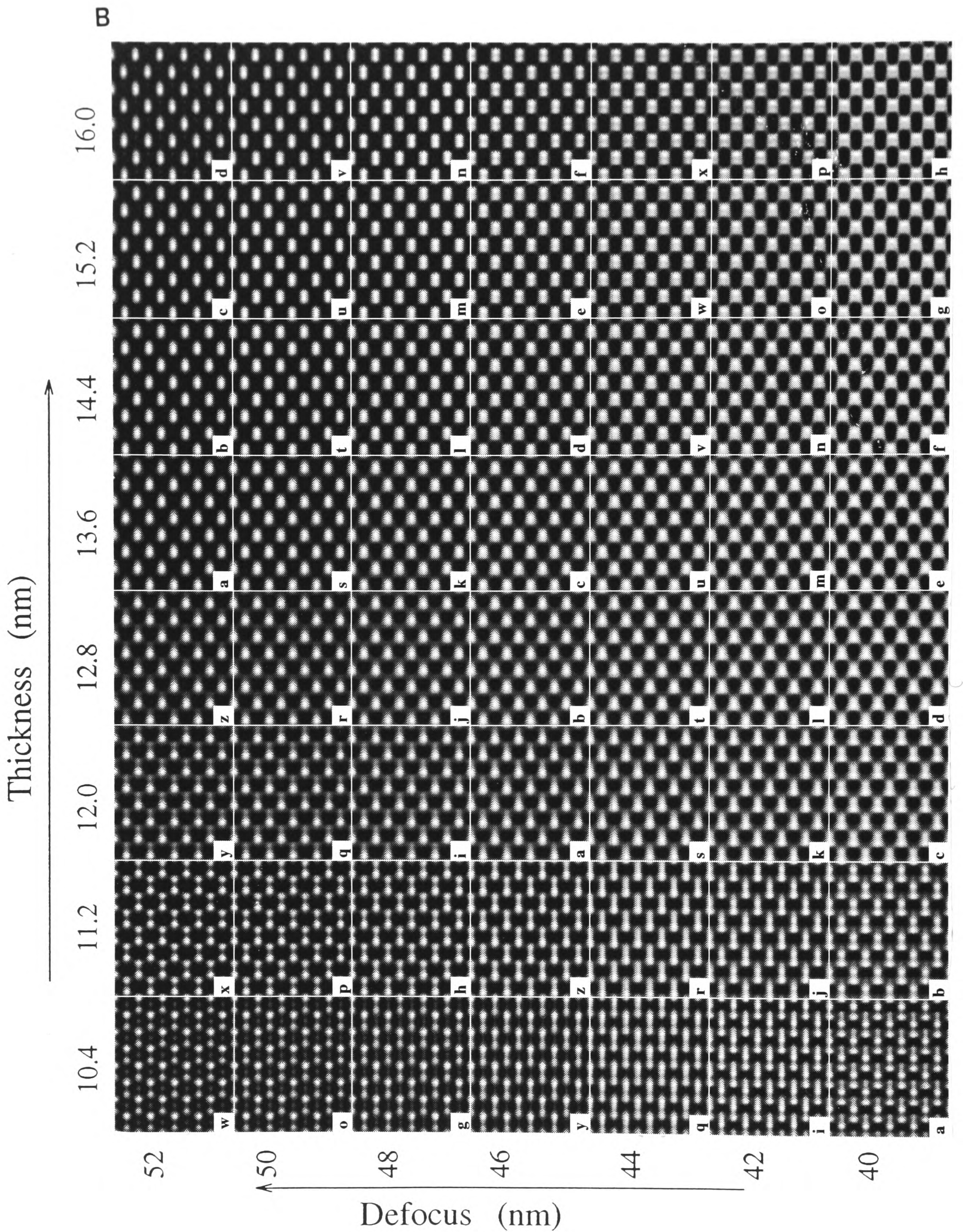

Figure 5.1: Simulated images of the perfect GaAs lattice at varying thickness and defocus. These images were obtained by the EMS package (Stadelmann, 1987), using the parameters given in Table 5.1. A) A coarse thickness-defocus variation. Also shown is the projected potential inserted at the bottom left of the figure. Image 'l' was chosen for image matching. B) Small variations around the image at 13.6 nm thickness and Scherzer defocus.

A

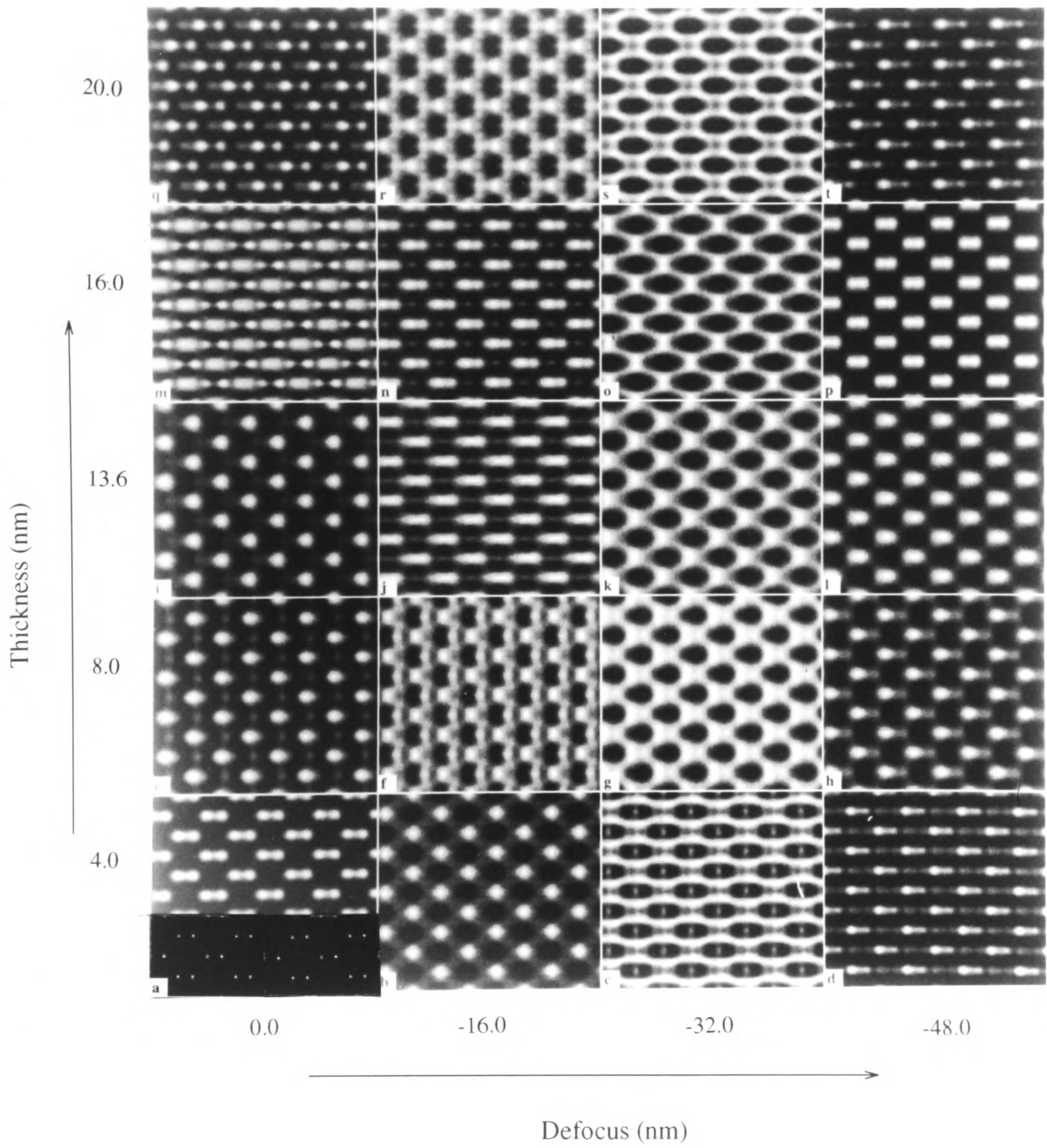

Figure 5.2: The digitised image of the grain boundary. Boxes A, B and C are drawn in to facilitate superposition of simulated images contained in the envelope attached to the back cover of the thesis, on the perfect crystal region, the [001], and the 60^0 dislocations.

C
B
A

Figure 5.3: The difference image obtained from the comparison of the simulated image '1' and the perfect crystal region in one grain of Figure 4.5.

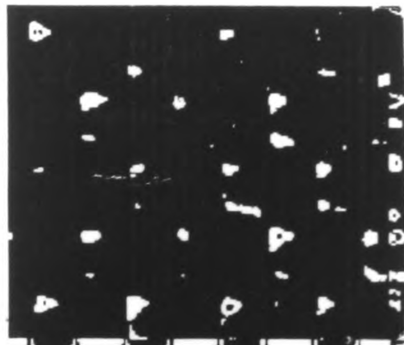
A

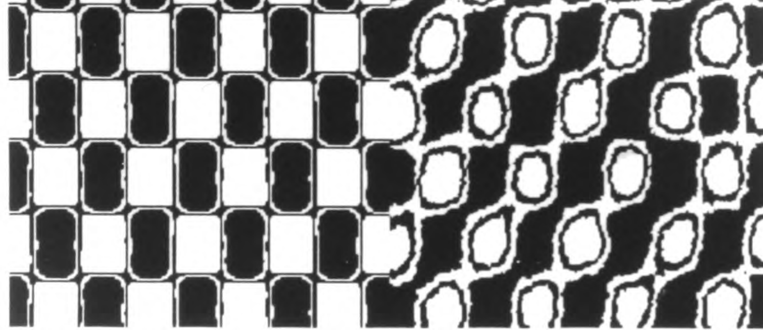
B
C

the tunnels are imaged white. This confirms the fact that the image shown in Figure 4.5 was taken nearly at Scherzer defocus which is at 471 Å. Note from Figure 5.1B that there is a range of thickness (12.8 - 14.4 nm) and defocal values (44 - 50 nm) that present similar images. The image at 'k' in 5.1B was choosen as the size and shape of the white region appeared best matched to that of the experimental image shown in Figure 4.5. Also, the contrast variation was judged to be the most appropriate amongst the range of similar images. It remains to be checked that a simulated image of the [001] dislocation at this defocus is well matched to its experimental image for a reasonable thickness.

5.2.3 Simulation of [001] edge dislocation

The atomic structure required for the dislocation image to be simulated was obtained by relaxation of a supercell containing two dislocations of equal and opposite Burgers vectors. The supercell used and how it was obtained is detailed in Section 5.3. A projection of the supercell is shown in Figure 5.4 where the red spots are As atoms and the yellow Ga. Figure 5.5A shows the projected potential and the images calculated at different thickness and defocii are shown in Figure 5.5B. The images appear complex and less clear with increasing thickness of the specimen, for each thickness the most directly interpretable image being at Scherzer defocus. There is black atom contrast at Scherzer defocus for thicknesses 160 Å and 200 Å and a reversed contrast at 80 Å and 120 Å.

Note that in the experimental image labelled Figure 4.5 the atoms are imaged black and the tunnels are imaged white. Therefore in the corresponding simulation we expect to see white tunnels in the calculated image. Since the defocus used in the experiment was estimated to be near Scherzer, in Figure 5.5B therefore we find the image 'l' to be closest to our true imaging condition. It corresponds to a thickness of 160 Å and

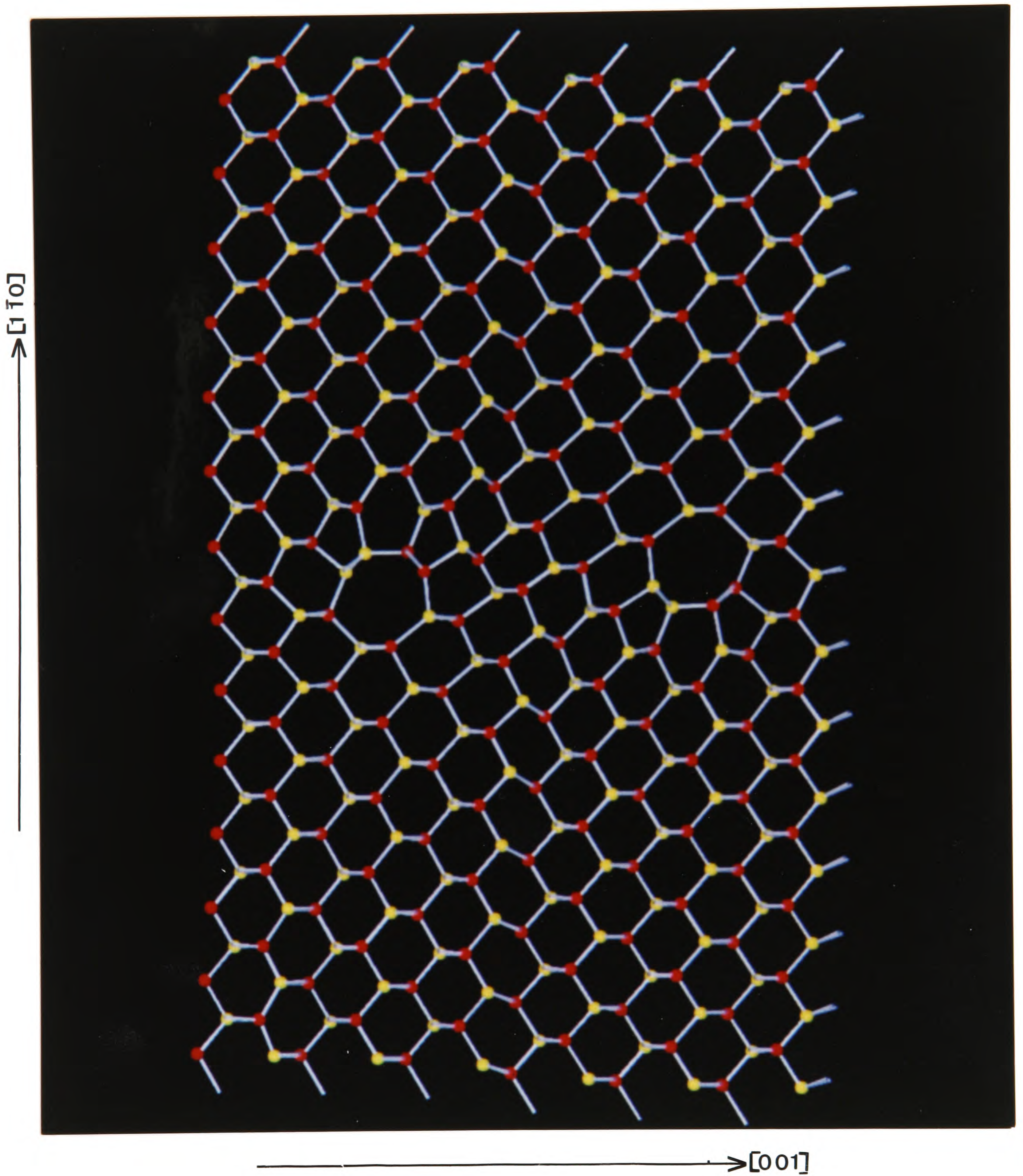

Figure 5.4: The [110] projection of the 336-atom supercell containing a [001] dislocation dipole. This supercell has been relaxed using Chadi parameters for GaAs with a k-space tight binding code.

Figure 5.5: A) The projected potential for the tight binding relaxed 336-atom supercell, under conditions given in Table 5.1. B) A thickness-defocal series of simulated images for the [001] dislocation, obtained from the tight binding relaxed 336-atom supercell. The defocus varies along a row from left to right in nm, and thickness increases along a column.

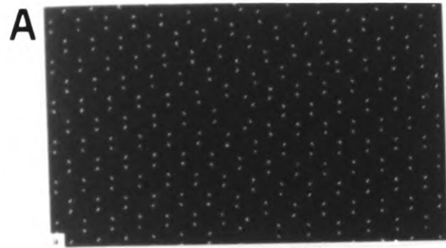
A

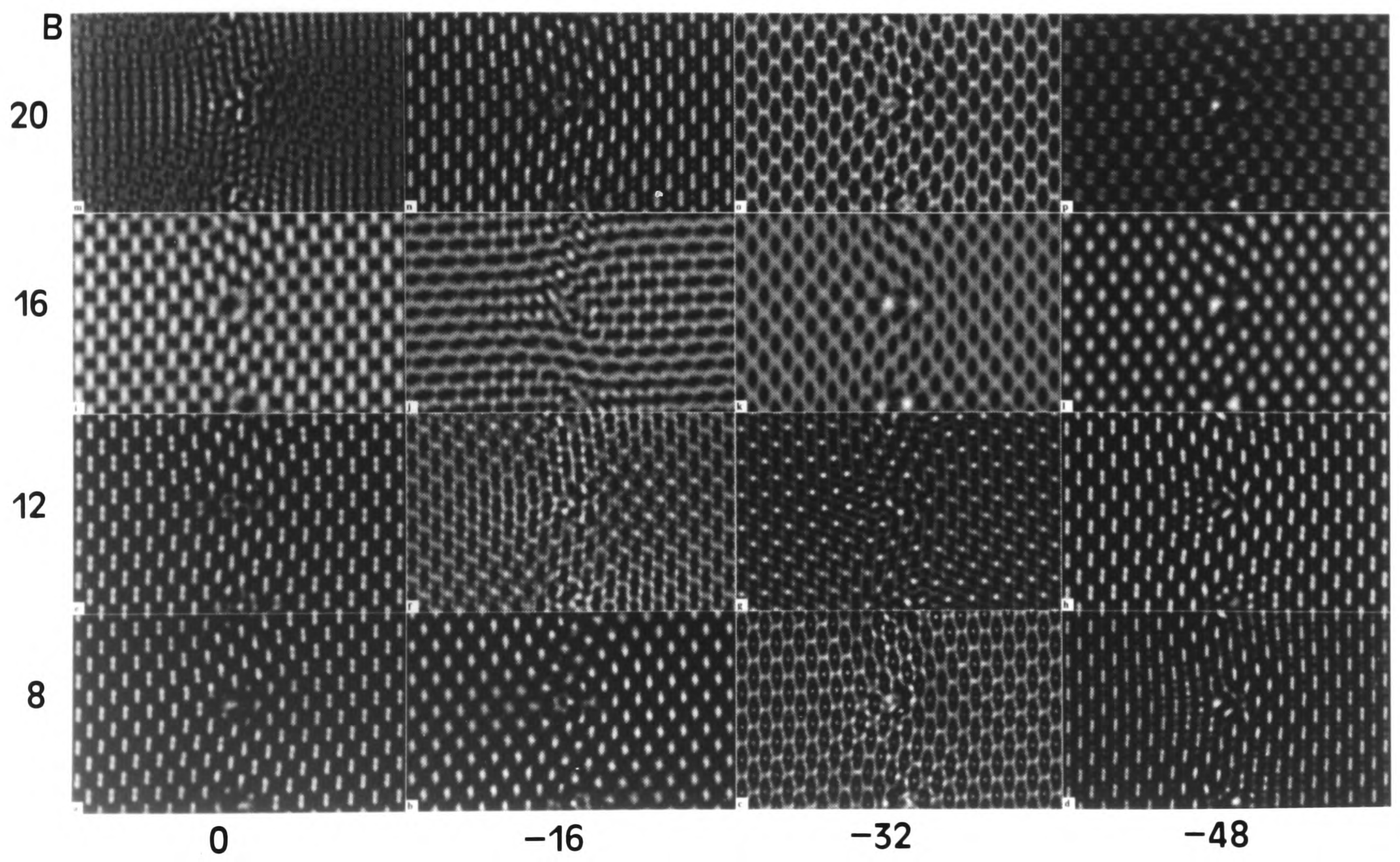
B
20
16
12
8
0
−16
−32
−48

a defocus of -480 Å. This is consistent with the defocus of -480 Å and thickness of 136 Å obtained for the perfect crystal by image matching in the previous section. The superposition of the box in Transparency B (contained in the envelope attached to the back cover of the thesis) on the experimentally obtained image in box B in Figure 5.2 reveals that the two appear to be in reasonable agreement. However, from Figure 5.6 which shows (A) the experimental image of the [001] dislocation and (B) the simulated image and (C) the difference pattern of the two, it is clear that there are marked differences. What appears to the naked eye as a good image match requires a structure refinement to eliminate major differences. However, the difference is localised to just two atoms in the 8-membered ring of the core, as can be seen from Figure 5.7B. Ideally there should be no difference at all and that would lead to a completely black difference pattern, which is clearly not the case in Figure 5.6(C). Nevertheless, from the image matching we can be reasonably confident that the atomic model generated and relaxed in the next section, and used in Transparency B, is a possible structure and that the image observed is a true representation and not an artefact since the differences between the two images is localised to two atoms, but the general bending of planes near the dislocation is correctly presented.

The question of polarity determination invariably creeps into the interpretation of HREM images of compound semiconductors. Ga and As being only two atomic numbers apart have very similar scattering factors and cannot be easily distinguished in the experimental image. The most successful method of polarity determination in GaAs has been convergent beam electron diffraction (Liliental-Weber and Parechanian- Allen, 1986). In the model we assume that the number of wrong bonds at the dislocation core is minimised as far as possible. The dislocation core has two 5-membered rings and an 8-membered ring, all other rings being 6-membered. The sites in the 8-membered ring are occupied, as far as possible, in a way consistent with the occupation of sites

Figure 5.6: A quantitative comparison of A) The digitized experimental image and B) The simulated image cut to the correponding size. C) The difference image. D) The simulated image taking atoms to be in the 'experimental-best-fit' positions. E) The difference image between the digitized experimental image and the simulated image D.

A

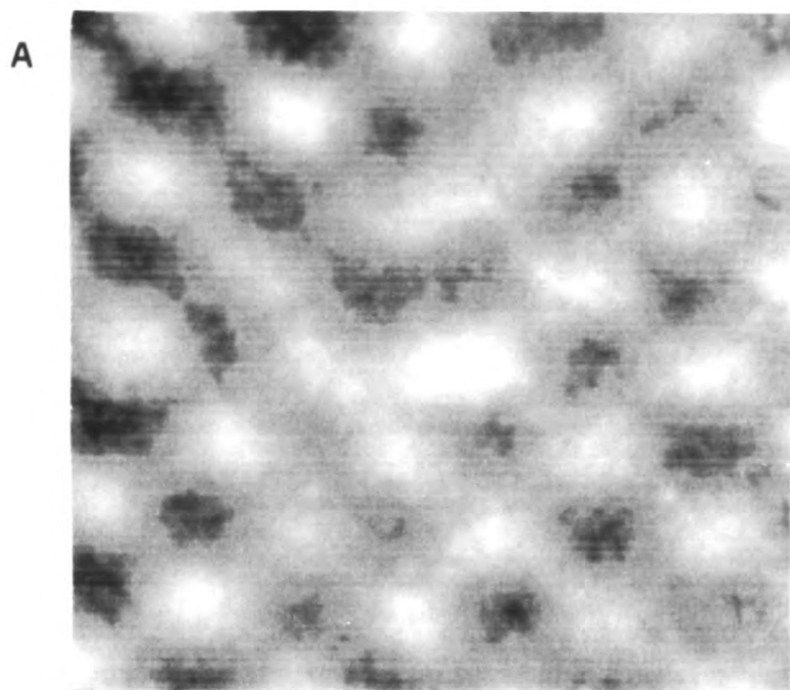

B

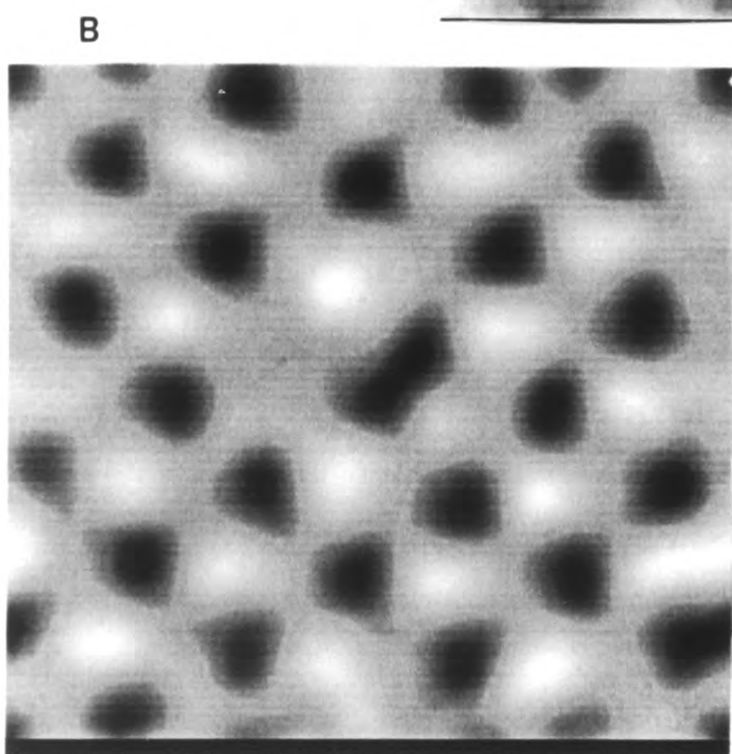

C

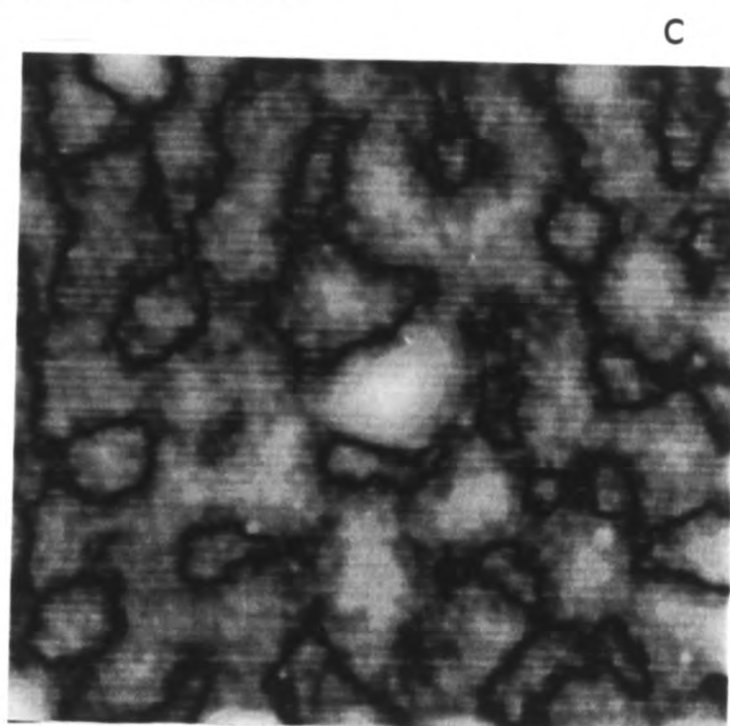

D

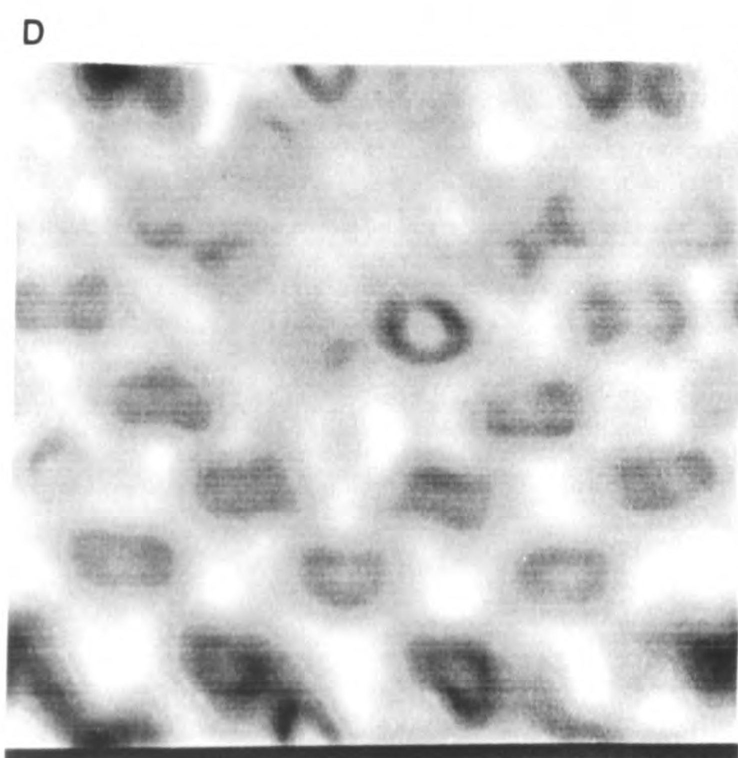

E

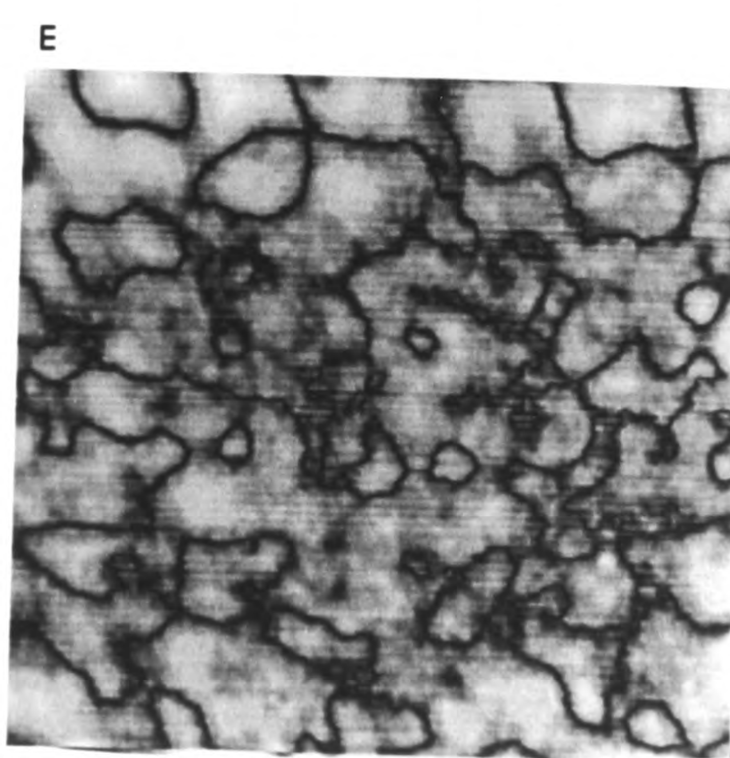

in the surrounding crystal. The four sites to one side of the 8-membered ring which are attached to 6-membered rings, are occupied by Ga and As alternately and are consistent with the surrounding crystal. We are then forced to have a minimum of two wrong bonds. If we choose one to be Ga-Ga then the other must be As-As if we are to have two and not three wrong bonds. These two wrong bonds are where the 5-membered rings are attached to the 8-membered ring. The equivalent positions of the two wrong bonds within a core makes it unnecessary to determine exactly which is the Ga-Ga one and which the As-As. This greatly eases the interpretation of the experimental image as there is no longer a need to know exactly which are the Ga and which the As atoms. For calculations to be tractable it is essential to assume that the dislocation is periodic along the dislocation line. This is because in both the relaxation of the dislocation core and the image simulation, 3-dimensional periodic boundary conditions are imposed on the supercell. No account is taken of relaxation at free surfaces which may well be important at foil thickness under 200 Å. Enforcing periodicity along the dislocation line may restrict local relaxations that may alleviate heavily strained bonds.

The quantitative comparisons and iterative structure refinement process was used to determine the shift in the atomic positions from their relaxed positions that would give the experimental-best-fit. A small region at the [001] dislocation core in the experimental image was isolated and used for comparison with the simulations from an equivalent area of the projected supercell. This smaller block consisted of 54 columns shown in Figure 5.7A where the size difference between Ga and As atoms has been deliberately exaggerated, As being the larger. Figure 5.7B shows the superposition of the atomic positions of 54 columns on the isolated experimental image. Whilst it is not true that the two atoms forming a dumb-bell lie exactly in it, a careful look at the Figure 5.7B reveals that there is an atom lying in the brightest white tunnel, which does seem

Figure 5.7: A) A 54-atom block chosen around a [001] dislocation core for the iterative structure refinement procedure. B) A superposition of the 54-atom block on the digitized experimental image. Note the atom at the centre that is on a white region of the image and appears to require shifting.

A

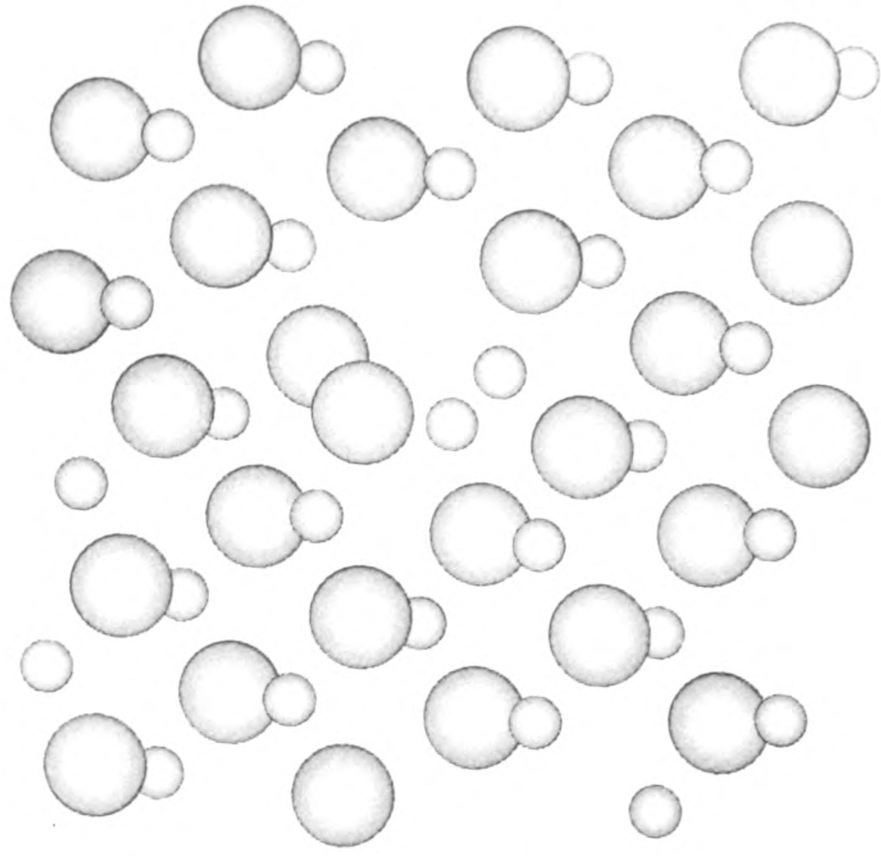

B

out of place. Due to a time constraint it was necessary to limit the number of atoms whose positions were allowed to shift to 10 atoms in the core. It is important to note that the block of 54 columns does not show periodic boundary conditions normal to the columns. The EMS program forcibly imposes these conditions, so distorting the edge of the simulated image each iteration. These edges were discarded in image comparisons made during the iterative refinement. The new simulated and difference images are shown in Figure 5.6D and 5.6E. Figure 5.8 has arrows showing the net shift in atomic positions from their atomically relaxed positions. The resultant displacements are listed in Table 5.2 and this structure is referred to as the experimental-best-fit structure. There are large shifts and the new core is not a feasible structure. The atoms have shifted too far away to bond and the presence of isolated atoms is unrealistic. It must be borne in mind that while the structure refinement procedure can shift atoms anywhere within the supercell it cannot remove an atom completely, thus there are limitations imposed on the refinement. In conclusion, the structure refinement has not yielded a plausible model for the dislocation core. The original model is far more plausible from a chemical and physical point of view, even though it does not give such good agreement with the experimental image.

The differences in the image simulated from the original model and the experimental image may be due to one or more reasons:

- The experimental image may consist of several overlapping cores because the dislocation core structure may vary along the dislocation line. This may, in part, be because of the 0.7 degree misalignment of the [110] axis in the two crystals.
- In the atomic relaxation it was a dislocation dipole and not an isolated dislocation that was relaxed. Interaction between cores may affect the atomic positions determined. For example, the bending of planes near the core is much stronger in the simulated image than in the HREM image.

Figure 5.8: The net shift in the atomic positions of 10 pre-selected atoms from their initial structure to the 'experimental-best-fit' positions, indicated by arrows.

Atom	Initial Position (X, Y)	Final position (X, Y)	Net Shift $(\Delta X, \Delta Y)$	Shift Å
Ga	(0.6002, 0.4899)	(0.5884, 0.4279)	(0.0118, 0.062)	1.05
Ga	(0.7839, 0.2681)	(0.8051, 0.2318)	(0.0212, 0.036)	0.70
As	(0.4305, 0.4276)	(0.4128, 0.4092)	(0.0177, 0.018)	0.43
Ga	(0.3973, 0.2809)	(0.3210, 0.2963)	(0.0763, 0.015)	1.37
As	(0.4886, 0.4993)	(0.4622, 0.3897)	(0.0264, 0.109)	1.88
As	(0.6984, 0.2758)	(0.6584, 0.1338)	(0.0400, 0.142)	2.46
Ga	(0.6589, 0.4196)	(0.7968, 0.2980)	(0.0479, 0.122)	2.18
As	(0.3128, 0.2748)	(0.2311, 0.2333)	(0.0817, 0.042)	1.59
Ga	(0.6001, 0.1810)	(0.5704, 0.1021)	(0.1029, 0.079)	1.41
As	(0.5081, 0.1802)	(0.4793, 0.0972)	(0.0288, 0.083)	1.47

Table 5.2: Shift in atomic positions resulting from iterative structure refinement.

- The boundary seen in the experiment has been analyzed and modelled as a perfect symmetric tilt boundary which is not the case. In truth it is an asymmetric tilt boundary.

- No account has been taken of possible impurity atoms sitting in the dislocation core. This is more than likely to be the case at such a large core, which will be an attractive site for misfitting atoms.

- No account has been taken of an oxide layer that may well be present on the specimen surface.

None of the above factors is trivial, nor are they easily resolved. Fully aware of these issues I have attempted to be cautious in drawing conclusions.

5.3 Relaxation of the [001] dislocation

Section 4.5 described how the [001] edge dislocation was constructed geometrically. In this section the geometric models are relaxed to estimate the atomic positions at the defect, using various routines based on the theories described in Chapter 3. Several different relaxations have been performed to be able to gather as much quantitative information as possible while making a minimum number of assumptions and approximations. The results presented here are not from first principles calculations and therefore necessarily involve approximations.

5.3.1 Relaxation using a classical potential

Energy minimisation using the Tersoff classical potential (Tersoff, 1986) for defining the inter-atomic forces was used to relax the 446-atom and 336-atom supercells described in Section 4.3. The short range inter-atomic forces may relax the geometry to a particular core structure or sometimes there is a set of different core structures that have similar

low energies. Elasticity theory and the presence of a dislocation dipole ensure that there are no long range stresses.

Both the supercells here consist entirely of Si atoms and the empirical parameters used were those for Si given by Tersoff (1988). Since the corresponding empirical values for GaAs parameters are not available for the Tersoff potential it was not possible to relax a GaAs supercell. Use is therefore made of the empirical parameters for Si as it shows the same sphalerite structure and tetrahedral coordination.

A dynamic relaxation was performed, in which the atoms have sufficient kinetic energy to find, at least in principle, the global minimum of energy. For this 26,000 time steps of annealing was carried out at 1300^0 K and then the system quenched (Finnis, 1990) to give the global minimum configuration. At temperatures higher than 1300^0 K the block of atoms begins to melt.

The relaxed core is shown in projection in Figure 5.9 where some bonds have been indexed to facilitate reference to them. All atoms were found to be four fold coordinated. Each dislocation is associated with an eight-membered ring and two five-membered rings as marked out in the figure. A cutoff of 0.50**a** is used for defining a bond, which means allowing bonds to be 15% stretched from their perfect crystal value. The bond length distortion for the 336 atom supercell varied between a stretch of 9.68% and a compression of 2.61% and the bond angles were a maximum of 137.09^0 and a minimum of 90.55^0; while the 446 atom supercell had a maximum bond stretch of 14.4% and minimum of 2.49% and the bond angle ranged from 141.43^0 to 88.13^0. The differences in the core structures are tabulated in Table 4.1 in which bonds are indexed as shown in the Figure 5.9. These numbers show the results are converged with respect to box size, except for the bond indexed 4, which varies in the amount it is stretched depending on the box size, relaxation technique and treatment, as shown in Table 5.3. The variation in bond stretch suggests the bond lies in a highly strained

Figure 5.9: A [110] projection of the reconstructed [001] dislocation core. The bonds have been indexed to facilitate reference to them in the text and tables.

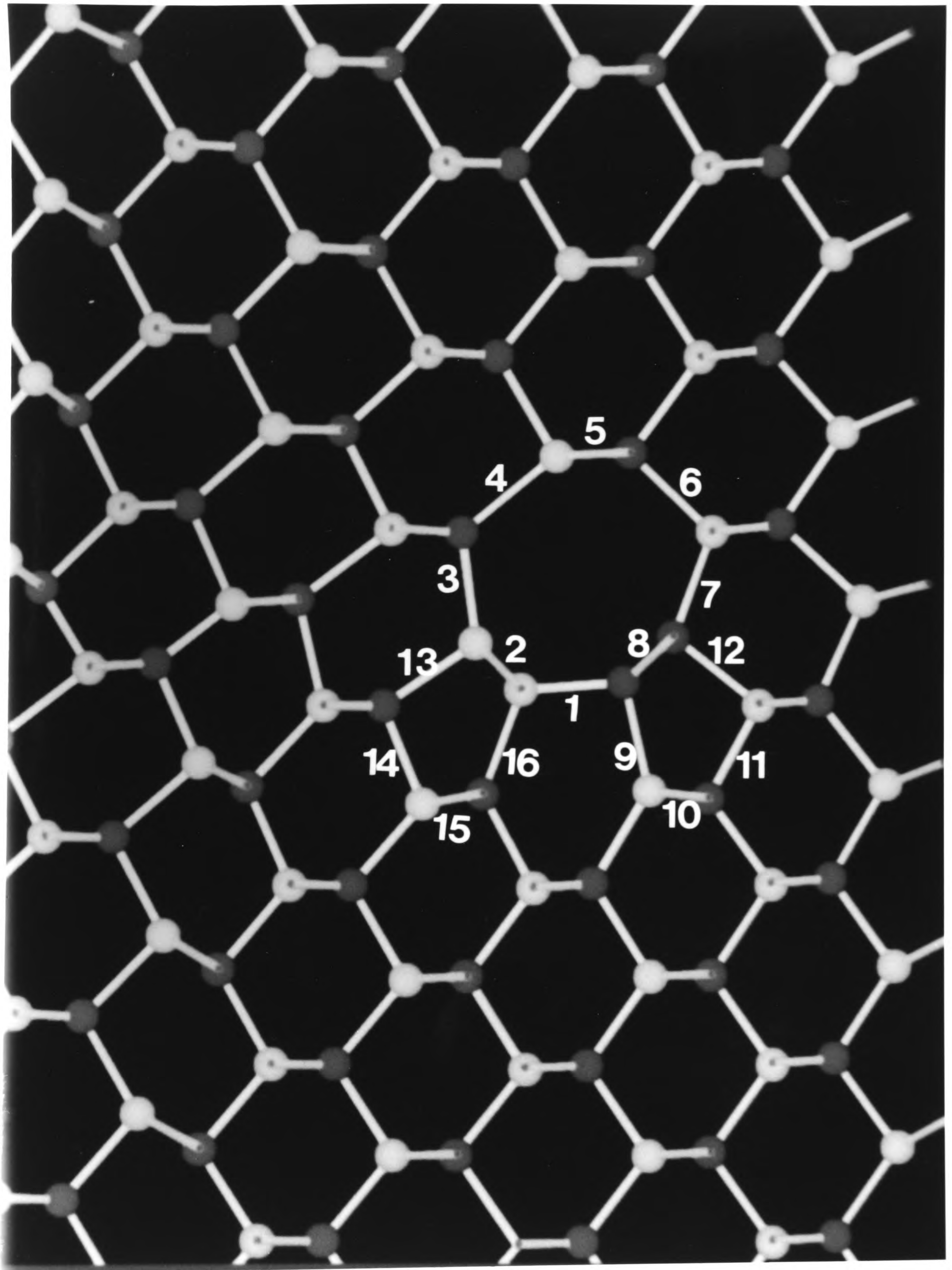

5
4
6
3
7
2
8
12
13
1
14
16
9
11
15
10

Bond 4	Supercell	Potential	Treatment
9.7%	336 1 dipole	Tersoff Si	Annealed then Quenched
14.2%	446 2 dipoles	Tersoff Si	Annealed then Quenched
10.0%	446 2 dipoles	BOP Si	Conjugate gradient
16.7%	336 1 dipole	TB GaAs	Annealed then Quenched

Table 5.3: Variation in bond length with box size, potential and treatment.

region of the core. These configurations were then further relaxed using a Bond Order potential constructed for Si. It was also relaxed by carrying out a tight binding matrix diagonalization for GaAs.

5.3.2 The Bond Order Potential (BOP) relaxation

The 446 atom block was relaxed as silicon using BOP, a program developed by A.P. Horsfield at the Materials Modelling Laboratory (MML), based on the bond order potential. This relaxation was run on the MML computers. A conjugate gradient relaxation was performed with 12 moments and locally oriented orbitals. The input file used can be seen in Appendix C, where all the parameters used are listed. The relaxed structure obtained here was not very different from that obtained by Tersoff, which is as expected owing to the similarity between the Tersoff potential and the bond order potential. The detailed differences in bond distortions between the relaxed structures are tabulated in Table 5.4.

The program failed to work for GaAs. The reasons for such behaviour are being looked into at the MML currently.

5.3.3 The Tight-binding relaxation

The tight-binding **k**-space scheme was used to relax the 336-atom block using a code written initially by McInnes (1992) and developed further by Bigger (1992) and Goringe (1994) and run on the Oxford University Convex. Empirical values for the hopping parameters were those given by Chadi (1984) for GaAs. The initial configuration was the relaxed structure obtained for silicon using the Tersoff relaxation.

Only one **k**-point was used in the averaging scheme mentioned in Chapter 3. This **k**-point was at [110]**a**/4 along the dislocation line and weighted 1. Relaxation was carried out till the force on each atom was less than 10^{-6} eV/Å. The maximum tensile and compressive bond length distortions were 16% and 6.85% respectively. The 16% stretched bond, which was 14% stretched in the Tersoff relaxation for Si. A 336 atom block is not sufficiently large to ensure that the two cores do not modify each other, but dealing with a larger supercell is too demanding on computer time since the matrix diagonalization method is an order N^3 algorithm, and hence not feasible. The bond angles ranged between 137^0 and 89^0. Other than bond length distortions these results are similar to those obtained by Bigger (1992) for the reconstructed 90^0 partial in Si using a Chadi Hamiltonian, in that all atoms are four-fold coordinated and there is no bond reconstruction along the dislocation line. Relaxations with the Tersoff potential and BOP resulted in bond angle deviations being similar to those obtained here but the bond length distortions were much less. Table 5.4 gives a comparison of the bond lengths and their percentage distortions for the supercell relaxed with Tersoff, BOP and that of GaAs relaxed by tight binding, in each case the distortion being relative to the normal bond length of $\mathbf{a}\sqrt{3}/4$ in the material. Figures 5.10 and 5.11 show the various relaxed cores obtained from different relaxation schemes. Table 5.5 compares the maximum bond distortions in the 336-atom supercell treated with Tersoff as Si and relaxed with tight binding as GaAs, and also gives the length of wrong bonds.

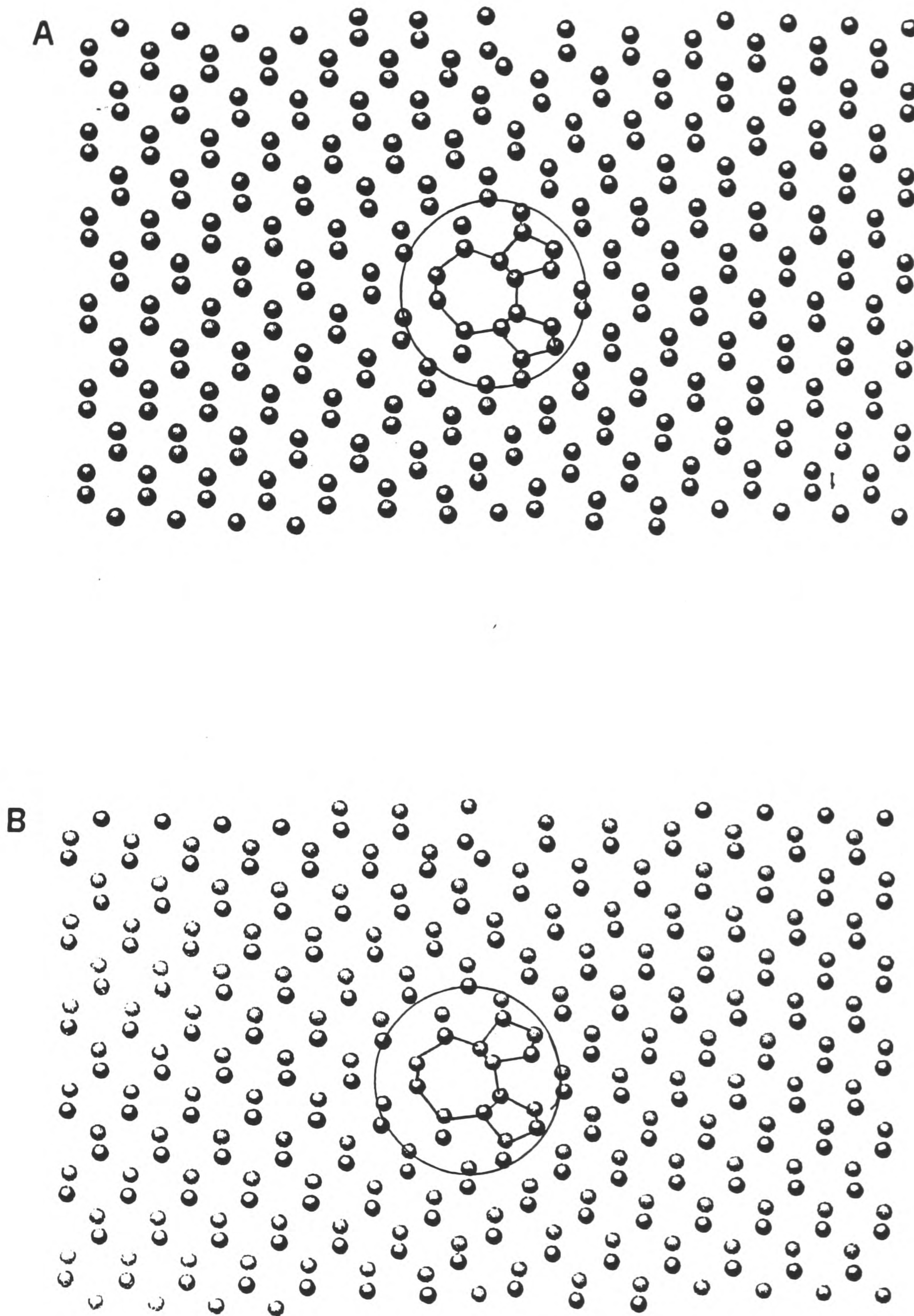

Figure 5.10: A comparative study of the relaxed cores obtained from the 336 atom supercell using a A) Tersoff scheme for Si and B) the tight binding **k**-space scheme for GaAs.

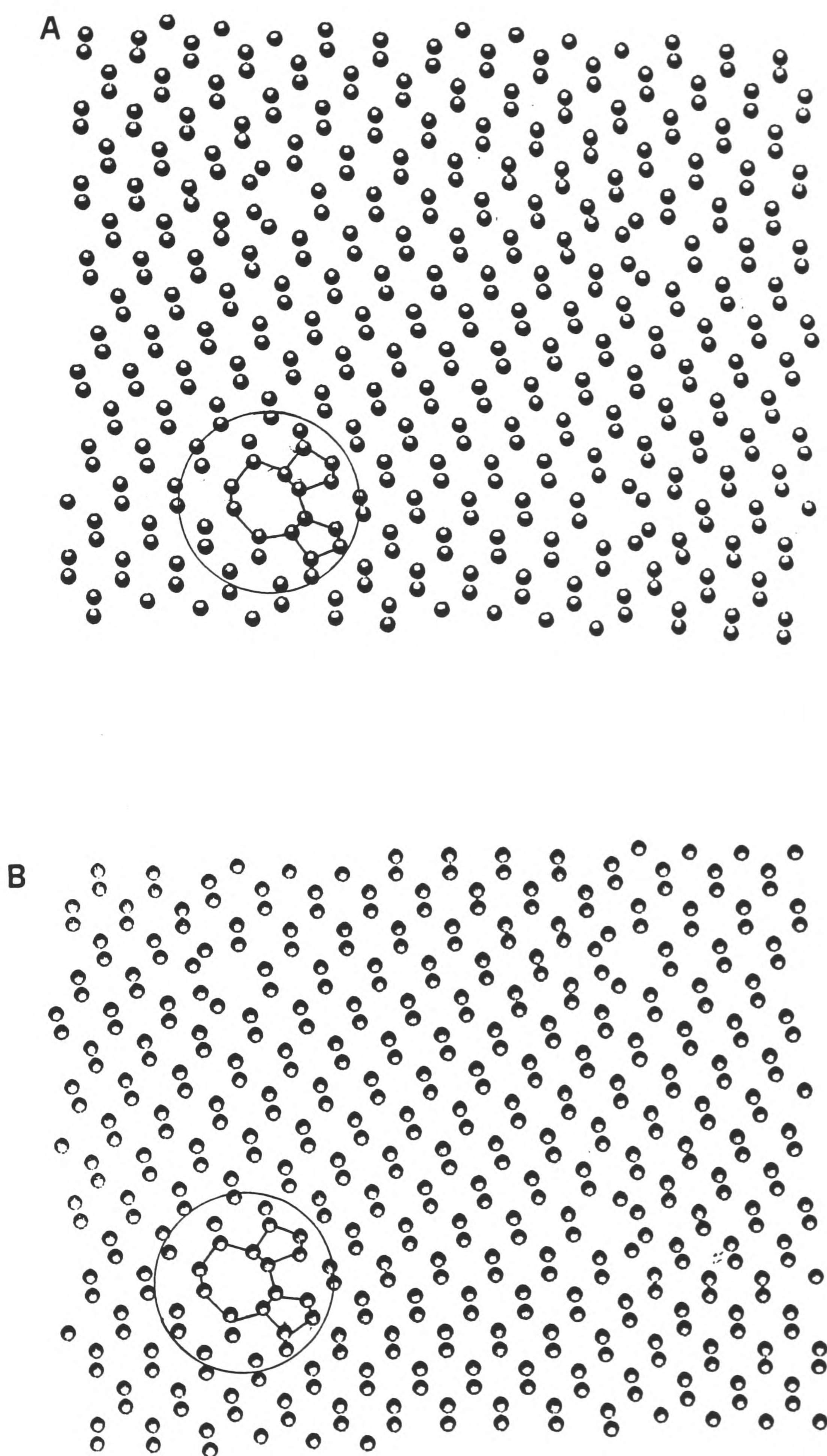

Figure 5.11: A comparative study of the relaxed cores obtained from the 446 atom supercell using A) Tersoff and B) BOP schemes for Si.

Bond Index Block Size	TB GaAs 336	BOP Si 446	Tersoff Si 446	Tersoff Si 336
1	1.3	1.1	2.3	1.1
2	8.4#	-0.4	-0.3	-0.7
3	0.7	2.1	2.0	1.4
5	5.0	4.9	6.2	5.9
6	3.5	2.2	3.2	4.3
7	11.6	4.0	3.2	1.8
8	0.3*	1.2	1.4	1.3
9	1.5	3.6	4.2	2.8
10	-2.7	-0.9	-1.3	-1.7
11	-4.2	-0.8	-1.2	-2.2
12	-2.7	-0.1	0.4	0.6
13	5.6	2.5	1.5	1.5
14	-5.3	-2.5	-2.2	-2.6
15	-1.8	-1.4	-2.0	-2.0
16	8.3	2.1	2.4	1.9

Table 5.4: Comparative percentage bond distortions in relaxed core structures of [001] dislocations, obtained for different potentials. * marks a Ga-Ga wrong bond, and # an As-As wrong bond.

The valence and lower conduction bands of the tetrahedrally coordinated semiconductors can be obtained within the tight-binding model. The next section gives information regarding the electronic structure obtained for the core atoms in the [001] edge dislocation.

5.4 Band structure and electronic states

The band structure was obtained for the tight binding relaxed 336-atom GaAs supercell using the Vogl *et al.* (1983) empirical tight-binding interactions and parameters for GaAs in the sp^3s^* model. The repeat vector along the dislocation line is [110]a/2 corresponding to a periodicity of $\mathbf{c}=0.707\mathbf{a}$ that remains unchanged during relaxation. Unidimensional dispersion of bands in the range $0 < \mathbf{k} < \pi/\mathbf{c}$ is obtained using just one

Bond Distortions	Tersoff Potential Si	Tight Binding GaAs
Maximum stretch	9.68%	16.78% (Ga-As)
Maximum compression	-2.61%	-6.85% (Ga-As)
Maximum angle	137.09^0	137.23^0
Minimum angle	90.55^0	89.16^0
Bond	**Length in a**	**Remark**
b-c	0.399	Ga-Ga strong bond
h-i	0.406	
a-a'	0.434	As-As wrong bond
k-j	0.431	
Ga-As bond	0.433	undistorted bond

Table 5.5: Comparison of relaxed [001] dislocation core structures

supercell. Figure 5.13 shows this band structure obtained from the defect-containing supercell. The perfect crystal shows a band gap of 1.55 eV in agreement with Vogl *et al.* (1983). Note that associated with the core of the defects are seen two deep (0.72 and 0.99 eV) and two shallow states in the band gap. The presence of deep states despite tetra-coordination is interesting.

Table 5.6 lists the index number of the atoms with which the localised states are associated and their weights. The strongly weighted atoms are circled in Figure 5.12 from where it can be seen that the 0.99 eV and 0.716 eV states are localised at the Ga-Ga wrong bond. The shallow states are distributed over the atoms at the core and probably are a consequence of bond distortions found in the core. The weight refers to the percentage contribution of the atom to the state. It is clear that the two deep states result from one dislocation core each, suggesting that they are possibly degenerate states, appearing 0.275 eV apart in Figure 5.13 as a result of interaction between them. The limit on the separation between the cores along [001], and hence

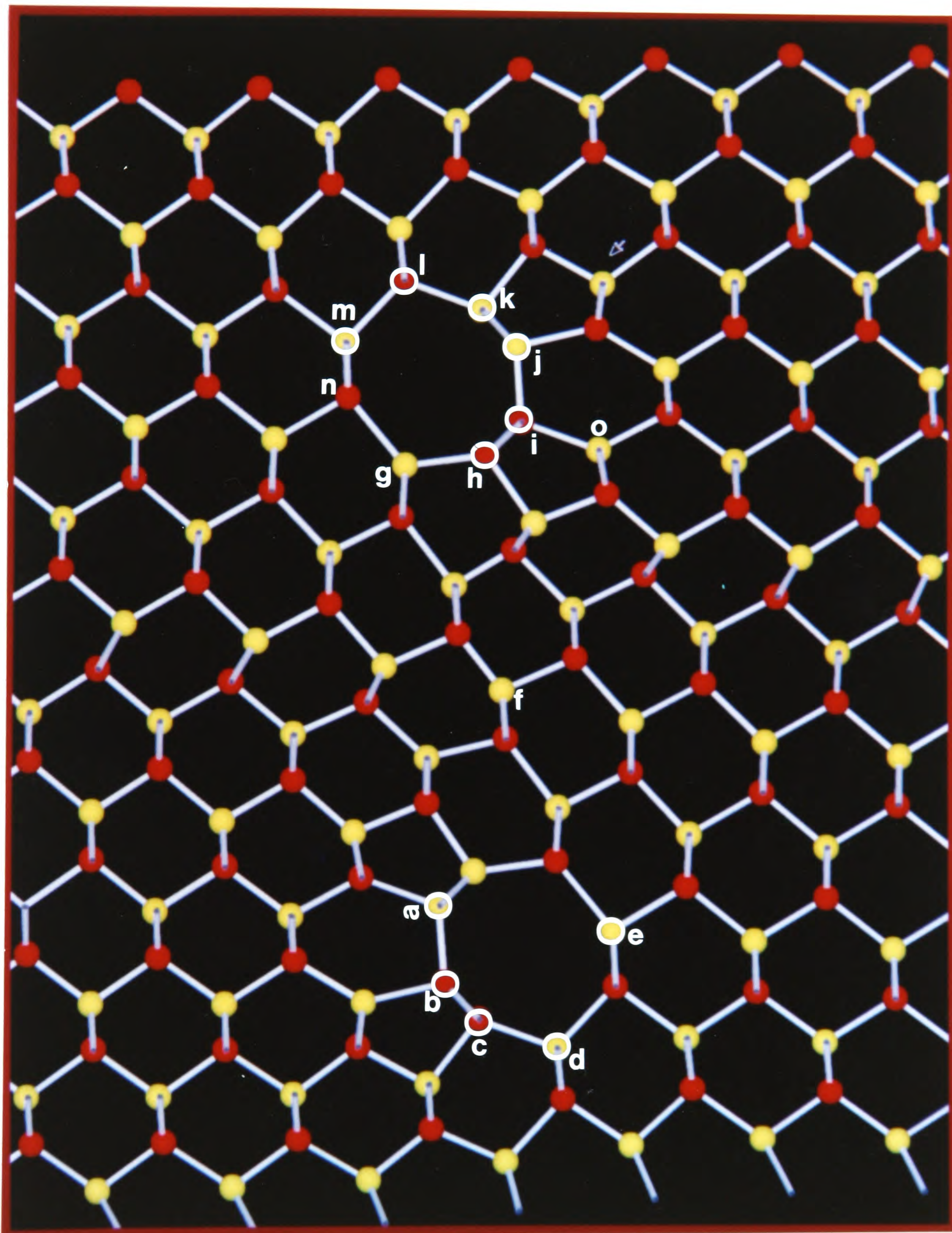

Figure 5.12: This figure illustrates the atoms associated with the states in the gap at the [001] dislocation core. See Table 5.6.

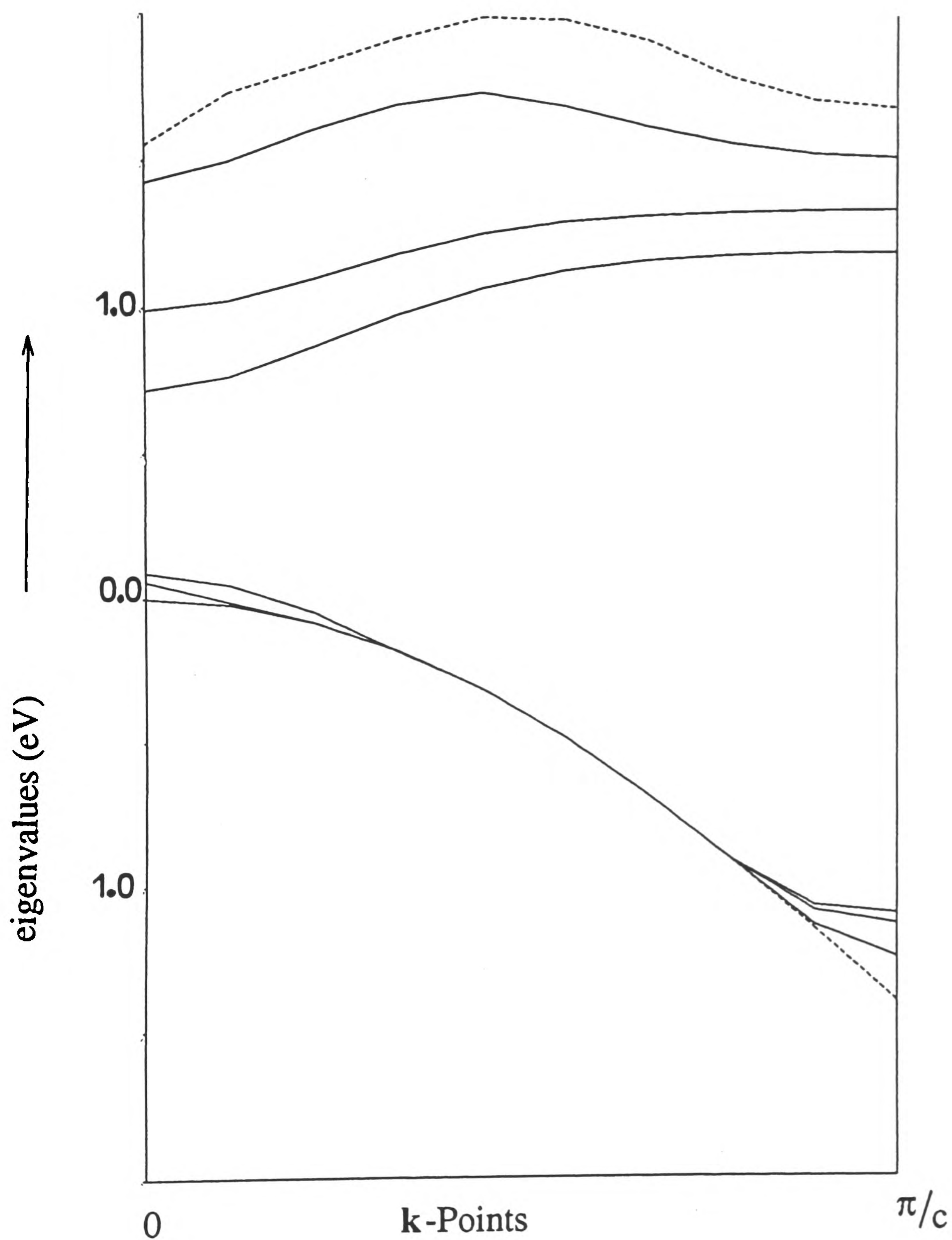

Figure 5.13: The projected band structure along the dislocation line for the 336-atom GaAs supercell relaxed by the **k**-space tight binding code and the Vogl sp^3s^* Hamiltonian. The dashed lines show the edges of the bulk valence and conduction bands. Note the presence of deep and shallow states in the gap. The deep states are associated with atoms at the core, as can be seen from Table 5.6 and these atoms are marked out in Figure 5.12. The shallow states have weight distributed over the core.

Level eV	Atom Index	Total Weight	s	p_x	p_y	p_z
0.057	l	0.04	0.00	0.00	0.00	0.04
	k	0.11	0.00	0.00	0.00	0.10
	j	0.12	0.00	0.01	0.00	0.11
0.089	k	0.09	0.00	0.00	0.00	0.08
	j	0.09	0.00	0.01	0.00	0.08
0.716	a	0.05	0.00	0.04	0.00	0.00
	c	0.32	0.08	0.14	0.05	0.02
	d	0.09	0.02	0.00	0.07	0.00
	b	0.27	0.10	0.05	0.08	0.01
0.991	i	0.32	0.08	0.08	0.09	0.01
	o	0.05	0.01	0.02	0.03	0.00
	h	0.30	0.09	0.11	0.05	0.03
	j	0.09	0.00	0.08	0.00	0.00
1.427	m	0.07	0.06	0.00	0.00	0.01
	g	0.08	0.06	0.00	0.02	0.00
	f	0.06	0.04	0.00	0.02	0.00
	e	0.09	0.07	0.00	0.01	0.00

Table 5.6: Weighting and occurrence of localised states in the reconstructed [001] core obtained for tight binding relaxation. See Figure 5.12 for atom indexing, red spots indicate Ga atoms.

the accuracy to which states associated with an isolated dislocation are known is set by the number of atoms that the program can relax, 336 being very near the upper limit for the computing power available. A faster and more efficient version has been developed by Goringe (1994) that can handle more atoms, although it cannot calculate band structures as it is a real space method. Since the Fermi level for the perfect supercell is 1.28 eV and that for the defect supercell is 0.45 eV the deep states are not occupied while the shallow ones are. Table 5.7 gives the charge on each atom. Notice that there is a charge transfer of about ± 0.42 electrons to Ga and ± 0.31 electrons to As atoms in the dislocation core, as opposed to a transfer of 0.23 electrons from Ga to As atoms in the perfect crystal. It is interesting to note that the charge transfer within the core is not simply determined by the difference in electronegativity between Ga and

Atom	Type	Electrons	Atom	Type	Electrons
1	As	5.23			
2	As	5.23			
15	Ga	2.77			
7	As	5.23	288	As	5.25
20	Ga	2.62	302	Ga	3.30
202	As	5.24	105	Ga	3.24
217	Ga	2.61	287	As	4.69
203	As	4.73	120	As	4.72
36	As	4.70	134	Ga	2.46
218	Ga	3.22	121	As	5.21
21	Ga	3.30	303	Ga	2.58
8	As	5.28	301	Ga	2.78
22	Ga	2.92	119	As	5.26
204	As	5.28	133	Ga	2.88
50	Ga	2.80	259	As	5.30
232	As	5.27	273	Ga	2.90
246	Ga	2.90	91	As	5.29

Table 5.7: Charges on atoms in Tight Binding relaxation. The atoms are indexed as in Appendix D.

As. Thus in the core, some Ga atoms acquire an excess and some As atoms a deficit of electronic charge. However, the numerical values of these charge transfers cannot be taken too seriously since the calculation is not self-consistent. In a self-consistent calculation, where screening would be taken into account, the charge transfers would be considerably smaller in magnitude.

5.5 Summary and Conclusion

Briefly outlining the work reported in this chapter it is fair to say that extensive use has been made of various atomic relaxation schemes ranging from classical potentials to semi- empirical tight-binding codes in order to obtain a consistent and physically plausible atomic structure of the [001] dislocation. This structure has then been used to

simulate a high resolution image to compare it with that experimentally obtained and presented in Chapter 4. Detailed quantitative comparisons were made with the real and simulated images and an experimental-best-fit structure determined by iterative refinement to the relaxed core. The structure obtained is not physically plausible and hence cannot be taken too seriously. It is the result of complete neglect of atomic interactions. If this structure is fed into any of the relaxation schemes the atoms move back to their original relaxed core positions. Although there are differences in the relaxed cores obtained from various techniques, differences between them are minor compared to the difference between any of them and the experimental-best-fit structure. It must be borne in mind that while simulation of HREM images are essential to analysis, the accurate matching of the two are not proof of a given structure though it may be used to certify that a structure under consideration is a possible one. There are far more factors, such as those listed in Section 5.2.3, involved in real high resolution imaging than are incorporated in the best simulation packages.

And finally, the electronic structure calculated from the tight-binding relaxed 336-atom supercell revealed the presence of states in the gap. The deep states were found to arise from the short (hence strong) Ga-Ga wrong bond located in the compressive region of the dislocation core. The states are not occupied. It would be of considerable interest to verify the presence of this state experimentally.

Chapter 6

The Undissociated 60^0 Dislocation

6.1 Introduction to 60^0 Dislocations

The **b**=**a**/2$< 110 >$ dislocations that run along $< 110 >$ and lie on the $\{111\}$ planes in a diamond lattice are of three types: the edge dislocation, the screw dislocation and the 60^0 dislocations. When a dislocation is referred to by an angle it is the angle between the dislocation line and the Burgers vector that is stated. The line of an edge dislocation is perpendicular to its Burgers vector and in the case of a screw dislocation the two are parallel. A dislocation may further be classified into glide and shuffle depending on whether the extra-half plane ends between two narrow or widely spaced $\{111\}$ planes, and in the case of compound semiconductors further still into α and β dislocations, as explained in Chapter 2. Whether dislocations preferentially exist in the glide or shuffle state in GaAs has not yet been determined.

Using the weak beam technique (Cockayne *et al.*, 1969), it was shown that most perfect dislocations in Si (Ray *et al.*, 1971), Ge (Haüssermann and Schaumburg, 1973), and III-V compounds (Gottschalk *et al.*, 1978; Gomez and Hirsch, 1978), are generally dissociated into two Shockley partials over most of their lengths. The Burgers vectors of all three dislocations lie in the same $\{111\}$ plane. Such a dislocation configuration is known as an extended dislocation and it is energetically favourable as can be seen

from the reaction:

$$\mathbf{a}/2[01\bar{1}] \rightarrow \mathbf{a}/6[\bar{1}2\bar{1}] + \mathbf{a}/6[11\bar{2}] \quad (6.1)$$

$$(a^2/2) \rightarrow (a^2/6) + (a^2/6). \quad (6.2)$$

However, recent studies (Gerthsen and Carter, 1993) showed that a significant fraction of the dislocations that were introduced by deformation were undissociated. This fraction was estimated at about 20% in semi-insulating GaAs.

An edge dislocation dissociates into two 60^0 partials, a screw dislocation into two 30^0 partials and the perfect 60^0 dislocation can dissociate into a 30^0 and a 90^0 partial. An intrinsic or extrinsic stacking fault lies in the region between the two partials as the Burgers vectors of the partials are not lattice translation vectors.

There has been much interest in determining the atomic and electronic structures in the cores of the three basic types of dislocations (i.e. 30^0, 60^0 and 90^0 Shockley partials). Dislocation cores have been observed experimentally by several techniques, edge on imaging of a dislocation using HREM being the most informative for non-screw orientations. Several chemically and energetically possible structures of the cores have been suggested by theoretical modelling techniques and some have been confirmed experimentally. The study of the dislocation core structures in semiconductors is summarised in Tables 6.1, 6.2 and 6.3, which list the main dislocations observed in Ge, Si and semi-insulating GaAs and the theoretical models for their core structures, giving some references.

The 60^0 dislocation has largely been observed as an extended dislocation, dissociated into 30^0 and 90^0 Shockley partials, with an intrinsic stacking fault lying between the two partials. Estimates of the stacking fault energy and length have also been made. In this chapter we report on our study of the undissociated 60^0 dislocation in GaAs. Although comparison here is made with dislocations found in the bulk (unless otherwise stated), Bullough (1955) showed that the dislocations in a grain boundary

Dislocation Type	Stacking fault	HREM	Model
Perfect 60^0	none	Chisholm *et al.*(1990)	
Edge $\rightarrow 60^0 + 60^0$	63±13 mJ/m^2	Bourret *et al.*(1979)	
$60^0 \rightarrow 30^0 + 90^0$	100±10 mJ/m^2	Desseaux *et al.* (1978)	30^0, 90^0 Teichler (1989)
screw $\rightarrow 30^0 + 30^0$	75 mJ/m^2	Möller (1978)	

Table 6.1: Current understanding of dislocations in Ge.

Dislocation Type	Stacking fault	HREM	Model
Perfect 60^0	none	Hutchison *et al.*(1983)	Hornstra (1958)
Edge $\rightarrow 60^0 + 60^0$	51±5 mJ/m^2	Spence and Kolar (1979)	Veth and Teichler (1984)
$60^0 \rightarrow 30^0 + 90^0$		Anstis *et al.*(1981)	30^0: Hirsch (1979) Heggie and Jones (1987) 90^0: Hirsch (1979) Jones(1979)
screw $\rightarrow 30^0 + 30^0$			30^0 as above

Table 6.2: Current understanding of dislocations in Si.

Dislocation Type	Stacking Fault	HREM	Core Model
Perfect [001]	none	Krakow and Smith (1987)	Chapter 5
Perfect 60^0	none	Chapter 4	Chapter 6
Edge $\rightarrow 60^0 + 60^0$	44±6 mJ/m^2	Maksimov *et al.* (1987)	
$60^0 \rightarrow 30^0 + 90^0$	6.58±1.04 nm	Gerthsen and Carter (1993)	Jones *et al.*(1993)
screw $\rightarrow 30^0 + 30^0$	4.5±0.35 nm	DeCooman and Carter (1987)	

Table 6.3: Current understanding of dislocations in GaAs

exhibit narrower cores than they do in the bulk. This narrowness leads to a greater Peierls stress being required to move the dislocation. The Peierls stress required varies exponentially with dislocation core width. The same reasoning would indicate the separation of dissociated partials of extended dislocations in a low angle grain boundary is less than in the bulk. Perhaps factors such as the lack of coherence at an interface and the proximity of other dislocations in the interface favour a slightly different bond reconstruction.

6.1.1 Geometry of the supercell

The programs used to generate geometrically and subsequently relax the supercell are exactly those used in the previous chapter and described in Chapter 3. A rectangular supercell of dimensions $6[001] \times 7[1\bar{1}0] \times [110]$ was generated and two sets of dislocation dipoles introduced in it as shown in Figure 6.1. At the upper left hand corner of the supercell is a $\mathbf{a}/2[101]$ dislocation with $\mathbf{a}/4[1\bar{1}2]$ edge and $\mathbf{a}/4[110]$ screw components, and the upper right hand dislocation has an equal and opposite Burgers vector. Note that the upper left dislocation is a Ga(glide) while the upper right dislocation is an As(glide). The lower left dislocation is an As(glide) and has a Burgers vector of $\mathbf{a}/2[\bar{1}01]$ with $\mathbf{a}/4[\bar{1}12]$ edge component and $\mathbf{a}/4[\overline{11}0]$ screw component, the lower right dislocation being its equal and opposite is a Ga(glide). Thus we have generated two grain boundaries perpendicular to [001] in one supercell, each boundary having two 60^0 dislocations per period. The screw components of the two dislocations in one period of the boundary cancel out ensuring there is no net twist content in the boundary. In order to achieve this we are forced to have four dislocations in a supercell, and hence a quadrupolar unit cell.

The net dislocation content per period of the boundary is [001], as can be seen from

Figure 6.1: A [110] projection of the 672-atom supercell used in atomic relaxations. The supercell contains two 60^0 dislocation dipoles and its period is 2 [110]/2 along the line of projection. The As atoms are shown larger than Ga for clarity.

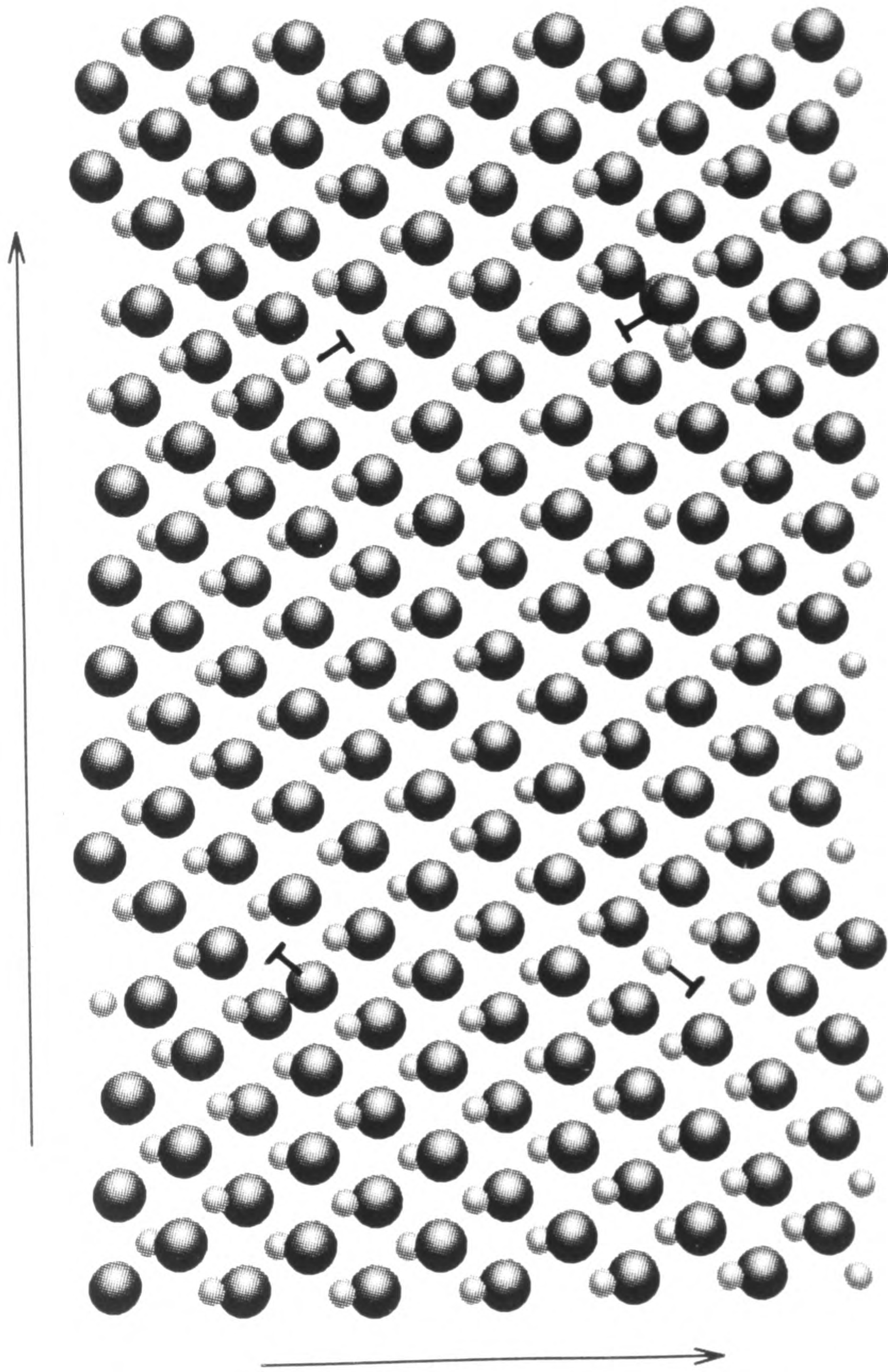
[1 $\bar{1}$ 0]
[0 0 1]

the equation below.

$$\mathbf{a}/2[101] + \mathbf{a}/2[\bar{1}01] \rightarrow \mathbf{a}[001] \qquad (6.3)$$

The dislocations are not sufficiently far apart for us to be certain they are not interacting, but larger spacing between the two boundaries in the unit cell would mean prohibitively increased computational time.

Bigger *et al.* (1992) showed the importance of the height of the repeat cell, d_0, being commensurate with the periodicity of the grain boundaries generated. In Figures 6.2A and 6.2B consider a grain boundary running along $[1\bar{1}0]$ as shown by line AC, generated by a set of $\mathbf{a}/2<110>$ dislocations. Per period, the boundaries in the supercell contain a net Burgers vector of $\mathbf{b}=\mathbf{a}[001]$ and $\mathbf{b}=\mathbf{a}[00\bar{1}]$ respectively. The dislocations impart an equal and opposite displacement of $\mathbf{a}/2[001]$ in each boundary period to either grain, as shown at site C. From the triangle ABC or ADC, it is clear that a similar triangle of double the scale would have the vector B′C′ ending at another atom that is equivalent to the atom at site C. The presence of the screw components of $\mathbf{a}/4[110]$ exactly cancel out. Hence, the period of the $\theta=11.5^0$ grain boundary normal to [110] is $14[1\bar{1}0]$ units as opposed to $7[1\bar{1}0]$ that we have taken. In order to keep the number of atoms and the number of dislocation dipole sets within computational limitations the periodicity along the $[1\bar{1}0]$ has been halved for the supercell. This imparts a small but finite misfit at the boundary of the supercell which can be dispersed throughout the supercell during the relaxation by setting up a small, finite, homogeneous strain. The importance of this strain is not negligible, but it was not possible to work with 4 sets of dislocation dipoles per supercell since this would have doubled the number of atoms in the supercell.

A

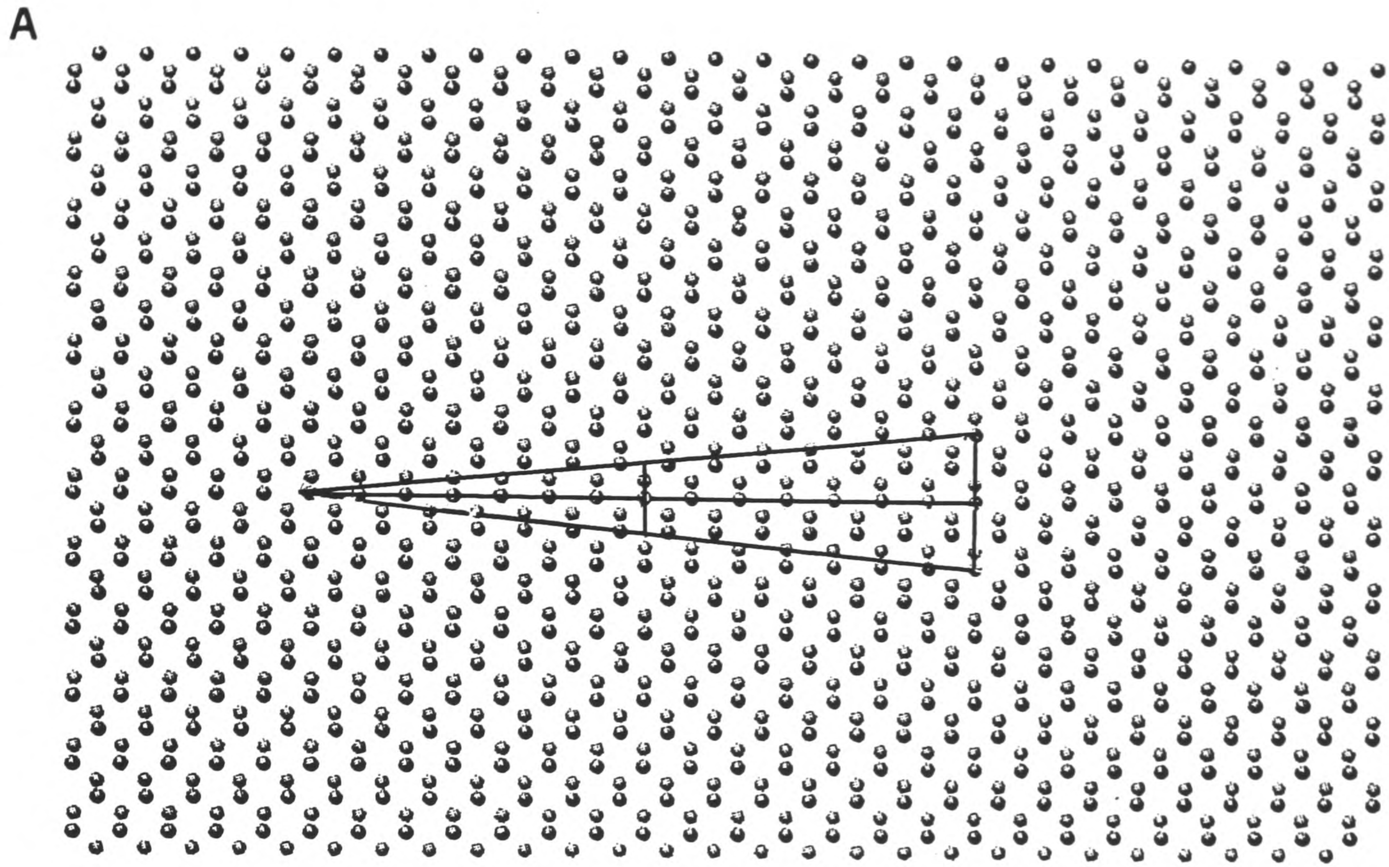

B

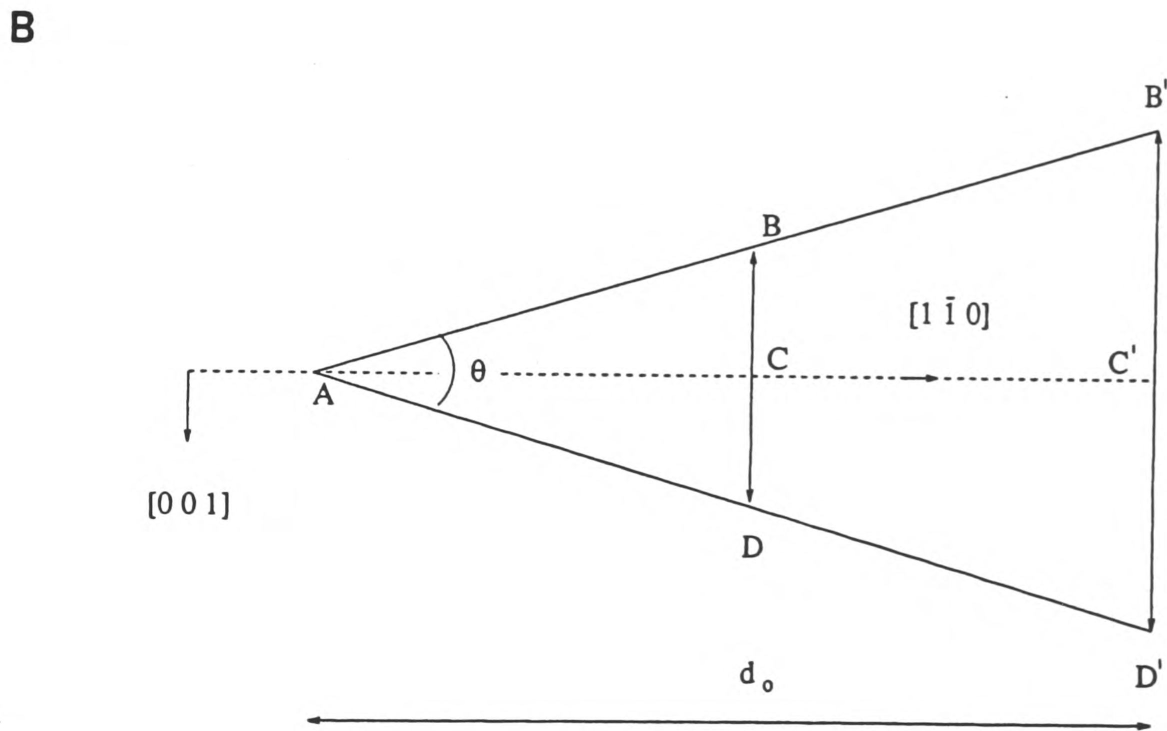

Figure 6.2: A) An illustration of the matching between the grain boundary periodicity and the supercell period along the boundary. B) Consider a grain boundary running along $[1\bar{1}0]$ as shown by line AC, generated by a set of $\mathbf{a}/2 < 110 >$ dislocations. Per period, the boundaries in the supercell contain a net Burgers vector of $\mathbf{b}$=$\mathbf{a}[001]$ and $\mathbf{b}$=$\mathbf{a}[00\bar{1}]$ respectively. The dislocations impart an equal and opposite displacement of $\mathbf{a}/2[001]$ in each boundary period to either grain, as shown at site C. From the triangle ABC or ADC, it is clear that a similar triangle of double the scale would have the vector B′C′ ending at another atom that is equivalent to the atom at site C.

6.1.2 The Atomic Relaxations

Two sets of relaxations were performed on the supercell generated in the previous section.

The first was a relaxation with the Tersoff potential carried out on the supercell, considering all atoms to be Si atoms. The potentials used were the Si Tersoff potentials. The supercell was annealed at 1300^0 K for several thousand time steps and subsequently quenched. It was found that the core spontaneously reconstructed in such a fashion as to lead to the doubling of periodicity along the dislocation line, i.e., bond reconstruction occurs along the dislocation line, similar to the reconstruction known to take place in the 30^0 partial in Si. In a perfect crystal the periodicity along [110] is 1/2[110]. It is therefore essential in the defect-containing supercell to double the cell height to [110] along the dislocation line. Consequently the number of atoms in the unit cell for the 60^0 dislocation must be considerably greater than considered in the [001] dislocation where the periodicity along the dislocation line remained 1/2[110], as in a perfect diamond lattice. The supercell used here contained 672 atoms.

The Tersoff relaxed core consists of a 7-membered ring with a 5-membered ring attached to it. The tetra-coordination of all atoms is satisfied, leaving no dangling bonds. There are two atoms in the core that bond along the dislocation line. This bond is stretched by only 3% over the normal bond length. Table 6.4 gives the maximum and minimum distortions that occur in the bond lengths and bond angles of the reconstructed core. There are rather large deviations in the bond angles from the ideal tetrahedral angle of 109^0. The effect this has on the electronic structure is of interest, however, it was not possible to carry out electronic structure calculations in this case.

Distortion	Tersoff Si	Tight Binding GaAs
Maximum bond stretch	3.1%	7.1%
Maximum bond compression	2.3%	6.6%
Maximum bond angle	147.98^0	150.80^0
Minimum bond angle	76.422^0	84.80^0

Table 6.4: Maximum and minimum distortions in the reconstructed perfect 60^0 dislocation core.

6.1.3 The Tight Binding Relaxation

A real space tight binding relaxation of the supercell was carried out using Chadi (1984) parameters. There is no qualitative difference in the core stucture from that obtained by Tersoff relaxation, except that we now treat the atoms in the supercell as Ga or As and are therefore able to comment on the formation of wrong bonds. The bond stretching and bond compression are compared with those obtained by Tersoff relaxation in Table 6.5, where the bonds are indexed as shown in Figure 6.3.

Minimising the number of wrong bonds in the system results in the bond between the two atoms lying at the joint of the 5- membered and 7-membered ring being a wrong bond. The As-As wrong bonds are longer and weaker than the Ga-Ga wrong bonds, consistent with the results obtained in Chapter 5 and with those obtained by Jones *et al.* (1993) from first principles using a local density approximation and working with cluster sizes of a maximum of 158 atoms.

6.2 Image simulation of the 60^0 Dislocation

The EMS package was used to generate a series of simulated images of the 60^0 dislocation at different thickness and defocal values using the same parameters as listed in Table 5.1, but now the image dimension 1024×1024. These images are shown in Figure 6.4, from which the image 'p', at a thickness of 200 Å and at Scherzer defocus,

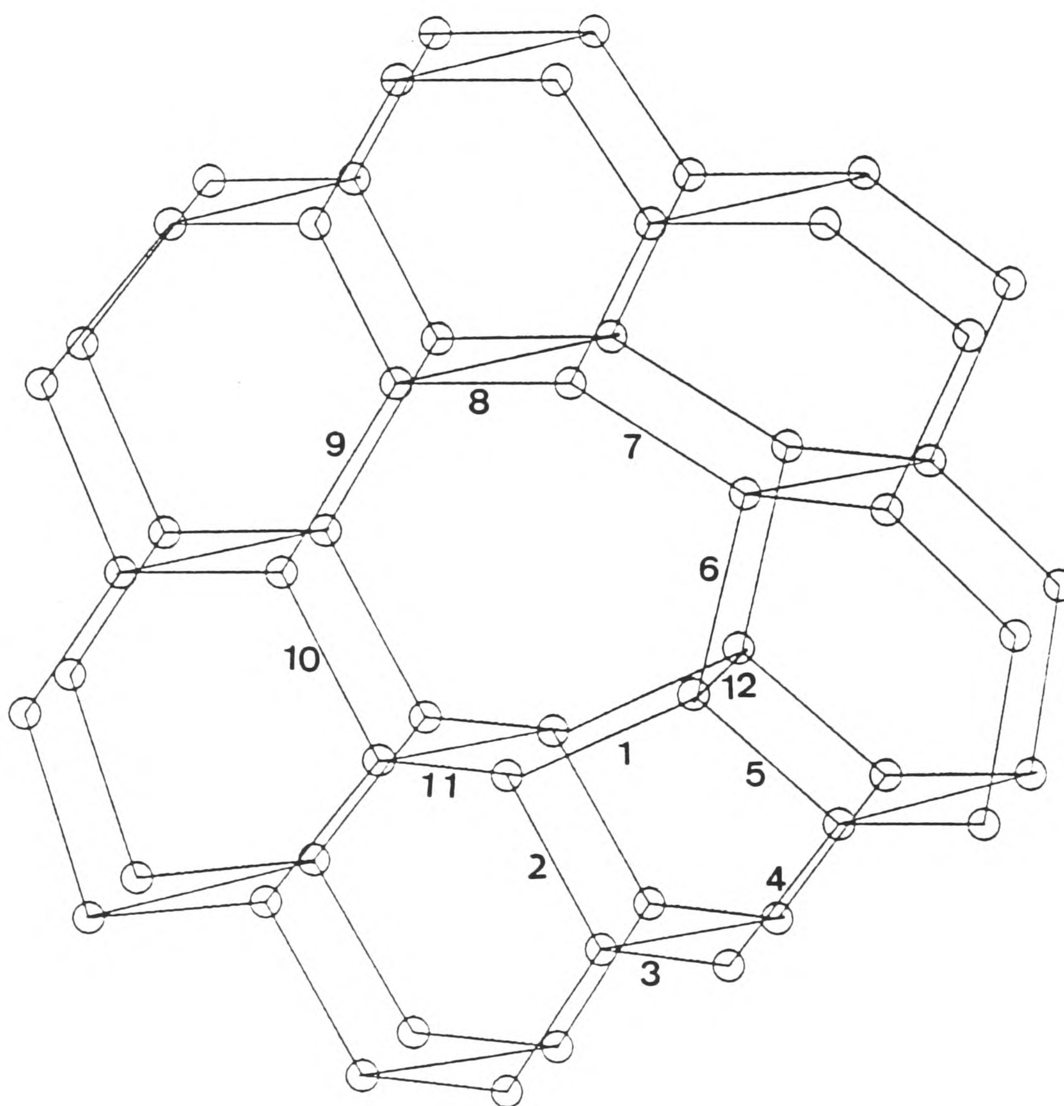

Figure 6.3: An illustration of the 60^0 core obtained by atomic relaxation, with bond indexing. Above is a schematic diagram showing bond index 12, along the dislocation line.

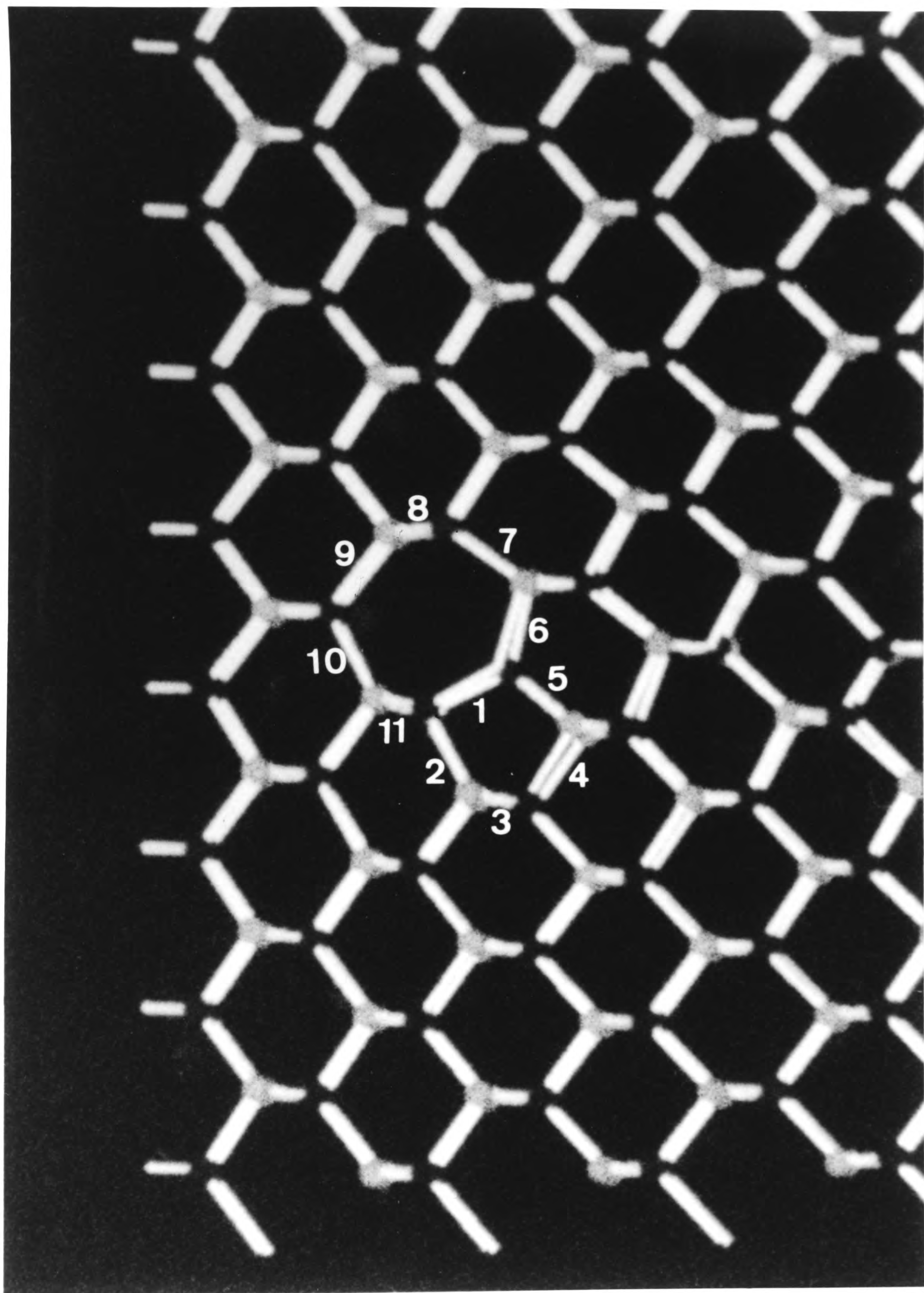
8
7
9
6
10
5
1
11
2
4
3

Bond Index	Tersoff Si	Tight Binding GaAs	Tight Binding GaAs
1	0.1	0.9 #	-6.1 *
2	-0.9	-2.1	5.2
3	-2.0	-3.1	-3.3
4	-3.1	-5.4	-5.2
5	-2.0	-4.8	7.1
6	-2.3	-0.7	-6.6
7	0.7	0.9	3.3
8	1.0	1.1	1.1
9	2.1	5.0	3.9
10	-0.2	0.5	1.7
11	-1.0	-2.5	-3.7
12	2.9	4.9 #	-3.8 *

Table 6.5: Comparative percentage bond distortions in relaxed core structures of perfect 60^0 dislocations obtained for different potentials. The two tight binding results are from the dislocation cores containing Ga-Ga and As-As wrong bonds respectively. * marks a Ga-Ga wrong bond and # an As-As wrong bond. Bond 12 is along the dislocation line.

was selected to compare with the experimentally obtained image produced in Chapter 4. This defocus and thickness are in agreement with the estimates made during comparisons of simulations and experimental images of the perfect crystal and the [001] dislocations. From the projected potential shown at the top left of Figure 6.4 it is determined that the atomic columns are imaged black and the tunnels are imaged white. One of the dislocation cores in the image 'p' is to be found boxed in the Transparency C (contained in the envelope at the back of the thesis). When the box is overlayed on the corresponding box C in Figure 5.2 it is seen that the two are in reasonable agreement.

Figure 6.4: A series of simulated images for the 672-atom supercell at varying thicknesses and defocii. The projected potential is shown at the top left.

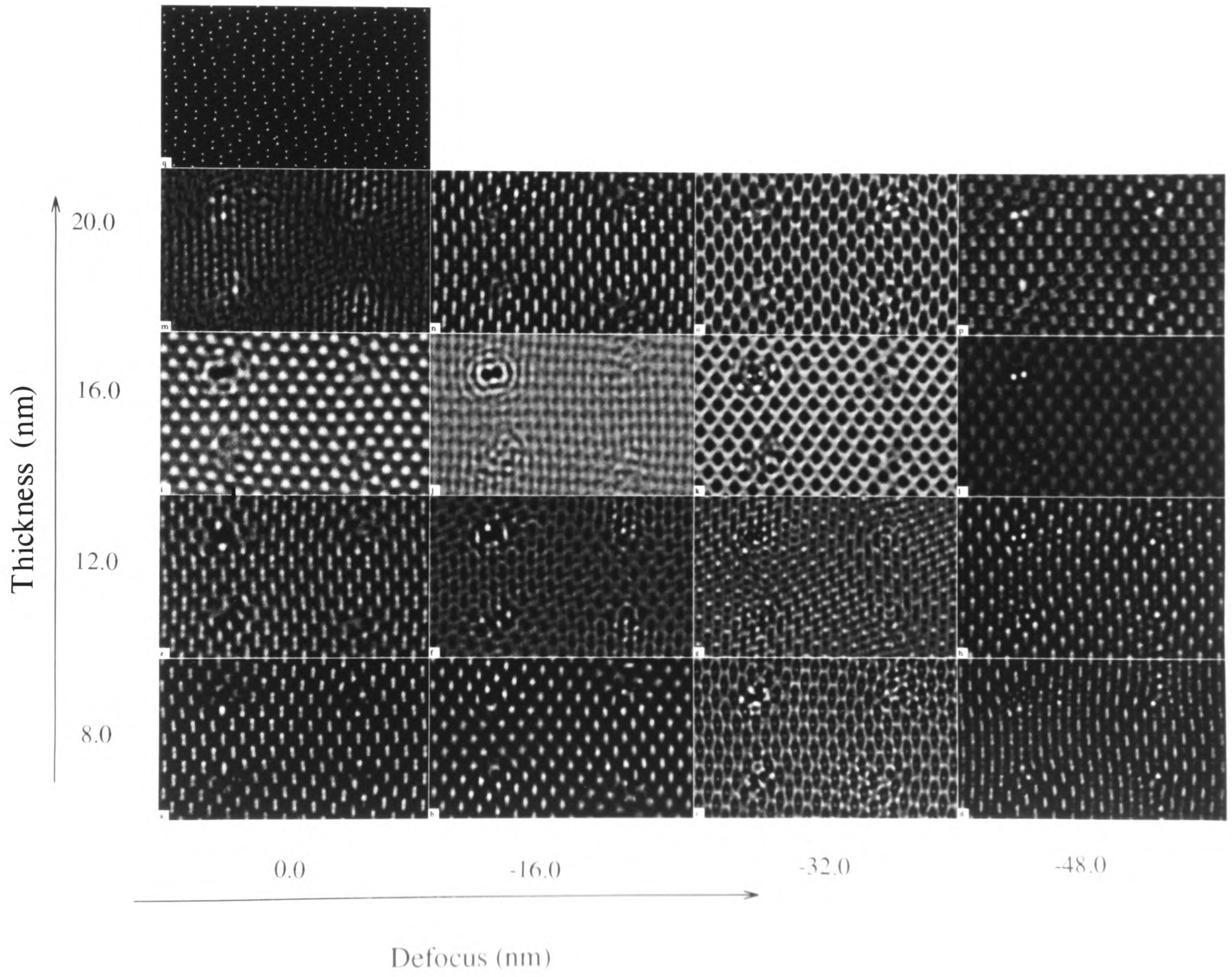

20.0
16.0
12.0
8.0
Thickness (nm)
0.0
-16.0
-32.0
-48.0
Defocus (nm)

6.3 Conclusion

From the work in this chapter it can be concluded that a physically reasonable atomic model for the core of a 60^0 perfect dislocation has been obtained. Due to the computational limitations the supercell constructed was not ideal in that the periodicity of the supercell did not match the periodicity of the grain boundary it contains. However, it is interesting to note the doubling of the period along the dislocation line is very similar in nature to the period doubling that occurs at the 30^0 partial in silicon. This is not surprising in view of the fact that the 60^0 perfect dislocation dissociates in the bulk into a 90^0 and a 30^0 partial.

Chapter 7

Other Experimental Work and Suggestions for the Future

7.1 Other Work

This chapter presents images of some grain boundaries in GaAs that have been obtained during the course of the search for an appropriate boundary to be studied in detail. All the images shown in this chapter are from specimens made from the same ingot used in Chapter 2. Each image resulted from a separate specimen. The specimen preparation was the same for all samples, apart from one specimen that was prepared by chemical jet polishing. This specimen was prepared as follows. A 3 mm sample was cut out ultrasonically. It was then mounted between two Si backing pieces, on a Pyrex disc using Crystal bond. The sample was then mechanically ground down using SiC papers until it was $\sim 70\mu$m thick. The SiC grinding damage was removed by a 6μm diamond polish. The sample was then dissolved off the Pyrex dish using dimethylformamide and stuck down onto a PTFE stub using Lacomit lacquer. An area around the edge of the sample was painted by Lacomit lacquer. The unmasked area of the sample was then chemically dished by rotating the PTFE stub and the sample under a jet of Cl_2/CH_3OH solution. After dishing, the plan view sample was chemically thinned to perforation by dipping in a Cl_2/CH_3OH solution. The perforated specimen was then

dissolved off the PTFE stub using acetone. After cleaning in acetone and methanol, the sample was then stuck onto a Cu TEM grid. The plan-view sample was then ready for TEM.

The analysis of a particular boundary, such as that carried out in Chapters 4, 5 and 6, needs to be done for every HREM image of good quality in order to extract the fullest information from it. However, due to limitations on time the images presented here have not been analysed thoroughly and they are available for anyone with sufficient interest in them for carrying out detailed work.

Figure 7.1A shows a twin boundary in GaAs and the corresponding diffraction pattern. It is a simple $\Sigma 3$ (111) boundary, the structure of which has been well understood in Si and Ge for a long time. In Figure 7.1B the structure of a twin band in an f.c.c. lattice is shown schematically. Since the $\{111\}$ plane in each grain is the boundary plane there are no dislocations and the boundary is of the highest coincidence possible. It can either be thought of as a 70.5^0 tilt boundary about [110], a 180^0 twist boundary about the boundary normal, [111], or as a shear in a $[11\bar{2}]$ direction. It would be of interest, however, to try to find out whether there are wrong bonds at the boundary, and if so, of what kind. Since wrong bonds are not thought to cost a great deal of energy in GaAs (Jones, 1981), a study to this effect would be worth undertaking. It is unlikely that HREM alone can be instrumental in determining this information, though with the aid of covergent beam electron microscopy an attempt might be made.

Figure 7.2 shows an HREM image of a 4^0 low angle grain boundary with arrows marking out some of the dislocation cores. The boundary is made up of $\mathbf{a}/2 < 110 >$ dislocations. These are the most frequently occurring dislocations in f.c.c. and diamond cubic structures. Figure 7.3 shows an HREM image of an 8^0 tilt boundary about [110], imaged edge on. Burgers vector analysis shows the existence of $\mathbf{a}/2 < 110 >$ dislocations.

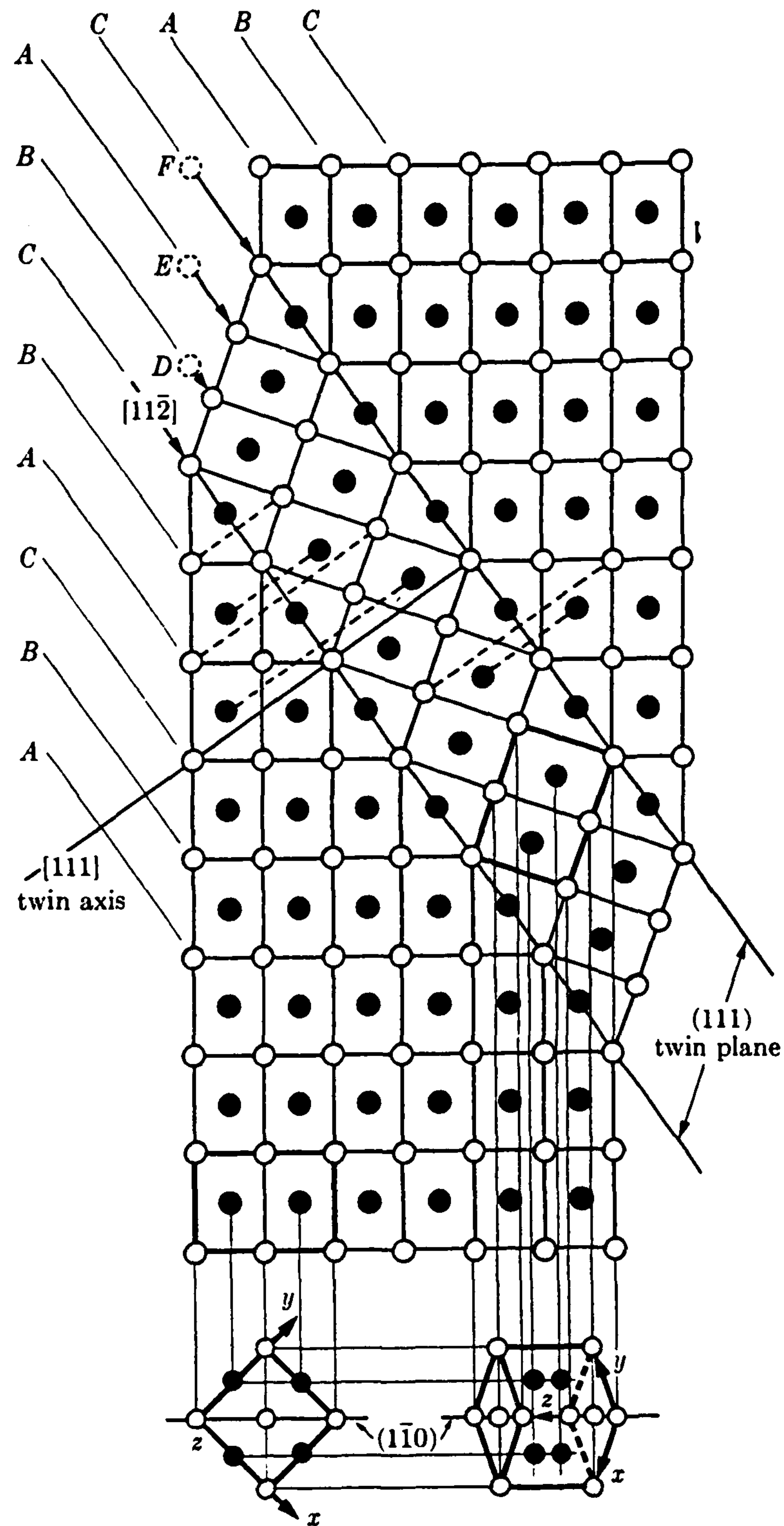

Figure 7.1: A) An HREM image of a twin boundary in GaAs and B) the [1$\bar{1}$0] projection of a twin boundary in an f.c.c. structure. Open circles represent atoms in the plane of the drawing and filled circles those in the layers immediately above or below. The reflection symmetry across the twin plane is suggested by the dashed lines connecting several pairs of atoms.

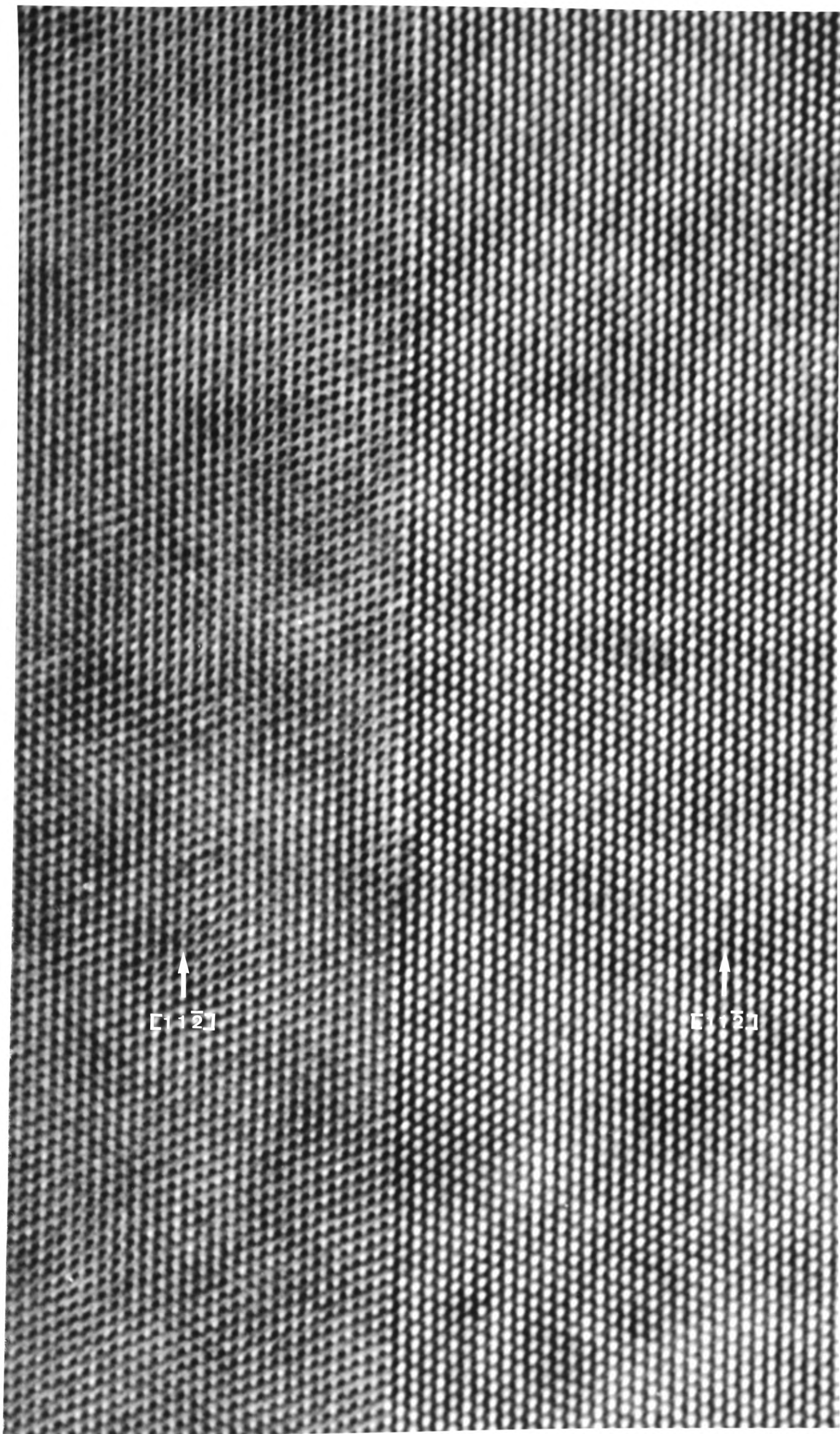
[1 1 $\bar{2}$]
[1 1 $\bar{2}$]

Figure 7.2: An HREM image of a 4^0 tilt boundary in GaAs about [110] with arrows marking some dislocation cores.

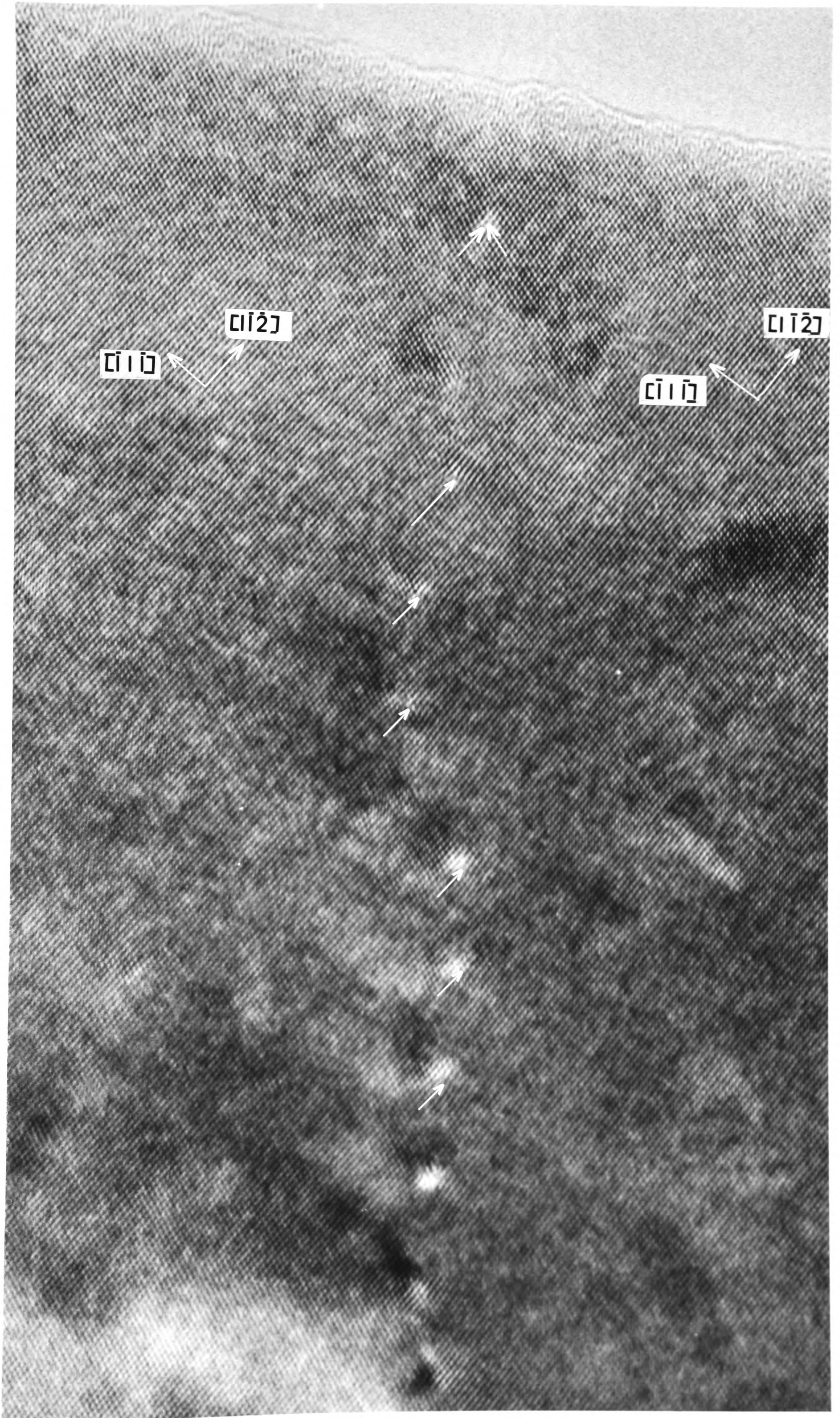

$[\bar{1}1\bar{1}]$
$[1\bar{1}\bar{2}]$
$[\bar{1}1\bar{1}]$
$[1\bar{1}\bar{2}]$

Figure 7.3: HREM imge of an 8^0 tilt boundary about [110] showing the presence of $\mathbf{a}/2 <110>$ dislocations.

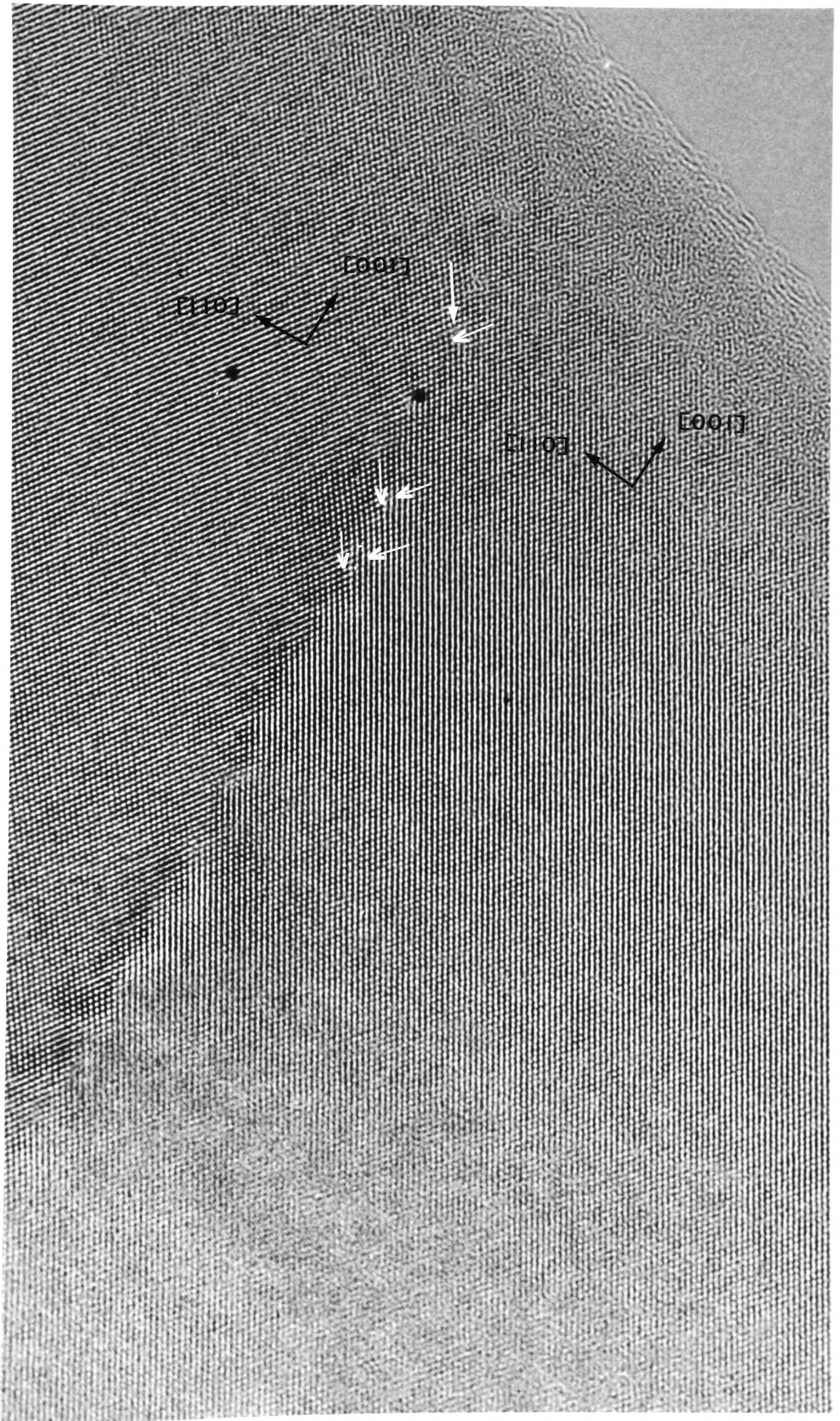

7.2 Suggestions for Further Work

- Tables 6.1, 6.2 and 6.3 are a good indication of work that remains to be done in the area of characterising the atomic and electronic states associated with dislocation cores. The distinction between dislocations in a boundary and those that occur in the bulk has not been considered while making the tables mentioned above, and that in itself is a major task and an important one. This would involve careful study of the same Burgers vector dislocations in the bulk and in a boundary, and would necessarily involve the three techniques used in this thesis, i.e., HREM imaging, atomistic relaxations and image simulations.

- The development of a BOP potential for GaAs such as the BOP potential for Si would go a long way towards predicting the qualitative structure of dislocation cores in this material. This is not an easy development and by its very nature involves a period of time to test the validity and limitations of the potential.

- Increased computational power would enable the semi-empirical tight binding analysis of the 60^0 dislocation to be carried out. At present a 672 atom supercell, resulting from period doubling along the dislcoation line, is much too large to be relaxed using a k-space approach. Had such a relaxation been possible knowledge of the localised electronic states (if any) could have been obtained.

- It would be of great interest to carry out electrical measurements at an [001] dislocation in a boundary to verify whether the predicted states in the band gap (see Figure 5.13) can be found. The difficulty in this lies in the fact that most of the data collected is across bulk specimens where knowledge of the density of point and extended defects is limited. Techniques such as the Hall effect, Photoluminescence and Deep Level Transient Spectroscopy (DLTS), have been

in use in this area of study. For a detailed account of the understanding of electrical activity associated with line defects in GaAs see Galloway (1994).

- There has been relatively little work done in the area of asymmetric boundaries. This is because the geometry is more complicated, and not due to less frequent occurrence of them. Twist boundaries too are more rarely reported.

- The questions of mobility of dislocations, grain boundary migration and the preference of glide or shuffle configurations are still open, with much to be yet understood.

- Variations of the iterative-structure refinement procedure carried out in this work to obtain the 'experimental-best-fit' structure will certainly be useful. The dependence of contrast features observed on different sets of planes would also be useful. If variations lead to physically plausible alternative core structures perhaps some insight could be obtained.

7.3 Closing Remarks

In the final analysis, the work reported in this thesis has led to plausible dislocation core structures for the [001] and 60^0 dislocations in GaAs. Electronic structure analysis revealed the presence of deep states associated with Ga-Ga wrong bond in the [001] disloction core. The work has also shown that matching of the simulated image to an HREM image is not proof of the structure on which the simulation is based, but it can distinguish between an artefact and a true contrast arising from structural changes.

The work has generated more questions than it has answered, but perhaps asking the right questions is more important than searching for answers to the irrelevant ones.

Appendix A

The Median Lattice

The concept of a Median Lattice was put forward by Frank (1950). It is an alternative coordinate frame in which grain boundaries are easier to study and classify, compared to choosing the coordinate frame of one crystal or the other. The median lattice is a crystal lattice with an orientation that is midway between the lattices of the two crystals meeting at a grain boundary.

Consider Figure A1a which shows a perfect median lattice. Suppose we now wish to create a grain boundary with the rotation axis perpendicular to the page, and of misorientation θ in the median lattice. If $\mathbf{n}_1$ and $\mathbf{n}_2$ be the surface normals to the boundary planes, the portion of the median lattice lying between the two boundary planes is simply removed, as can be seen from Figure A1b. The next step is to then rotate $\mathbf{n}_1$ and $\mathbf{n}_2$ in opposite sense by $\theta/2$ such that the two boundary planes come together as indicated by the arrows. The grain boundary has now been formed. Now, the mean boundary plane is given by:

$$\mathbf{N} = \mathbf{n}_1 + \mathbf{n}_2$$

On the basis of the median lattice symmetric tilt boundaries in cubic crystals must have the mean boundary plane as a mirror plane of the perfect crystal, whereas an asymmetric boundary cannot have a mean boundary plane that is a mirror plane of the perfect crystal.

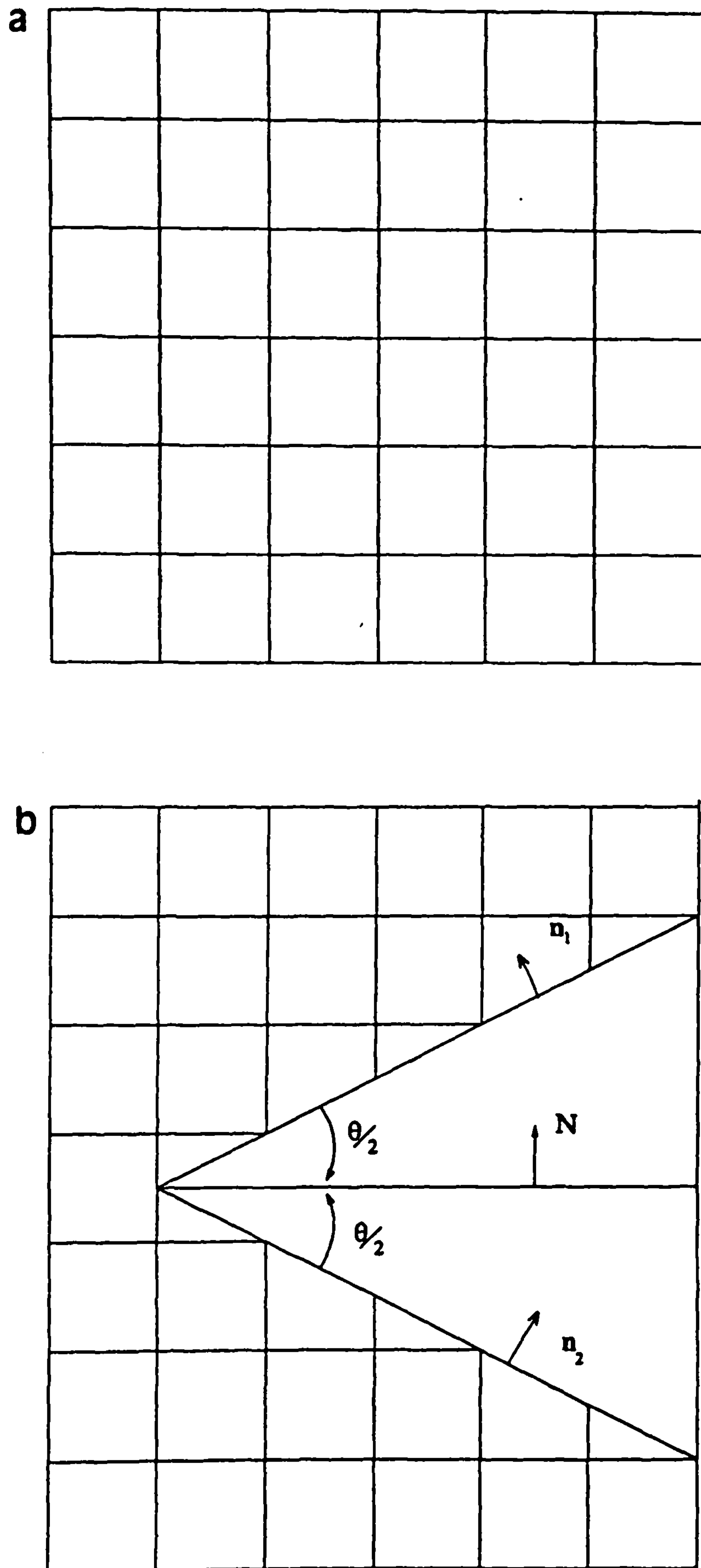

Figure A.1: a) The perfect median lattice in which a grain boundary is to be formed. b) Rotation of the surface normals about the rotation axis normal to the page. The normal to the mean boundary plane is **N**.

For example, say we wish to characterise a symmetric tilt boundary on a (hkl) plane. First, set $\mathbf{n}_1 = [hkl]$ and $\mathbf{n}_2 = [h\overline{kl}]$, which makes the mean boundary plane normal [100], which is a mirror plane. The tilt angle is given by:

$$\cos\theta = (h^2 - k^2 - l^2)/(h^2 + k^2 + l^2)$$

and the tilt axis is given by $\mathbf{n}_1 \times \mathbf{n}_2$, which is parallel to $[0\bar{l}k]$.

Appendix B

The Contrast Transfer Function

The effects of changes in objective lens parameters and illumination conditions on simple lattice fringes formed from diffracted beams is given here. Simple expressions are given to illustrate how the lattice fringes are affected by defocus, C_s and electronic instabilities. Consider an image formed by the central beam and a single Fourier component. Let the Bragg beam Φ_{hk0} (which is affected by the specimen orientation and thickness) be represented by:

$$\Phi_{hk0} = \phi_{hk0} \exp[i\epsilon]$$

then, the image is given by:

$$\Psi(x, y) = \sum \Phi_{hk0} \exp[-2\pi i(hx/a + ky/b)] \exp[i\chi(u_{h,k})]$$

where the sum is over all the beams in the objective aperture and a, b are the unit cell dimensions normal to the electron beam direction. Here, $\chi(u_{h,k})$ is the phase shift introduced by the instrumental abberations. In the absence of astigmatism this is given by:

$$\chi(u_{h,k}) = \frac{2\pi}{\lambda}[\frac{\Delta f \lambda^2 u_{h,k}^2}{2} + \frac{C_s \lambda^4 u_{h,k}^4}{4}]$$

where,

$$u_{h,k}^2 = \frac{h^2}{a^2} + \frac{k^2}{b^2}$$

For a cubic specimen, and the diffracted beam $(h,0,0)$ only, in the kinematic case $\epsilon = -\frac{\pi}{2}$, then from the two beams we obtain an image:

$$I(x) = \Psi_i(x)\Psi_i^*(x) = \phi_0^2 + \phi_h^2 + 2\phi_0\phi_h \sin\left[2\pi h\frac{x}{a} - \chi(u_h)\right]$$

Hence any changes in $\chi(u_h)$ produces a sideways movement in the fringe image.

For the case of 3 beams in the objective aperture, $(0,0,0), (h,0,0)$ and $(-h,0,0)$ the image intensity is given by:

$$I(x) = \phi_0 + \phi_h + \phi_{-h} + 4\phi_0\phi_h \cos(2\pi h\frac{x}{a})\cos[\chi(u_h) + \epsilon] + 2\phi_h\phi_{-h}\cos(4\pi h\frac{x}{a}).$$

For $\phi_h = \phi_{-h}$ and $\epsilon = \frac{-\pi}{2}$ there are cosine fringes with lattice spacing and weaker cosine fringes at half that spacing.

For a weak phase object the exit wave amplitude can be written as:

$$\Psi_e(x,y) = \exp\left[-i\sigma\phi_p(x,y)\right]$$

where σ is a constant and $\phi_p(-x,-y)$ is the projected specimen potential. The final image amplitude $\Psi_i(x,y)$ can be expressed as:

$$\begin{aligned}\Psi_i(x,y) &= [1 - i\sigma\phi_p(-x,-y)] * \mathcal{F}[P(u,v)\exp(i\chi(u,v))] \\ &= [1 - i\sigma\phi_p(-x,-y)] * [c(x,y) + is(x,y)]\end{aligned}$$

where, $c(x,y), s(x,y)$ are the Fourier transforms of the real and imaginary parts of $\exp(i\chi(u,v)$. $\chi(u,v)$ is an even function of (u,v) and represents the lens aberration phase shift, while $P(u,v)$ corresponds to the objective aperture pupil function. To a first order approximation:

$$\Psi_i(x,y) = 1 + [\sigma\phi_p(-x,-y)] * [s(x,y)] - i\sigma\phi_p(-x,-y) * [c(x,y)]$$

which results in an image intensity given by:

$$I = \Psi_i(x,y)\Psi_i^*(x,y) = 1 + 2\sigma\phi_p(-x,-y) * s(x,y).$$

This shows that the important factor is $\mathcal{F}[P(u,v)\sin(\chi(u,v))]$. If $\sin\chi(u,v) \approx 1$ over a large range (passband), then the image is the most simple one in that each point is simply smeared out by the aperture function, $P(u,v)$. This is the case at Scherzer defocus and hence it is that passband imaging is preferred.

In many beam images (HREM) it is difficult to write down such an expression. The projected charge density approximation, which assumes a flat Ewald sphere, can be used to obtain a relation between a specimen of known structure, thickness and orentation, and its image. No objective aperture or spherical aberration is considered here. The exit wave at the bottom of the specimen (assumed a phase object) is given by:

$$\Psi_e(x,y) = \exp(-i\sigma\phi_p(x,y))$$

where $\phi_p(x,y)$ is the projected specimen potential in volt nm. The back focal plane amplitude is given by the Fourier transform:

$$\Psi_d(u,v) = \mathcal{F}\{\exp(-i\sigma\phi_p(x,y))\}\exp(i\pi\Delta f\lambda(u^2+v^2)) = \Phi(u,v)[1 + i\pi\Delta f\lambda(u^2+v^2)]$$

The image amplitude at unit magnification and no rotation is given by the inverse tranform:

$$\Psi_i(x,y) = \exp(-i\sigma\phi_p(x,y)) + i\pi\Delta f\lambda\mathcal{F}^{-1}\{(u^2+v^2)\Phi(u,v)\}$$

The image intensity, to first order, is:

$$I(x,y) = 1 - \Delta f\lambda\frac{\sigma}{2\pi}\nabla^2\phi_p(x,y).$$

Using Poisson's equation $\nabla^2\phi_p(x,y) = -\rho_p(x,y)/\epsilon_0\epsilon$ we have:

$$I(x,y) \approx 1 + (\Delta f\lambda\frac{\sigma}{2\pi\epsilon_0\epsilon})\rho_p(x,y)$$

where $\rho_p(x,y)$ is the projected total charge density, including the nuclear contribution.

Effects of spherical abberation and limiting objective aperture have been included by various workers showing that within certain experimental conditions the high resolution image represents the specimen total charge density.

Appendix C

List of Input Parameters used in the Atomic Relaxations

C.1 The Tersoff Potential

The functional form as derived by Tersoff (1988) is as follows:

$$
\begin{aligned}
E &= \sum_i E_i = \frac{1}{2}\sum_{i\neq j} V_{ij} \\
V_{ij} &= f_c(r_{ij})[a_{ij} A \exp(-\lambda_1 r_{ij}) - b_{ij} B \exp(-\lambda_2 r_{ij})] \\
f_c(r) &= 1 \qquad\qquad\qquad\qquad r < R - D \\
&= \frac{1}{2} - \frac{1}{2}\sin[\frac{\pi}{2}\frac{r-R}{D}] \qquad R - D < r < R + D \\
&= 0 \qquad\qquad\qquad\qquad r > R + D \\
b_{ij} &= (1 + \beta^n \zeta_{ij}^n)^{\frac{-1}{2n}} \\
a_{ij} &= (1 + \alpha^n \eta_{ij}^n)^{\frac{-1}{2n}} \\
\zeta_{ij} &= \sum_{k(\neq i,j)} f_c(r_{ik}) g(\theta_{jik}) \exp[\lambda_3^3 (r_{ij} - r_{ik})^3] \\
\eta_{ij} &= \sum_{k(\neq i,j)} f_c(r_{ik}) g(\theta_{jik}) \exp[\lambda_3^3 (r_{ij} - r_{ik})^3] \\
g(\theta) &= 1 + \frac{c^2}{d^2} - \frac{c^2}{d^2 + (h - \cos\theta)^2}
\end{aligned}
$$

where i, j and k refer to atoms in the system, r_{ij} is the length of the bond between atoms i and j, and θ_{jik} is the angle between bonds ij and ik.

Parameter	Value
A (eV)	1.8308X10^3
B (eV)	4.7118X10^2
λ_1	2.4799 $\AA^{-1}$
λ_1	1.7322 $\AA^{-1}$
α	0.0
β	1.0999$\times$10^{-6}
η	7.8734$\times$10^{-1}
c	1.0039$\times$10^5
d	16.218
h	-0.59826
λ_3	1.7322 Å$-$1
R	2.85 Å
D	0.15 Å

Table C.1: Parameter set used for Tersoff (1988) potential for Si.

C.2 The Bond Order Potential

The method is based on the tight binding bond model with use of Greens function G in representing the bond energy (E_{cov} in Chapter 3) as a sum over the bonds themselves. Angular character of atomic orbitals shows up in the dependence of bond energy on the orientation and local environment of the bonds.

From the tight binding bond model (Sutton *et al.*,1988) we have:

$$U_{bond} = \frac{1}{2}\sum_{i\alpha}\int^{E_F} 2(E - E_{i\alpha})\eta_{i\alpha}(E)dE$$

where $\eta_{i\alpha}(E)$ is the density of states given by:

$$\eta_{i\alpha}(E) = \sum_{\nu} |a^{\nu}_{i\alpha}|^2\delta(E - E_{\nu})$$

where $|a_{i\alpha}^{\nu}|^2$ is the weight that the atomic state $i\alpha$ has on a particular bond orbital ν. $\eta_{i\alpha}(E)$ is related to the moments by the simple relation:

$$\mu_{i\alpha}^{(p)} = \int [E^p \eta_{i\alpha}(E)] dE.$$

The shape of the density of states curve is characterised by the moments as follows:

$\mu_{i\alpha}^{(1)}$ gives the centre of gravity of the curve.

$\mu_{i\alpha}^{(2)}$ gives the width of the curve.

$\mu_{i\alpha}^{(3)}$ relates to the skewness of the curve.

$\cdots$ and so on. Also,

$$\mu_{i\alpha}^{(p)} = < i\alpha | H^p | i\alpha > .$$

i.e. the p'th moment $\mu_{i\alpha}^{(p)}$, of the Hamiltonian is related to the density of states. This allows us to calculate $\mu_{i\alpha}^{(p)}$ and can be interpreted as hopping around the lattice.

The Hamiltonian is parameterised using the GPS values (Goodwin *et al.*, 1989) and the scaling law used is that shown in Chapter 3 with a cut off at 3.2 Å.

Such use of moments provide qualitative insight into the effect of local connectivity on electronic structure only. For a quantitative understanding a recursion scheme is used. The density of states is evaluated from the recursion coefficients by using the Green's function $G = (E - H)^{-1}$. The recursion coefficients are directly related to the moments. There is another way of expressing the bond energy, as:

$$U_{bond} = \frac{1}{2N} \sum_{i,j} U_{bond}^{ij} = \frac{1}{2N} \sum_{i\alpha j\beta, i \neq j} 2 H_{i\alpha j\beta} \Theta_{j\beta i\alpha}$$

where Θ is the bond order matrix or density matrix. It gives the difference between the number of electrons in the bonding N^+ and anti-bonding N^- states and can be written as:

$$\Theta_{ij}(E_F) = \frac{1}{2}[N^+ - N^-].$$

If $|u_0^\pm>$ represents the bonding (+) or anti-bonding (-) state:

$$|u_0^\pm> = \frac{1}{\sqrt{2}}[|i\alpha> \pm |j\beta>]$$

then, the number of electrons in these states can be found as follows:

$$\begin{aligned} N^+ &= 2\int^{E_f} \eta_{bonding}(E)dE = \frac{-2}{\pi}\Im\{\int^{E_F} < u^+|G(E+i0^+)|u^+ > dE\} \\ N^- &= 2\int^{E_f} \eta_{anti-bonding}(E)dE = \frac{-2}{\pi}\Im\{\int^{E_F} < u^-|G(E+i0^+)|u^- > dE\} \end{aligned}$$

where $\Im$ denotes the imaginary part, and hence

$$\Theta_{i\alpha j\beta} = -\frac{2}{\pi}\Im\{\int^{E_F} < i\alpha|G(E+i0^+)|j\beta > dE\}.$$

This has been generalised (Horsfield, 1995) to a representation as a potential as follows:

$$\Theta_{i\alpha j\beta} = \sum_{p=0}^{\infty} \frac{\delta N^{i\alpha}}{\delta \mu^{(p)}} \zeta_{p+1}^{i\alpha j\beta}$$

where,

$$\begin{aligned} \zeta_{p+1}^{i\alpha j\beta} &= < i\alpha|H^p|j\beta > \\ \mu^{(p)} &= < i\alpha|H^p|i\alpha > \\ N^{i\alpha} &= \int[\eta_{i\alpha}(E)]dE. \end{aligned}$$

standard	
4	number of orbitals
5.649	cubic constant
Gallium	Atom Name
0	Identifier
-2.657	E_s
3.669	E_p
0.00	spin correlation
3.00	number of electrons
Arsenic	
1	
-8.343	
1.041	
0.00	
5.00	
2	number of interaction sets
1	number of pairs sharing this interaction
0 1	atom(i) atom(j)
2.4465	r zero
-1.613	hss sigma
2.504	hsp sigma Ga(s)-As(p)
1.940	hsp sigma Ga(p)-As(s)
3.028	hpp sigma
-0.781	hpp pi
2	
0 0	
1 1	
2.4465	
-1.613	
2.232	
2.232	
3.028	
-0.781	
1	number of pair potentials
4.04974987248088d0, 0.0d0, 0.0d0	U1,U2, U3

Table C.2: Parameters used for GaAs tight-binding.

Appendix D

The 336-atom Supercell

ATOM NUMBER	TYPE	X	Y	Z
1	Ga	0.4375878	1.8708140E-02	0.8750054
2	Ga	0.4435886	9.0251714E-02	0.8746272
3	Ga	0.4496298	0.1622743	0.8739870
4	Ga	0.4556915	0.2350198	0.8728030
5	Ga	0.4614802	0.3088239	0.8704334
6	Ga	0.4657532	0.3840321	0.8653831
7	Ga	0.4560523	0.4567870	0.8442551
8	Ga	0.4216144	0.5251988	0.8403705
9	Ga	0.4106773	0.5967167	0.8581155
10	Ga	0.4098518	0.6663903	0.8700894
11	Ga	0.4135846	0.7360800	0.8739551
12	Ga	0.4192797	0.8061574	0.8751275
13	Ga	0.4254348	0.8766527	0.8753468
14	Ga	0.4315588	0.9475174	0.8752440
15	As	0.4822460	5.4095179E-02	0.8749112
16	As	0.4879710	0.1259083	0.8745134
17	As	0.4936991	0.1983757	0.8738980
18	As	0.4994371	0.2718692	0.8728829
19	As	0.5050305	0.3469828	0.8710089
20	As	0.5114247	0.4241404	0.8646952
21	As	0.4807866	0.4987603	0.8210452
22	As	0.4525333	0.5630325	0.8499919
23	As	0.4508718	0.6323091	0.8692308
24	As	0.4538456	0.7014535	0.8737860
25	As	0.4589504	0.7709984	0.8752099

ATOM NUMBER	TYPE	X	Y	Z
26	As	0.4647777	0.8411160	0.8754930
27	As	0.4706745	0.9117231	0.8754019
28	As	0.4764948	0.9827257	0.8751923
29	Ga	0.6040595	1.8740356E-02	0.8752071
30	Ga	0.6092576	9.0202600E-02	0.8749831
31	Ga	0.6144204	0.1621208	0.8748385
32	Ga	0.6197367	0.2346763	0.8749849
33	Ga	0.6259079	0.3080942	0.8761060
34	Ga	0.6358341	0.3822957	0.8802302
35	Ga	0.6598870	0.4548998	0.8972024
36	Ga	0.5765781	0.5225883	0.9525871
37	Ga	0.5680142	0.5992792	0.8780946
38	Ga	0.5753438	0.6686398	0.8777566
39	Ga	0.5819644	0.7375039	0.8769673
40	Ga	0.5879019	0.8069029	0.8763182
41	Ga	0.5934328	0.8770055	0.8758348
42	Ga	0.5987918	0.9476614	0.8754802
43	As	0.6483523	5.3985238E-02	0.8751673
44	As	0.6532627	0.1256100	0.8750524
45	As	0.6581665	0.1976866	0.8752335
46	As	0.6635209	0.2703334	0.8763244
47	As	0.6710306	0.3433993	0.8800561
48	As	0.6874512	0.4150990	0.8910427
49	As	0.7209539	0.4852292	0.9038390
50	As	0.6036881	0.5640565	0.9148605
51	As	0.6134903	0.6334550	0.8828946
52	As	0.6215599	0.7023628	0.8790806
53	As	0.6278251	0.7715357	0.8772868
54	As	0.6332002	0.8413827	0.8763244
55	As	0.6383171	0.9118278	0.8757591
56	As	0.6433622	0.9827251	0.8754027
57	Ga	0.7706944	1.8039286E-02	0.8753543
58	Ga	0.7754117	8.9173585E-02	0.8752062
59	Ga	0.7801118	0.1602759	0.8753259
60	Ga	0.7850929	0.2312661	0.8761542
61	Ga	0.7914742	0.3019911	0.8789692
62	Ga	0.8020424	0.3721370	0.8870037
63	Ga	0.8220893	0.4425532	0.8997368
64	Ga	0.7058101	0.5263835	0.9167199
65	Ga	0.7294137	0.5969552	0.8976845

ATOM NUMBER	TYPE	X	Y	Z
66	Ga	0.7426575	0.6653948	0.8848591
67	Ga	0.7508093	0.7348276	0.8797011
68	Ga	0.7563781	0.8051560	0.8773909
69	Ga	0.7612234	0.8759318	0.8762671
70	Ga	0.7659537	0.9469338	0.8756790
71	As	0.8149444	5.3110003E-02	0.8752641
72	As	0.8196838	0.1241410	0.8752136
73	As	0.8245270	0.1949815	0.8755656
74	As	0.8300636	0.2654337	0.8770291
75	As	0.8380077	0.3351419	0.8814796
76	As	0.8506367	0.4041853	0.8931151
77	As	0.8732819	0.4745896	0.9077467
78	As	0.7579620	0.5585459	0.9047055
79	As	0.7792919	0.6286234	0.8914792
80	As	0.7897103	0.6984121	0.8823756
81	As	0.7958921	0.7689530	0.8785659
82	As	0.8008026	0.8398360	0.8768225
83	As	0.8054806	0.9108855	0.8759629
84	As	0.8101961	0.9820001	0.8755075
85	Ga	0.9375204	1.7311513E-02	0.8753002
86	Ga	0.9425555	8.8224590E-02	0.8750740
87	Ga	0.9476430	0.1587080	0.8749638
88	Ga	0.9529145	0.2286281	0.8751436
89	Ga	0.9587952	0.2979473	0.8761613
90	Ga	0.9659082	0.3671710	0.8795487
91	Ga	0.9756230	0.4382356	0.9027028
92	Ga	0.8587162	0.5154354	0.9057941
93	Ga	0.8940001	0.5856341	0.8971547
94	Ga	0.9105553	0.6570253	0.8847662
95	Ga	0.9176459	0.7299284	0.8796026
96	Ga	0.9228389	0.8024400	0.8773147
97	Ga	0.9276643	0.8744541	0.8762195
98	Ga	0.9325429	0.9460537	0.8756429
99	As	0.9820634	5.2357227E-02	0.8751075
100	As	0.9873923	0.1230244	0.8748479
101	As	0.9928240	0.1931567	0.8746135
102	As	0.9984378	0.2626423	0.8744927
103	As	4.2360504E-03	0.3317162	0.8747802
104	As	1.0097881E-02	0.4014723	0.8782676
105	As	3.0995774E-04	0.4829345	0.9380481

ATOM NUMBER	TYPE	X	Y	Z
106	As	0.9242748	0.5465860	0.9062862
107	As	0.9469402	0.6181834	0.8867707
108	As	0.9555560	0.6921701	0.8805038
109	As	0.9613414	0.7654368	0.8777759
110	As	0.9665049	0.8379276	0.8764845
111	As	0.9716175	0.9098201	0.8758067
112	As	0.9768029	0.9812756	0.8754013
113	Ga	0.1043534	1.7281085E-02	0.8750995
114	Ga	0.1101581	8.8277936E-02	0.8747252
115	Ga	0.1160011	0.1588611	0.8741434
116	Ga	0.1216746	0.2289100	0.8730869
117	Ga	0.1263807	0.2982501	0.8709148
118	Ga	0.1286595	0.3669004	0.8657793
119	Ga	0.1277853	0.4348198	0.8385227
120	Ga	0.1039025	0.4988801	0.8144525
121	Ga	7.4070461E-02	0.5768574	0.8770694
122	Ga	7.6723978E-02	0.6533123	0.8769869
123	Ga	8.1821196E-02	0.7281472	0.8765256
124	Ga	8.7279141E-02	0.8016107	0.8760962
125	Ga	9.2908651E-02	0.8740870	0.8757222
126	Ga	9.8607786E-02	0.9459085	0.8754042
127	As	0.1492538	5.2464962E-02	0.8748549
128	As	0.1553417	0.1233029	0.8743259
129	As	0.1614309	0.1937314	0.8733521
130	As	0.1670338	0.2636496	0.8713499
131	As	0.1705901	0.3329314	0.8667623
132	As	0.1706221	0.4013031	0.8529112
133	As	0.1586557	0.4723133	0.8292828
134	As	0.1272997	0.5452699	0.8528843
135	As	0.1167102	0.6161410	0.8721529
136	As	0.1199418	0.6910064	0.8748375
137	As	0.1253396	0.7648631	0.8755720
138	As	0.1312524	0.8376633	0.8756175
139	As	0.1372521	0.9097198	0.8754405
140	As	0.1432408	0.9812774	0.8751895
141	Ga	0.2710559	1.7978013E-02	0.8749520
142	Ga	0.2773480	8.9282870E-02	0.8745014
143	Ga	0.2836872	0.1606079	0.8736540
144	Ga	0.2898123	0.2319760	0.8719157
145	Ga	0.2947073	0.3033103	0.8680784

ATOM NUMBER	TYPE	X	Y	Z
146	Ga	0.2950929	0.3739565	0.8591524
147	Ga	0.2847299	0.4439926	0.8470008
148	Ga	0.2652307	0.5162337	0.8471780
149	Ga	0.2481547	0.5876680	0.8586656
150	Ga	0.2434327	0.6594062	0.8693016
151	Ga	0.2465285	0.7316086	0.8736081
152	Ga	0.2521828	0.8035641	0.8749822
153	Ga	0.2584640	0.8752069	0.8752821
154	Ga	0.2647844	0.9466435	0.8752041
155	As	0.3160280	5.3332150E-02	0.8747554
156	As	0.3223391	0.1247335	0.8741525
157	As	0.3286574	0.1962947	0.8729688
158	As	0.3345195	0.2680995	0.8704596
159	As	0.3384595	0.3400714	0.8648372
160	As	0.3340928	0.4116553	0.8535715
161	As	0.3155016	0.4825997	0.8462371
162	As	0.2957490	0.5548825	0.8517002
163	As	0.2862844	0.6252810	0.8635771
164	As	0.2862643	0.6962915	0.8714252
165	As	0.2910037	0.7678161	0.8742877
166	As	0.2971191	0.8392984	0.8751249
167	As	0.3034699	0.9106789	0.8752395
168	As	0.3097654	0.9820036	0.8750852
169	Ga	0.3574592	5.4092377E-02	0.1247664
170	Ga	0.3637335	0.1256696	0.1241827
171	Ga	0.3700254	0.1975910	0.1230527
172	Ga	0.3759422	0.2699833	0.1206887
173	Ga	0.3800964	0.3427896	0.1154606
174	Ga	0.3758702	0.4144566	0.1038095
175	Ga	0.3564958	0.4839832	9.5634781E-02
176	Ga	0.3360739	0.5567349	0.1010894
177	Ga	0.3274621	0.6278528	0.1136314
178	Ga	0.3277391	0.6985828	0.1215378
179	Ga	0.3324646	0.7694780	0.1243317
180	Ga	0.3385855	0.8404639	0.1251416
181	Ga	0.3449379	0.9115440	0.1252467
182	Ga	0.3512222	0.9827414	0.1250907
183	As	0.3961509	1.8074483E-02	0.1249797
184	As	0.4022377	8.9574039E-02	0.1245785
185	As	0.4083590	0.1614384	0.1238657

ATOM NUMBER	TYPE	X	Y	Z
186	As	0.4144229	0.2338687	0.1224866
187	As	0.4199385	0.3070774	0.1196104
188	As	0.4229392	0.3810377	0.1133422
189	As	0.4129345	0.4529271	9.5961250E-02
190	As	0.3823698	0.5233268	9.3152136E-02
191	As	0.3709148	0.5943139	0.10.1235716
192	As	0.3688428	0.6642140	0.1191362
193	As	0.3720993	0.7343577	0.1235716
194	As	0.3776961	0.8049253	0.1249790
195	As	0.3838654	0.8757651	0.1252870
196	As	0.3900466	0.9468195	0.1252152
197	Ga	0.5236280	5.4552048E-02	0.1249571
198	Ga	0.5292367	0.1263512	0.1246134
199	Ga	0.5348892	0.1988149	0.1241509
200	Ga	0.5407385	0.2722986	0.1235422
201	Ga	0.5472071	0.3473142	0.1228140
202	Ga	0.5568086	0.4243431	0.1226127
203	Ga	0.6104288	0.5034326	0.1855475
204	Ga	0.4921963	0.5600277	9.9756710E-02
205	Ga	0.4908786	0.6328897	0.1213874
206	Ga	0.4950303	0.7025382	0.1246889
207	Ga	0.5005629	0.7719523	0.1255712
208	Ga	0.5064484	0.8418515	0.1256370
209	Ga	0.5122763	0.9123054	0.1254633
210	Ga	0.5179921	0.9832224	0.1252287
211	As	0.5626028	1.8449485E-02	0.1251692
212	As	0.5679178	9.0001881E-02	0.1249197
213	As	0.5731794	0.1620999	0.1246897
214	As	0.5785030	0.2350045	0.1246068
215	As	0.5843387	0.3091297	0.1251138
216	As	0.5927996	0.3847429	0.1275591
217	As	0.6170017	0.4562742	0.1466113
218	As	0.5082871	0.5133835	6.2979601E-02
219	As	0.5294725	0.5974850	0.1221680
220	As	0.5346811	0.6676546	0.1261749
221	As	0.5404772	0.7369177	0.1263403
222	As	0.5461876	0.8064799	0.1260690
223	As	0.5517535	0.8766390	0.1257335
224	As	0.5572175	0.9473261	0.1254328
225	Ga	0.6897902	5.4075181E-02	0.1251996

ATOM NUMBER	TYPE	X	Y	Z
226	Ga	0.6946264	0.1254994	0.1251155
227	Ga	0.6994975	0.1971808	0.1253825
228	Ga	0.7049547	0.2691483	0.1266901
229	Ga	0.7128932	0.3412391	0.1309478
230	Ga	0.7292626	0.4127027	0.1418009
231	Ga	0.7611392	0.4839134	0.1536515
232	Ga	0.6420399	0.5671222	0.1629281
233	Ga	0.6537843	0.6342890	0.1349785
234	Ga	0.6628835	0.7023662	0.1299195
235	Ga	0.6695077	0.7714334	0.1276218
236	Ga	0.6749023	0.8414000	0.1264571
237	Ga	0.6799389	0.9119521	0.1258143
238	Ga	0.6848889	0.9828817	0.1254327
239	As	0.7291884	1.7986506E-02	0.1253438
240	As	0.7339319	8.9248776E-02	0.1251955
241	As	0.7386360	0.1606597	0.1253097
242	As	0.7435853	0.2321786	0.1261325
243	As	0.7499074	0.3036106	0.1289598
244	As	0.7609859	0.3741886	0.1368433
245	As	0.7823885	0.4439591	0.1489276
246	As	0.6678575	0.5292097	0.1705082
247	As	0.6903933	0.5990400	0.1477403
248	As	0.7015542	0.6668527	0.1340471
249	As	0.7092292	0.7358026	0.1293831
250	As	0.7147354	0.8056384	0.1272707
251	As	0.7196208	0.8760765	0.1262215
252	As	0.7244051	0.9469049	0.1256602
253	Ga	0.8564842	5.3144574E-02	0.1252485
254	Ga	0.8612676	0.1240097	0.1251729
255	Ga	0.8661535	0.1945303	0.1254532
256	Ga	0.8716560	0.2645412	0.1267138
257	Ga	0.8791347	0.3338892	0.1306530
258	Ga	0.8900815	0.4027049	0.1429852
259	Ga	0.9119561	0.4738273	0.1606753
260	Ga	0.7972219	0.5568233	0.1537676
261	Ga	0.8200430	0.6263983	0.1414177
262	Ga	0.8312173	0.6967182	0.1323998
263	Ga	0.8374133	0.7680172	0.1285649
264	Ga	0.8423082	0.8394434	0.1268161
265	Ga	0.8469808	0.9108081	0.1259568

ATOM NUMBER	TYPE	X	Y	Z
266	Ga	0.8517076	0.9820548	0.1255000
267	As	0.8959913	1.7148435E-02	0.1253289
268	As	0.9009391	8.8091493E-02	0.1251280
269	As	0.9059482	0.1586812	0.1250956
270	As	0.9112354	0.2287337	0.1254832
271	As	0.9174893	0.2980295	0.1270261
272	As	0.9257413	0.3666463	0.1316440
273	As	0.9363192	0.4351515	0.1517296
274	As	0.8185010	0.5168502	0.1551571
275	As	0.8525850	0.5879289	0.1473735
276	As	0.8688840	0.6591934	0.1355342
277	As	0.8762078	0.7311031	0.1299240
278	As	0.8814720	0.8029459	0.1274489
279	As	0.8862733	0.8745626	0.1262774
280	As	0.8910906	0.9459597	0.1256730
281	Ga	2.3643531E-02	5.2699298E-02	0.1250582
282	Ga	2.9078506E-02	0.1233923	0.1247433
283	Ga	3.4549084E-02	0.1935526	0.1243578
284	Ga	3.9936278E-02	0.2630795	0.1238525
285	Ga	4.4902265E-02	0.3321893	0.1231714
286	Ga	4.8764866E-02	0.4020097	0.1221493
287	Ga	6.8720661E-02	0.4791101	4.4517972E-02
288	Ga	0.9661702	0.5419685	0.1578809
289	Ga	0.9896536	0.6156670	0.1345481
290	Ga	0.9970955	0.6911529	0.1295959
291	Ga	2.6065232E-03	0.7651033	0.1274144
292	Ga	7.7702529E-03	0.8379468	0.1263389
293	Ga	1.2971532E-02	0.9100248	0.1257434
294	Ga	1.8268006E-02	0.9815731	0.1253625
295	As	6.2846728E-02	1.6777635E-02	0.1251401
296	As	6.8539731E-02	8.7690622E-02	0.1247926
297	As	7.4305385E-02	0.1581307	0.1242968
298	As	8.0028988E-02	0.2280009	0.1234604
299	As	8.5142642E-02	0.2973357	0.1218306
300	As	8.8413887E-02	0.3667379	0.1180875
301	As	8.9463554E-02	0.4369478	8.7670274E-02
302	As	0.9762906	0.4984589	0.1812582
303	As	2.8797777E-02	0.5759954	0.1349754
304	As	3.4541875E-02	0.6526653	0.1288022
305	As	4.0499207E-02	0.7276918	0.1271912

ATOM NUMBER	TYPE	X	Y	Z
306	As	4.6082150E-02	0.8011711	0.1263540
307	As	5.1639650E-02	0.8736403	0.1258266
308	As	5.7221085E-02	0.9454453	0.1254539
309	Ga	0.1907822	5.3167701E-02	0.1248186
310	Ga	0.1969409	0.1241946	0.1242551
311	Ga	0.2030532	0.1949661	0.1231870
312	Ga	0.2085515	0.2653814	0.1209514
313	Ga	0.2116783	0.3351854	0.1158215
314	Ga	0.2098495	0.4042602	0.1027645
315	Ga	0.1975784	0.4751536	8.3696328E-02
316	Ga	0.1706387	0.5464165	0.1027428
317	Ga	0.1599093	0.6187513	0.1196735
318	Ga	0.1615609	0.6926650	0.1239285
319	Ga	0.1665957	0.7659869	0.1252301
320	Ga	0.1725060	0.8384951	0.1254843
321	Ga	0.1785933	0.9104010	0.1253844
322	Ga	0.1846805	0.9819167	0.1251573
323	As	0.2295925	1.7238826E-02	0.1249656
324	As	0.2358556	8.8417679E-02	0.1245189
325	As	0.2421831	0.1594437	0.1236872
326	As	0.2483187	0.2303127	0.1219870
327	As	0.2532496	0.3009834	0.1182205
328	As	0.2542684	0.3711899	0.1091804
329	As	0.2447730	0.4420228	9.5952205E-02
330	As	0.2242658	0.5147176	9.6641779E-02
331	As	0.2060232	0.5850356	0.1092274
332	As	0.2015394	0.6567996	0.1200244
333	As	0.2051052	0.7297435	0.1238846
334	As	0.2108484	0.8022698	0.1250882
335	As	0.2170964	0.8742673	0.1253247
336	As	0.2233641	0.9458800	0.1252236

References

Alexander H, Haasen P, Labusch R and Schröter W, (1979), *J. de Physique*, **C6**, No. 6, 75.

Alexander H, Kisielowski-Kimmerlich C and Weber ER, (1983), *Physica B & C*, **116**, 583.

Alinaghian P, Gumbsh P, Skinner AJ and Pettifor DG, (1993), *J. Phys.: Condensed Matter*, **5**, 5795.

Anstis GR, Hirsch PB, Humphreys CJ, Hutchison JL and Ourmazd A, (1981), *Inst. Phys. Conf. Ser.*, **60**, p. 15.

Aoki M and Pettifor DG, (1993), *Internat. J. Mod. Phys. B*, **7**, 299.

Bacmann JJ, Papon AM, Petit M and Silvestre G, (1985), *Phil. Mag. A*, **15**, 697.

Bethe H, (1928), *Ann. Phys.*, **87**, 55.

Bigger JRK, (1992), *D.Phil Thesis*, Oxford University.

Bigger JRK, McInnes DA, Sutton AP, Payne MC, Stich I, King-Smith RD, Bird DM, Clarke LJ, (1992), *Phys. Rev. Lett.*, **69**, 2224.

Bilby BA, Bullough R and Smith E, (1955), *Proc. Roy. Soc. London A*, **231**, 26.

Bishop GH and Chalmers B, (1968), *Scripta Met.*, **2**, 133.

Bollmann W, (1970), *Crystal Defects and Crystalling Interfaces*, Springer-Verlag, Berlin.

Bonnet R, (1985), *J. Physique*, **46**, C4-61.

Bourret A, (1982), *Ultramicroscopy*, **9**, 405.

Bourret A and Desseaux J, (1979), *Phil. Mag. A*, **39**, 405.

Bourret A and Desseaux J, (1979), *Phil. Mag. A*, **39**, 419.

Bourret A and Desseaux J, (1979), *J. de Physique*, **40**, C6.

Bourret A and Bacmann JJ, (1985), *J. de Physique*, **46**, NC-4, 27.

Brandon DG, Ralph B, Ranganathan S and Wald MS, (1964), *Acta Metall.*, **12**, 813.

Bristowe PD and Crocker AG, (1975), *Phil. Mag.*, **31**, 503.

Bullough R, (1955), *Ph.D Thesis*, Sheffield University, UK.

Car R and Parrinello M, (1985), *Phys. Rev. Lett.*, **55**, 2471.

Carter CB, (1981), *Mat. Res. Soc. Symp. Proc.*, (ed. Leamy HJ, Pike GEL and Seager CH), **5**, p. 33.

Carter CB, Rose J and Ast DG, (1981), *Inst. Phys. Conf. Ser.*, **60**, 153.

Carter CB, Cho CH, Elgat Z, Fletcher R and Wagner DK, (1985), *Inst. Phys. Conf. Ser.*, **76**, 221.

Chadi DJ, (1978), *Phys. Rev. Lett.*, **41**, 1062.

Chadi DJ, (1979a), *Phys. Rev. B*, **19**, 2074.

Chadi DJ, (1979b), *Phys. Rev. Lett.*, **43**, 43.

Chadi DJ, (1984), *Phys. Rev. B*, **29**, 785.

Chadi DJ and Martin RM, (1976), *Solid State Commun.*, **19**, 643.

Chisholm MF, Pennycook SJ and Jeeson DE, (1990), *Mat. Res. Soc. Symp. Proc.*, **159**, 447.

Cho NH, Carter CB, Wagner DK and McKernan S, (1987), *Inst. Phys. Conf. Ser.*, **87**, 281.

Christian JW and Crocker AG, (1980), *Dislocations in Solids, Vol. 3, (ed. Nabarro FRN)*, North Holland: Amsterdam, p. 165.

Clarke DR, (1978), *J. Appl. Phys.*, **49**, 2409.

Cockayne DJH, Ray ILF and Whelan MJ, (1969), *Phil. Mag.*, **20**, 1265.

Cockayne DJH, Hons A and Spence JCH, (1980), *Phil. Mag. A*, **42**, 773.

Cowley J, (1975), *Diffraction Physics*, North Holland: Amsterdam.

Cunningham B and Ast DG, (1981), *Mat. Res. Soc. Symp. Proc.*, (ed. Leamy HJ, Pike GE and Seager CH), **5**, p. 25 .

D'Anterroches C and Bourret A, (1984), *Phil. Mag. A*, **49**, 783.

DeCooman BC, Cho CH, Elgat Z, Carter CB, (1985), *Ultramicroscopy*, **18**, 305.

DeCooman BC and Carter CB, (1987), *Appl. Phys. Lett.*, **50**, 40.

Desseaux J and Bourret A, (1978), *J. Physique Colloq.*, **39**, C2-116.

Esaki L and Tsu R, (1970), *IBM J. Res. Develop.*, **14**,61.

Fahrenbruch AL and Bube RH, (1983), *Fundamentals of Solar Cells*, (Academic Press: New York), Ch 9.

Feuillet G, (1983), *M.Sc. Thesis*, Oxford University.

Finnis MW, (1990), *J. Phys. C: Condensed Matter*, **2**, 331.

Finnis MW and Sinclair JE, (1984), *Phil. Mag. A*, **50**, 45.

Frank FC, (1950), *Symposium on the Plastic Deformation of Crystalline Solids*, (ONR: Pittsburgh), p. 150.

Frank J, (1980), *Computer processing of Electron Microscope Images*, (ed. Hawkes PW), Springer-Verlag, Berlin.

Frenkel J and Kontorova T, (1938), *Phys. Z. Sowj Un.*, **13**, 1.

Fullmann RL and Fisher JC, (1951), *J. Appl. Phys.*, **22**, 1350.

Gai PL and Howie A, (1974), *Phil. Mag.*, **30**, 939.

Galloway SA, (1994), *D.Phil. Thesis*, Oxford University.

Geipel T, (1993), *Ph.D Thesis*, Case Western Reserve University.

Gerthsen D and Carter CB, (1993), *Phys. Status Solidi A*, **136**, 29.

Gerthsen D, Ponce FA and Anderson GB, (1989), *Phil. Mag. A*, **59**, 1045.

Ghosh AK, Fishman C and Feng T, (1980), *J. Appl. Phys.*, **51**, 446.

Gleiter H, (1977a), *Phil. Mag.*, **36A**, 1109.

Gleiter H, (1977b), *Scripta Metall.*, **11**, 305.

Gomez A and Hirsch PB, (1977), *Philos. Mag.*, **36**, 169.

Gomez A and Hirsch PB, (1978), *Phil. Mag. A*, **38**, 733.

Goodhew PJ, (1980), *Grain Boundary Structure and Kinetics*, (ed. Balluffi RW), Cleveland, Ohio: American Society for Metals, p. 155.

Goodwin L, Skinner AJ and Pettifor DG, (1989), *Europhys. Lett.*, **9**, 701.

Goringe C, (1994), *D.Phil. Thesis*, Oxford University.

Gottschalk H, Patzer G and Alexander H, (1978), *Phys. Status Solidi A*, **45**, 207.

Grimmer H, Bollmann W, Warrington DH, (1974), *Acta Crystall.*, **A30**, 197.

Grovenor CRM, (1985), *J. Phys. C: Sol. Stat. Phys.*, **18**, 4079.

Häussermann F and Shaumburg H, (1973), *Philos. Mag.*, **27**, 745.

Heggie ML and Jones R, (1987), *Inst. Phys. Conf. Ser.*, **87**, p. 367.

Heine V and Hafner J, (1980), *J. Phys. F: Metal Phys.*, **16**, 1429.

Hirsch PB, (1979), *J. Phys. (Paris)*, **40**, C6-27.

Hirsch PB, Howie A, Nicholson RB, Pashley DW and Whelan MJ, (1977), *Electron Microscopy of Thin Crystals.*, IInd ed., (Krieger: New York).

Hirth JP and Balluffi R, (1973), *Acta Metall.*, **21**, 929.

Hirth JP and Lothe J, (1982), *Theory of Dislocations in Solids*, McGraw Hill: New York.

Holt DB, (1964), *J. Phys. Chem. Solids*, **25**, 1395.

Holt DB, (1969), *J. Phys. Chem Solids*, **30**, 1297.

Hornstra J, (1958), *J. Phys. Chem. Solids*, **5**, 129.

Hornstra J, (1959), *Physica*, **25**, 409.

Horsfield A, (1995), *to be published.*

Howie A and Whelan MJ, (1961), *Proc. Roy. Soc.*, **A263**, 217.

Hutchison JL, Anstis GR, Pirouz P, (1983), *Inst. Phys. Conf. Ser.*, **67**, 21.

Jones R, (1979), *J. Phys. (Paris)*, **40**, C6-33.

Jones R, (1981), *Inst. Phys. Conf. Ser.*, **60**, p. 45.

Jones R, Öberg S and Marklund S, (1981), *Phil. Mag. B*, **43** , 839.

Jones R, Umerski A, Sitch P, Heggie MI and Öberg S, (1993), *Phys. Status Solidi A*, **138**, 369.

Keating PN, (1966), *Phys. Rev.*, **145**, 637.

Kim MJ, Carpenter RW, Chen YL and Schwuttke GH, (1992), *Ultramicroscopy*, **40**, 258.

Kohyama M, (1987), *Phys. Stat. Sol. B*, **141**, 71.

Krakow W and Smith DA, (1987), *Ultramicroscopy*, **22**, 47.

Krivanek OL, (1978), *Chem. Scripta*, **14**, 213.

Krivanek OL, Isoda S and Kobayashi K, (1977), *Phil.Mag.*, **36**, 931.

Kronberg ML and Wilson FH, (1959), *Trans. Am. Inst. Min. Engrs.*, **215**, 820.

Kyser DF and Millea MF, (1964), *J. Electrochem. Soc.*, **111**, 1102.

Laue von M, (1949), *Acta Crystallogr.*, **2**, 106.

Liliental-Weber Z and Parechanian-Allen L, (1986), *Appl. Phys. Lett.*, **49**, 18, 1190 .

Lu G and Cockayne DJH, (1986), *Phil. Mag. A*, **53**, 307 .

Majewski JA and Vogl P, (1987), *Phys. Rev. B: Condensed Matter*, **35**, 9666.

Maksimov SK, Filipov AP, Gaidenkov GN, Heydenreich J and Khodos II, (1984), *Phys. Stat. Solidi A*, **84**, 79.

Marklund S, (1978), *Phys. Status Solidi B*, **85**, 673.

Marklund S, (1979), *Phys. Status Solidi B*, **92**, 83.

Marklund S, (1983), *J. Phys. (Paris)*, **44**, C4-25.

Matare HF, (1960), *Proc. Insts. Elect. Engrs. B*, **106**, 293.

McInnes DA, (1992), *D.Phil. Thesis*, Oxford University.

McKernan S, Elgat Z and Carter CB, (1991), *Inst. Phys. Conf. Ser.*, **93**, 171.

Möller HJ, (1978), *Phil. Mag.*, **37**, 41.

Mott NF, (1948), *Proc. Phys. Soc. London*, **60**, 391.

Nabarro FRN, (1947), *Proc. Phys. Soc.*, **59**, 256.

Olsen GB and Cohen M, (1979), *Acta Met.*, **27**, 1007.

Ourmazd A, (1989), *Phys. Rev. Lett.*, **62**, 933.

Paidar V, (1992), *Phil. Mag. A*, **66**, 41.

Paxton AT and Sutton AP, (1989), *Acta Metall.*, **37**, 1693 .

Peierls RE, (1940), *Proc. Phys. Soc.*, **52**, 23.

Pettifor DG, (1977), *J. Phys. F.*, **7**, 613.

Pettifor DG, (1989), *Phys. Rev. Lett.*, **63**, 2480.

Pettifor DG, (1990), *Springer Proc. Phys.*, **48**, 64.

Pond RC and Smith DA, (1976), *Proc. of the Sixth European Cong. on Electron Microscopy (Jerusalem: Tal International)*, p. 233.

Pond RC and Vlachavas DS, (1983), *Trans. Roy. Soc. London, A*, **386** , 95.

Pumphrey PH, (1976), *Grain Boundary Structure and Properties*, (ed. Chadwick GA and Smith DA), London: Academic Press, p. 139.

Pumphrey PH and Goodhew PJ, (1979), *Phil. Mag. A*, **39**, 825.

Putaux JL and Thibault-Desseaux J, (1990), *J. Physique*, **51**, C1-33 .

Ray ILF and Cockayne DJH, (1971), *Proc. Roy. Soc.*, **A325**, 543.

Ray ILF and Cockayne DJH, (1973), *J. Microsc.*, **98**, 170.

Read WT and Shockley W, (1950), *Phys. Rev.*, **78**, 275.

Seitz F, (1940), *Modern Theory of Solids*, McGraw-Hill: New York.

Shockley W, (1953), *Phys. Rev.* , **91**, 228.

Shubnikov AV and Koptsik VA, (1977), *Symm. Sci. Art.*, Plenum: New York.

Slater JC and Koster GF, (1954), *Phys. Rev.*, **94**, 1498.

Smith AR and Eyring L, (1982), *Ultramicroscopy*, **8**, 39.

Smith DA, Pond RC and Vitek V, (1977),*Acta Metall.*, **25**, 475.

Spence JCH , (1988), *Experimental High Resolution Electron Microscopy*, IInd edition, Oxford University Press.

Spence JCH and Kolar H, (1979), *Phil. Mag. A*, **39**, 59.

Stadelmann PA, (1987), *Ultramicroscopy*, **21**, 131.

Stillinger FH and Weber TA, (1985), *Phys. Rev. B*, **31**, 5262.

Sutton AP, (1981), *Ph.D. Thesis*, University of Pennsylvania.

Sutton AP, (1984), *Int. Met. Rev.*, **29**, 377.

Sutton AP, (1989), *Phil. Mag. A*, **60**, 147.

Sutton AP, (1991), *Inst. Phys. Conf. Ser.*, **104**, 13.

Sutton AP, Balluffi RW and Vitek V, (1981), *Scripta Met.*, **15**, 989.

Sutton AP and Vitek V, (1983), *Phil. Trans. Roy. Soc. A*, **309**, 1.

Sutton AP and Balluffi RW, (1987), *Acta Metall.*, **35**, 2177.

Sutton AP, Finnis MW, Pettifor DG and Ohta Y, (1988), *J. Phys. C: Sol. Stat. Phys.*, **21**, 35.

Sutton AP and Balluffi RW, (1990), *Phil. Trans. Roy. Soc. A*, **309**, 1.

Tanaka M and Jouffrey B, (1984), *Phil. Mag. A*, **50**, 733.

Tarui Y, Komiya Y and Harada Y, (1971), *J. Electrochem. Soc.*, **118**, 118.

Teichler H, (1989), *Polycrystalline Semicond.*, (ed. Werner JH, Strunk HP and Möller HJ), Springer Proc. Phys., Springer: Heidelberg, **35**, p. 25.

Tersoff J, (1986), *Phys. Rev. Lett.*, **56**, 632.

Tersoff J, (1988), *Phys. Rev. B*, **38**, 9902.

van der Merwe JH, (1950), *Proc. Phys. Soc. London A*, **63**, 616.

Vaudin MD, Cunningham B and Ast DG, (1983), *Scripta Metall.*, **17**, 191.

Veth H and Teichler H, (1984), *Philos. Mag. B*, **49**, 371.

Vitek V, (1970), *Scripta Met.*, **4**, 725.

Vitek V, Sutton AP, Smith DA and Pond RC, (1979), *Phil. Mag. A*, **39**, 213.

Vitek V, Sutton AP, Wang GJ and Schwartz D, (1983), *Scripta Met.*, **17**, 183.

Vitek V, (1988), *Phil. Mag. A*, **58**, 193.

Vitek V and Wang GJ, (1985), *Dislocations in Solids*, Yamada Science Foundation, University of Tokyo Press, p. 637.

Vogel FL, Pfann WG, Corey HE and Thomas EE, (1953), *Phys. Rev.*, **90**, 489.

Vogl P, Hjalmarson HJ and Dow JD, (1983), *J. Phys. Chem. Solids*, **44**, 365.

Wang YL and Teichler H, (1989), *Phys. Status Solidi B*, **154**, 649.

Weber E and Alexander H, (1979), *J. Physique*, **40**, C6-101.

Werner JH and Strunk HP, (eds), (1991), *Polycrystalline Semiconductors II*, Springer Proc. Phys., Springer-Verlag, Berlin.

Wilshaw PR, (1984), *D.Phil Thesis*, Oxford University.

Wilshaw PR and Booker GR, (1986), *Micros. Semiconduct. Materials 1985*, **76**, Ch. 81, p. 329.

Wilson JH, Todd JD and Sutton AP, (1990), *J. Phys. Condens. Matter*, **2**, 10259.

Wolf D, (1985), *J. de Physique*, **46**, C4-393.

Wosinski T., (1989), *J. Appl. Phys.*, **49**, 5, 2827.

Young CT, Steel JH, Lytton JR, Lytton JL, (1973), *Metallur. Trans.* , **4**, 2081.